

1 **A Web Portal and Workbench for Biological Dissection of Single** 2 **Cell COVID-19 Host Responses**

3
4 Kang Jin^{1,2}, Eric E. Bardes¹, Alexis Mitelpunkt^{1,3,4}, Jake Y. Wang¹, Surbhi Bhatnagar^{1,5}, Soma
5 Sengupta⁶, Daniel P. Krummel⁶, Marc E. Rothenberg⁷, Bruce J. Aronow^{1,8*}

6
7 ¹Division of Biomedical Informatics, Cincinnati Children's Hospital Medical Center, Cincinnati,
8 OH, 45229, USA

9 ²Department of Biomedical Informatics, University of Cincinnati, Cincinnati, OH, 45229, USA

10 ³Pediatric Rehabilitation, Dana-Dwek Children's Hospital, Tel Aviv Medical Center, Tel Aviv,
11 6423906, Israel

12 ⁴Sackler Faculty of Medicine, Tel Aviv University, Tel Aviv, 6997801, Israel

13 ⁵Department of Electrical Engineering and Computer Science, University of Cincinnati,
14 Cincinnati, OH, 45221, USA

15 ⁶Department of Neurology and Rehabilitation Medicine, University of Cincinnati College of
16 Medicine, Cincinnati, OH, 45267, USA.

17 ⁷Division of Allergy and Immunology, Department of Pediatrics, Cincinnati Children's Hospital
18 Medical Center, University of Cincinnati, Cincinnati, OH, 45229, USA

19 ⁸Department of Pediatrics, University of Cincinnati School of Medicine, Cincinnati, OH, 45256,
20 USA

21 *Corresponding author. Email: bruce.aronow@cchmc.org (B.A.)

22
23

24 **Abstract**

25

26 Numerous studies have provided single-cell transcriptome profiles of host responses to SARS-
27 CoV-2 infection. Critically lacking however is a reusable datamine to allow users to compare and
28 explore these data for insight, inference, and hypothesis generation. To accomplish this, we
29 harmonized datasets from blood, bronchoalveolar lavage and tissue samples from COVID-19 and
30 other control conditions and derived a compendium of gene signature modules per cell type,
31 subtype, clinical condition and compartment. We demonstrate approaches for exploring and
32 evaluating their significance via a new interactive web portal (ToppCell). As examples, we
33 develop three hypotheses: (1) a multicellular signaling cascade among alternatively differentiated
34 monocyte-derived macrophages whose tasks include T cell recruitment and activation; (2) novel
35 platelet subtypes with drastically modulated expression of genes responsible for adhesion,
36 coagulation and thrombosis; (3) a multilineage cell activator network able to drive extrafollicular
37 B maturation via an ensemble of genes extensively associated with risk for developing
38 autoimmunity.

39

40 **Teaser**

41

42 Implicating COVID-19 Gene and Cell Networks Responsible for Inflammation,
43 Thromboembolism and Autoimmune Pathobiology.

44

45 **Short title**

46 Data mining COVID-19 Gene and Cell Networks

47

48

49 **Introduction**

50
51 COVID-19 clinical outcomes are variable. The poorer outcomes due to this infection are highly
52 associated with immunological and inflammatory responses to SARS-Cov-2 infection (1, 2) and
53 many recent single cell expression profiling studies have characterized patterns of
54 immunoinflammatory responses among individuals, mostly during acute infection phases.
55 Different studies have revealed a spectrum of responses that range from lymphopenia (3, 4),
56 cytokine storms (5, 6), differential interferon responses (7, 8) and emergency myelopoiesis (9,
57 10). However, a variety of obstacles limit the ability of the research and medical communities to
58 explore and compare these studies to pursue additional questions and gain additional insights that
59 could improve our understanding of cell type specific responses to SARS-CoV-2 infection and
60 their impact on clinical outcome.

61 Whereas many studies have focused on the peripheral blood mononuclear cells (PBMC) (9, 11–
62 14) due to ease of procurement, other studies have profiled airway locations via bronchoalveolar
63 lavage (BAL) (15, 16), nasopharyngeal swabs, and bronchial brushes (17). Additional sampling
64 sites that could also be infected or affected have also been approached in autopsy-derived
65 materials from the central nervous system (18, 19), and other sites (20). Moreover, as major
66 COVID-19 consortiums working on the collection and integration of each of their individual
67 studies and interpreting important features of these individual datasets as downloadable datasets
68 or browsable versions, such as single cell portal
69 (https://singlecell.broadinstitute.org/single_cell/covid19) and COVID-19 Cell Atlas
70 (<https://www.covid19cellatlas.org/>), using these data beyond markers, cell types, and individual
71 signatures is either not possible or not accomplishable across-datasets. Thus, a well-organized and
72 systematic study of immune cells across tissues for in-depth biological explorations is an unmet
73 need for a deeper understanding of the underlying basis of the breadth of COVID-19 host defense
74 and pathobiology.

75
76 Here we harmonized and analyzed eight high quality publicly available single-cell RNA-seq
77 datasets from COVID-19 and immunologically-related studies that in total covered more than
78 480,000 cells isolated from peripheral blood, bronchial alveolar lavage and lung parenchyma
79 samples, and assembled an integrated COVID-19 atlas (<https://toppcell.cchmc.org/>). We
80 established a framework for deriving, characterizing, and establishing reference gene expression
81 signatures from these harmonized datasets using modular and hierarchical approaches based on
82 signatures per class, subclass, and signaling/activation and clinical status per each sample group.

33 Leveraging these gene expression signature modules, we demonstrate datamining approaches that
34 allow for the identification of a series of fundamental disease processes: (1) an intercellular
35 monocytic activation cascade capable of mediating the emergence of hyperinflammatory
36 monocyte-derived alveolar macrophages in severe COVID-19 patients; (2) the generation of
37 several alternatively differentiated platelet subtypes with dramatically different expression of sets
38 of genes associated with critical platelet tasks capable of altering vascular and tissue responses to
39 infectious agents; and (3) a multilineage and multi cell type cooperative signaling network with
40 the potential to drive extrafollicular B maturation at a lesion site, but do so with high risk for the
41 development of B cell-associated immunity. Additionally, immune hallmarks of COVID-19
42 patients were compared with other immune-mediated diseases using single-cell data from patients
43 with influenza, sepsis, or multiple sclerosis. Consistent and varied compositional and gene
44 patterns were identified across these implicating striking COVID-19 effects in some individuals.

45 46 **Results**

47 48 **Creating the First COVID-19 Signature Atlas Using ToppCell Portal**

49 To have a comprehensive coverage of cells, we collated single-cell data of COVID-19 patients
50 from eight public datasets, which in total contains 231,800 PBMCs, 101,800 BAL cells and
51 146,361 lung parenchyma cells from donors: 43 healthy; 22 mild; 42 severe; and 2 convalescent
52 patients (Fig. 1A, table S1).

53
54 To assemble an integrated atlas of human cell responses to COVID-19, we sought to harmonize
55 metadata encompassing clinical information, sampling compartments, and cell and gene
56 expression module designations. Doing so provides a rich framework for detecting perturbations
57 of cell repertoire and differentiative state adaptations. We first integrated single cell RNA-seq
58 data in Seurat (21) and annotated cell types using canonical markers (table S2). Further
59 annotations of B cell and T cell subtypes were completed using the reference-based labeling tool
60 Azimuth (22). Sub-clustering was applied for some cell types, such as neutrophils and platelets, to
61 interrogate finer resolutions of disease-specific sub-populations (Fig. 1B). Using the ToppCell
62 toolkit (<https://toppcell.cchmc.org/>), we created over 3,000 hierarchical gene modules of the most
63 significant differentially expressed genes (DEGs) for all cell classes and sub-clusters across
64 compartments and disease severity (table S1). These modules were then used to infer cell-cell
65 interactions as well as upregulated pathways, which were further combined for functional
66 comparative analysis in a specific cell manner in ToppCluster (23) (Fig. 1B), such as sub-clusters

17 of platelets. Integration of ToppCluster output of cells from multiple compartments and disease
18 conditions built pathogenic maps, highlighted by the coagulation map of COVID-19 (fig. S12). In
19 addition, perturbation of cell abundance was evaluated either in one cell population, or in multiple
20 populations across diseases. Taken together, we investigated cell abundance changes, severity-
21 associated signatures, mechanisms of COVID-19 specific symptoms and unique features of
22 COVID-19 as an immune-mediated disease (Fig. 1B).

23

24 **Dynamic Changes and Balance of COVID-19 Immune Repository in Blood and Lung**

25 After the aforementioned cell annotation procedure, we identified 28 and 24 distinct cell types in
26 PBMC and BAL respectively (Fig. 2, A and C, table S2). Shifts of Uniform Manifold
27 Approximation and Projection (UMAP) of cell type distributions were observed in both
28 compartments of mild and severe patients (Fig. 2, A and C, fig. S1A and fig. S3A). In PBMC,
29 conventional dendritic cells (cDC), plasmacytoid dendritic cells (pDC) and non-classical
30 monocytes displayed a prominent reduction in severe patients (Fig. 2B and fig. S1C), consistent
31 with prior reports (11, 24, 25). In contrast, severe patients demonstrated dramatic expansion of
32 neutrophils, especially immature stages (fig. S1C and fig. S2). Integration with evoked pathways
33 in the following analysis implicated that neutrophil expansion was likely the consequence of
34 emergency myelopoiesis (26). Additionally, a general down-regulation of T cell and NK cell was
35 observed, consistent with lymphopenia reported in clinical practices (5, 27) (fig. S1C and fig. S2).
36 However, the trend of T cell subtypes varies across studies and individuals, apart from
37 proliferative T cells which have a dramatic increase in mild and severe patients (fig. S2). Notably,
38 plasmablasts substantially increased in COVID-19 patients, and especially so in severe patients,
39 suggesting upregulated antibody production (28) (Fig. 2B and fig. S1C). Expansion of platelets is
40 another significant change observed in severe patients, possibly leading to immunothrombosis in
41 the lung, which could be closely associated with the severity of the disease (29, 30) (Fig. 2B and
42 fig. S1C).

43

44 In samples obtained from patients' lungs, we observed the depletion of FABP4^{high} tissue-resident
45 alveolar macrophages (TRAM) and dramatic expansion of FCN1^{high} monocyte-derived alveolar
46 macrophages (MoAM) in severe patients (Fig. 2, C and D and fig. S3D). Mild patients exhibited a
47 moderate reduction of tissue-resident macrophages, but no evidence of aggregation of monocyte-
48 derived macrophages (Fig. 2, C and D, fig. S3, A and D). Dynamic changes of these two subtypes
49 suggest increased tissue chemoattraction (31) and potential damage of patients' lungs (32). In

50 addition, neutrophils were only identified in severe patients in the integrated BAL data (Fig. 2C
51 and fig. S3A), which might be related with neutrophil extracellular traps (NETs) in the lung (33).
52 However, more samples are required to draw a solid conclusion. We also noted conventional
53 dendritic cells decreased in the severe patients, which is consistent with the trend of the
54 counterpart in PBMC data. Opposite to the change in PBMC, an expansion of plasmacytoid
55 dendritic cells is observed in both mild and severe patients (Fig. 2D). Other cell types, including T
56 cell and NK cell in the BAL, also have converse changes of their counterparts in PBMC, which
57 could be attracted by lung macrophages or epithelial cells after infection or damages (17) (Fig. 2D
58 and fig. S3D). These changes were consistently observed in lung parenchyma samples from
59 severe COVID-19 patients (fig. S4). With cells well-annotated in the integrated COVID-19 atlas,
60 we drew a global heatmap for cells in both blood and lung using ToppCell gene modules (top 50
61 DEG in each module) of all identified cell classes. While there was conservation of gene patterns
62 involved in healthy donors and severe COVID-19 patients, there were substantial differences
63 most notably in myeloid cells (Fig. 2E). Such hierarchically ordered ToppCell gene modules were
64 broadly used in visualization, large-scale comparisons and fine-resolution investigations in the
65 following analyses.

66

67 **Myeloid Cell Atlas: Functionally Distinct Neutrophils at Different Levels of Maturation and** 68 **Derailed Macrophages in the Lung**

69 Dysregulated myeloid cells have been reported as an important marker of severe COVID-19
70 patients (9, 10). In order to gain a deeper and comprehensive understanding of these cells, we
71 applied the sub-clustering strategy on the integrated data of key cell types, such as neutrophils and
72 macrophages, and then generated gene modules for comparative functional analysis and
73 interactome inference. We successfully identified 5 neutrophil sub-clusters after the integration of
74 PBMC and BAL data, including 3 FCGR3B⁺ mature sub-clusters and 2 FCGR3B⁻ immature sub-
75 clusters (Fig. 3A and fig. S5B, table S3). They're mainly from severe patients and their gene
76 modules were generated and subjected to comparative functional enrichment using ToppCell and
77 ToppCluster (Fig. 3, C and D, fig. S5A). We identified proliferative neutrophils (referred to as
78 pro-neutrophils and Neu4) and MMP8^{high} precursor immature neutrophils (referred to as pre-
79 neutrophils and Neu2) (Fig. 3A and fig. S5B) consistent with prior studies (9). While immune
80 response genes and pathways were barely activated in the immature neutrophils, they displayed
81 upregulation of granule formation pathways and NETosis-associated proteins, including ELANE,
82 DEFA4 and MPO, especially in Neu4 (9, 26) (Fig. 3C, fig. S5, B and C). Upregulated myeloid

33 leukocyte mediated immunity in Neu2 suggests involvement of this cell type in anti-viral function
34 (Fig. S5D). Yet, the absence of cytokine and interferon response pathways suggests the lack of
35 mature immune responses (Fig. 3D). Notably, compared to mature neutrophils (Neu0 and Neu1)
36 in the blood, the extravasated hyperinflammatory sub-cluster (Neu3) from BAL of severe patients
37 shows extraordinarily high expression of interferon-stimulated genes, as well as prominent
38 upregulation of productions and responses to cytokines and interferons (Fig. 3, C and D, fig S5, B
39 and D).

40
41 MoAM and TRAM were two main macrophage types in the BAL (Fig. 2C); both are known to
42 have distinct roles in immune responses in the lung (15). As described above, five sub-clusters
43 among the expanded COVID-19 patient-specific MoAM (Fig. 3B, table S3) were found, where
44 the loss of HLA class II genes and elevation of interferon-stimulated genes (ISGs) were
45 consistently observed (Fig. 3F and fig. S6A). Relative to MoAM3,4, MoAM1,2,5 displayed an
46 upregulation of interferon responses and cytokine production (Fig. 3D, fig. S6B and table S3),
47 indicating their pro-inflammatory characteristics. Notably, MoAM5 shows dramatic upregulation
48 of IL-6 secretion and cytokine receptor binding activities (Fig. S7, A to D). However, cells in this
49 sub-cluster were mainly from one severe patient (fig. S3C). We still need more data to fully
50 understand such dramatic upregulation of IL-6 secretion in some severe patients. Similar to
51 MoAM, we also identified two distinct groups of TRAM in BAL (Fig. 3B and fig. S6B),
52 including quiescent TRAM (TRAM1 and TRAM2) and activated TRAM (TRAM3). The
53 quiescent group was mainly from healthy donors with enriched pathways of ATP metabolism
54 (Fig. 3D), while the activated group from mild and severe patients displays upregulation of ISGs
55 and cytokine signaling pathways (fig. S6B and table S3). However, the magnitude of activation
56 and inflammatory responses in TRAM3 is smaller than MoAM1,2,5. Not surprisingly, stronger
57 antigen processing and presentation activities were observed in TRAM3 relative to MoAM1,2,5
58 (Fig. 3D, fig. S6B and table S3). Collectively, we concluded that tissue-resident macrophages
59 were greatly depleted in severe patients as the front-line innate immune responders in the lung.
60 Pro-inflammatory monocyte-derived macrophages infiltrate into the lung, leading to the cytokine
61 storm and damage of the lung. Large amounts of infiltration of MoAM were not observed in mild
62 COVID-19 patients, probably due to the controlled infection, which could explain milder lung
63 damages in those patients.

14

15 To develop an understanding of the interaction network in the lung microenvironment of severe
16 COVID-19 patients, we focused on signaling ligands, receptors and pathways using ToppCell and
17 CellChat (Fig. 3E and fig. S8, A and B). Notably, basal cells, MoAMs, neutrophils and T cells all
18 contributed to the cytokine, chemokine and interleukin signaling networks. Strikingly, severe
19 patient specific MoAM2 shows the broadest upregulation of signaling ligands, including CCL2,
20 CCL3, CCL7, CCL8, CXCL9, CXCL9, CXCL10, CXCL11, IL6, IL15 and IL27, suggesting its
21 role as a signaling network hub that is distinct from the other major signaling ligand-expressing
22 cells of BAL such as epithelial and other myeloid cell types such as TRAM3 and proliferating
23 myeloid cells (fig. S8A). Among the MoAM2 top signaling molecules, attractants CXCL8,
24 CXCL9 and CXCL10 are known to target CXCR3 on T cells, suggesting their role is to stimulate
25 migration of T cells to the epithelial interface and into BAL fluid (Fig. 3E) (15). In addition,
26 many of MoAM2's ligands have the potential to cause autocrine signaling activation via IL6-
27 IL6R, IL1RN-ILR2, CCL7-CCR1, CCL2-CCR1 and CCL4-CCR1, indicating its active roles in
28 self-stimulation and development, which further amplify the attraction and migration of T cells
29 and other immune cells. Notably, CCR1 was also expressed in activated TRAM3, but with a
30 lower level. Although IL6 expression level is relatively low compared to other ligands in BAL
31 data, substantial expression of IL6R was observed in MoAMs. The CCL and CXCL signaling
32 pathways of neutrophils are less strong than MoAMs (fig. S8B), but they displayed high
33 expression levels of CXCR1 and CXCR2, which binds with a large number of the chemokines
34 from MoAM and epithelial cells (Fig. 3E). In addition, neutrophils exhibit an extraordinarily high
35 level of IL1B, which could potentially in turn activate macrophages (fig. S8, A and B). TRAM3
36 also displayed a unique pattern of signaling molecules, with a substantial level of CCL23 which
37 could potentially attract MoAM by the interaction with CCR1. Secretion of CXCL3 and CXCL5
38 in TRAM3 towards CXCR2 could be a potential chemoattraction pathway for neutrophils. In turn,
39 neutrophils could activate TRAM3 by secreting IL1B, which binds with IL1RAP. Additionally,
40 CD4+ T cells could also activate TRAM3 by IL10-IL10RB interaction (Fig. 3E and fig. S8, A and
41 B).

42
43 In addition to neutrophils and macrophages, the upregulation of ISGs was observed in classical
44 monocytes of both mild and severe patients (cMono3, cMono4), while the reduction of the MHC
45 class II cell surface receptor HLA-DR genes was only observed in severe patients (cMono4) (fig.
46 S9). In cDCs, polarization of interleukin secretion was observed in mild-patient and severe-
47 patient specific clusters (fig. S10F). Collectively, dynamic changes of marker genes,

48 transcriptional profiles, signaling molecules and biological activities reveal the heterogeneity of
49 myeloid cell sub-clusters across disease severity (fig. S11C). Pro-inflammatory gene expression
50 was found in all major myeloid cell types, including cMono4, DC1, DC9 in PBMC and Neu3,
51 DC10, MoAM1, MoAM2, MoAM5 in BAL of COVID-19 patients. The reduction of MHC class
52 II (HLA-II) genes is a common feature of classical monocytes and macrophages in COVID-19
53 patients and implies impaired capacity to activate T cell adaptive immunity.

54

55 **COVID-19 Coagulation and Immunothrombosis Map**

56 Individuals severely affected during acute phase COVID-19 infection, and in particular those with
57 significantly elevated risk of death, frequently demonstrate striking dysregulation of coagulation
58 and thrombosis characterized by hypercoagulability and microvascular thromboses (endothelial
59 aggregations of platelets and fibrin) and highly elevated D-dimer levels. Yet, COVID-19 does not
60 lead to wide scale consumption of fibrinogen and clotting factors (29, 30, 34–36). At present, we
61 lack a molecular or cellular explanation of the underlying basis of this pathobiology (29, 37). To
62 evaluate candidate effectors of this pathobiology, we used a list of genes associated with
63 abnormal thrombosis from mouse and human gene mutation phenotypes and identified
64 parenchymal lung sample endothelial cells and platelets in PBMC as cell types highly enriched
65 with respect to genes responsible for the regulation of hemostasis (fig. S12). Because platelet
66 counts were greatly elevated in severe versus mild individuals, we further examined platelet gene
67 expression signatures and cell type differentiation and identified six distinct platelet sub-clusters
68 shared across all datasets after data integration (Fig. 4, A and B). Severe-patient-specific PLT0 is
69 an interesting sub-cluster with elevated integrin genes, including ITGA2B, ITGB1, ITGB3,
70 ITGB5, as well as thrombosis-related genes, such as SELP, HPSE, ANO6 and PF4V1. Antibodies
71 against the latter are associated with thrombosis including adverse reactions to recent COVID-19
72 vaccine ChAdOx1 nCoV-19 (38). In addition, upregulated pathways of hemostasis, wound
73 healing and blood coagulation were also observed in PLT0 (Fig. S13A and table S4). Importantly,
74 PLT2 is an inflammatory sub-cluster with an upregulation of ISGs and interferon signaling
75 pathways, while PLT4 is highlighted by upregulated post-transcriptional RNA splicing activities
76 (Fig. S13, A and C).

77

78 Severity-associated gene patterns were also identified by selecting coagulation-associated genes
79 modules (Fig. 4C and table S4), indicating distinct coagulation activities across platelets. Apart
80 from pan-platelet genes, we found dramatic upregulation of genes involved in platelet activation,

31 fibrinogen binding and blood coagulation in platelets of severe COVID-19, including
32 procoagulant heparanase (HPSE) (39), Anoctamin-6 (ANO6) (40), and selectin P (SELP) (41)
33 (Fig. 4, C and D). Heparanase is an endoglycosidase that cleaves heparan sulfate constituents, a
34 major component of anti-coagulation glycocalyx on the surface of vascular endothelium (42, 43).
35 Upregulated heparanase was related to upregulation of cell-matrix adhesion and coagulation (Fig.
36 4D). Thrombotic vascular damages could be caused by the degradation function of heparinase
37 enriched in platelets of severe patients. Elevation of ANO6 is known to trigger phospholipid
38 scrambling in platelets, resulting in phosphatidylserine exposure which is essential for activation
39 of the clotting system (44). In addition, other upregulated genes involved in coagulation-
40 associated activities were also observed, including wound healing, fibrinolysis, platelet
41 aggregation and activation (Fig. 4D), which likely collectively contribute to the clotting issue of
42 severe COVID-19 patients.

43

44 **Emergence of Developing Plasmablasts and B Cell Association with Autoimmunity**

45 Autoimmune disorders in COVID-19 patients such as immune thrombocytopaenic purpura (ITP)
46 is now recognized as a known disease complication (45–49). However, little is known about the
47 molecular and cellular mechanism behind it. To examine this further, we integrated B cells and
48 plasmablasts from both PBMC and BAL and conducted systematic analysis (Fig. 5, A and B and
49 fig. S14, A and B). Several COVID-19 specific sub-clusters were identified in B cells, such as
50 ISG^{high} activated B cells (cluster 7) (Fig. 5A). Importantly, activated B cells showed dramatic
51 upregulation of interferon signaling pathways and cytokine productions (fig. S15A), indicating its
52 anti-virus characteristics. Notably, plasmablasts were mainly observed in severe COVID-19
53 patients, where a group of proliferative cells was identified and labeled as developing
54 plasmablasts (Fig. 5B). In contrast, non-dividing plasmablasts displayed upregulation of
55 immunoglobulin genes (IGHA1, IGHA2, IGKC), B cell markers (CD79A) (50), interleukin
56 receptors (IL2RG) and type II HLA complex (HLA-DOB) (Fig. 5C and table S5). In addition,
57 non-dividing plasmablasts showed unique isotypes of immunoglobulin (Ig) in sub-regions of
58 UMAP, whereas developing plasmablasts displayed obscure Ig types (fig. S14, E and F).
59 Antibody production activities were upregulated in non-dividing plasmablasts based on gene
60 enrichment analysis (Fig. S15A and table S5). Collectively, we inferred that non-dividing
61 plasmablasts had definite immunoglobulin isotypes and were actively involved in immune
62 responses towards COVID infection, while developing plasmablasts were less mature but highly
63 proliferative to replenish the repertoire of plasma cells.

14

15 Since there are few clues of gene associations of autoimmunity in COVID-19, we brought up a
16 hypothesis-driven, prior knowledge-based approach to discover and prioritize genes for the
17 specific phenotype (Fig. 5D). First, gene modules of B cells and other cells in severe patients
18 were collected and subjected to ToppGene for enrichment analysis. Then we queried
19 autoimmunity-associated terms in the enriched output and identified associated genes. After that,
20 we retrieved interaction pairs using ToppCluster and CellChat database (51). In the end, we
21 identified genes that are not only involved in autoimmunity, but have a mediator role in the
22 immune signaling network. Using this approach, we observed several candidate pairs of genes,
23 including TNFSF13B-TNSRSF13, IL10-IL10RA, IL21-IL21RA, IL6-IL6R, CXCL13-CXCR5,
24 CXCL12-CXCR4, CCL21-CCR7, CCL19-CCR7 and CCL20-CCR6 in severe patients, which
25 were enriched for autoimmune diseases, such as autoimmune thyroid diseases, lupus nephritis,
26 autoimmune encephalomyelitis (52–56). Candidate cytokine and chemokine ligand genes were
27 expressed in various cell types in PBMC and BAL, including IL21 and CXCL13 from exhausted
28 T cells of BAL, CXCL12 from mesenchymal cells, IL6 and CCL21 from endothelial cells,
29 CCL19 from cDC and CCL20, TNFSF13B, and TNFSF13 from lung macrophages (Fig. 5E and
30 table S5). These interaction pairs have been linked with auto-immunity (57, 58). In addition, we
31 analyzed single-cell studies (59, 60) of rheumatoid arthritis and lupus nephritis patients and found
32 that high expression levels of the candidate receptors in B cells and ligands in other cells were
33 also observed, such as CXCL13 in helper T cells and CXCR5 in B cells in both studies (fig. S15,
34 C and D). However, more evidence is still required to infer the association between these
35 interactions and autoimmunity in COVID-19 patients. Supported by the evidence above, we drew
36 a network for potential mediator interactions of B cells and their associations with autoimmune
37 disorders, where linkages with diseases, such as rheumatoid arthritis, systemic lupus
38 erythematosus, were highlighted, as well as linkages with mouse phenotypes, such as abnormal
39 immune tolerance and increased susceptibility to autoimmune disorder (Fig. 5F). As a caveat,
40 although using prior knowledge to prioritize gene and cell-associated functions and interactions
41 may introduce biases, such approaches also have the potential to highlight key similarities and
42 differences between different disease causes and clinical responses and improve our
43 understanding of the molecular and cellular mechanisms at work.

44

45 **Functional Map and Immune Cell Interplay Landscape in COVID-19**

46 As above, where highly significant enrichments of unique functions and pathways could be
47 identified in the subtypes of multiple cell classes, such as neutrophils, platelets and B cells, we
48 sought to get a more holistic understanding of COVID-19 specific cell class and subclass-level
49 signatures, including T cell subtypes (fig. S16 and fig. S17), we built an integrative functional
50 map of all cell types in three compartments across multiple disease conditions using a highly
51 integrated gene module set (Fig. 6A and table S6). All enriched functional associations in
52 ToppCluster for gene modules of cell types and sub-clusters were depicted. They were grouped
53 by disease conditions and compartments to show heterogeneity of cellular functions in different
54 circumstances.

55
56 In the heatmap (Fig. 6A), most enrichments were consistently observed across cells of healthy
57 donors and COVID-19 patients. However, some unique patterns were also identified. For
58 example, T cells and NK cells in healthy donors show enrichments of mitochondrial transport and
59 ATP metabolic process, while activated T cells in mild patients show upregulation of type I
60 interferon production and cytokine signaling. Enrichments of macrophage differentiation and
61 neutrophil migration regulation were uniquely found in MoAM1 in severe patients (Fig. 6A). The
62 function map provides a high-level approach to investigate functional variations of cells across
63 disease conditions and compartments. The predicted interplay of immune cells across multiple
64 compartments and disease conditions is displayed in Fig. 6B. Cell proportion changes, sub-cluster
65 specific signatures and cell-cell interaction are also depicted.

66 67 **Similarity and Heterogeneity Between COVID-19 and Other Immune-mediated Diseases**

68 To further analyze COVID-19 specific immune signatures, we compared immune cells from
69 COVID-19 patients with cells in other immune-mediated diseases, including severe influenza
70 (12), sepsis (61) and multiple sclerosis (62). 404,125 cells were included after the integration of
71 PBMC single-cell datasets (Fig. 7A and fig. S18, table S7). Dynamic changes of cell abundance
72 were compared in diseases versus healthy donors. Similar to COVID-19 patients, severe influenza
73 patients also exhibited the reduction of non-classical monocytes, pDC, cDC and CD4⁺ TCM, but
74 the effect of the former two types was smaller in magnitude (Fig. 7B). However, the reduction of
75 non-classical monocytes is more significant in severe COVID-19 patients than severe influenza or
76 mild COVID-19 patients (Fig. 7B). Notably, NK cell reduction is associated with COVID-19
77 severity, whereas T cell depletion is a more dramatic perturbation in severe influenza. Within
78 these comparisons, the expansion of plasmablasts is consistently observed, whereas the

79 accumulation of platelets is unique to SARS-CoV-2 and in particular, to severe COVID-19
30 clinical status (Fig. 7B).

31

32 In addition to dynamic changes of cell ratios, we also investigated the regulation of immune
33 mediator genes across various diseases (Fig. 7C and table S7). IL-6 is an important factor of
34 cytokine storms in COVID-19 (63). As shown in the heatmap, naive B cells are the main sources
35 of IL-6 in COVID-19 patients while CD14⁺ monocytes show the highest expression levels in
36 severe influenza patients (Fig. 7C). Specific ligands, including CXCL2, CXCL3, CCL20 were
37 upregulated in both severe COVID-19 patients and severe influenza patients. CCR4 and IL2RA is
38 uniquely high in CD4⁺ T cells of COVID-19 patients. Interestingly, most PBMC myeloid cell
39 types displayed upregulated levels of interferon-stimulated genes in both COVID-19 and
40 influenza, especially in COVID-19, where highest levels of ISGs in CD14⁺ Monocytes, cDC and
41 pDC were observed.

42

43

44 **Discussion**

45

46 In this work, we have constructed an innovative immune signature atlas of the blood and lung of
47 COVID-19 patients using the integrated single cell RNA-sequencing data and Topp-toolkit. By
48 virtue of systemic analysis of large sample size from multiple sampling sites, consistent
49 immunopathology-associated changes of cell abundance and transcriptional profiles were
50 observed in the circulating and lung immune repertoire of COVID-19 patients. The established
51 single cell atlas and the provided public portal (<https://toppcell.cchmc.org/>) enables the query of
52 candidate molecules and pathways in each of these processes.

53

54 Leveraging this approach, we identified three major candidate mechanisms capable of driving
55 COVID-19 severity: (1) a cascade-like network of proinflammatory autocrine and paracrine
56 ligand receptor interactions among subtypes of differentiating mononuclear, lymphoid, as well as
57 other cell types; (2) the production of emergency platelets whose gene expression signatures
58 implicate significantly elevated potential for adhesion, thrombosis, attenuated fibrinolysis, and
59 potential to enhance the release of heparin-bound cytokines as well as further influence the
60 activation of neutrophils causing further inflammatory cell recruitment and neutrophil netosis; and
61 (3) the extrafollicular activation of naive and immature B cells via a multilineage network that
62 includes monocytic subtypes and exhausted T cells of cytokines and interleukins with the

13 potential to generate local antigen specific response to virus infected targets and collateral
14 autoimmunity. More details will be discussed below.

15

16 We identified dramatically expanded macrophages which were marked by the loss of HLA class
17 II genes and upregulation of interferon-stimulated genes. It implicates a key role for these
18 activated macrophages involved in signaling network and less so in activation of adaptive T cell
19 immunity. Among them, MoAM2 displayed hyperinflammatory responses and extraordinary high
20 levels of signaling molecules, which are involved in both autocrine (e.g. IL-6, CCL2, CCL4 and
21 CCL8) and paracrine (e.g. CXCL2, CXCL9, CXCL10 and CXCL11) signaling pathways. The
22 former pathway contributed to the self-stimulation and development, which amplified the
23 paracrine pathway for T cell and neutrophil chemoattraction. The latter two cell types in turn
24 activated MoAMs with cytokines genes (CCL5, IL10 of T cells and IL1B of neutrophils,
25 respectively). Based on the intercellular and multifactor complexity of the signaling cascade we
26 have outlined, to effectively control a malignant inflammatory cascade, it may be essential to
27 consider simultaneously targeting multiple nodes of this network of cytokines and interleukins. In
28 addition, HLA-DR^{low} monocytes, likely reflecting dysfunctional cells, were observed in severe
29 infection. This, along with evidence of emergency myelopoiesis with immature circulating
30 neutrophils into the circulation was detected in severe COVID-19. These neutrophils had
31 transcriptional programs suggestive of dysfunction and immunosuppression not seen in patients
32 with mild COVID-19. As such, we have presented evidence for the contribution of defective
33 monocyte activation and dysregulated myelopoiesis to severe COVID.

34

35 Platelet expansion is uniquely observed in COVID-19 versus other immune-mediated diseases.
36 Strikingly, these activated platelets were highlighted with abnormal thrombosis and upregulated
37 heparanase, a procoagulant endoglycosidase that cleaves anti-coagulation heparan sulfate
38 constituents on endothelial cells and potentially causes thrombotic vascular damages.
39 Additionally, heparanase-cleaved heparan sulphate (HS) fragments were capable of stimulating
40 the release of pro-inflammatory cytokines, such as IL1B, IL6, IL8, IL10 and TNF through the
41 TLR-4 pathway in PBMC (64), further contributing to the hyperinflammatory environment in
42 COVID-19 patients. Since heparanase is recognized as a hallmark in tumor progression and
43 metastasis (65), we hypothesize COVID-19 infection could be associated with higher occurrence
44 of lung tumor metastasis. However, more data is required to support it. Pro-neutrophil secreted

45 proteins (e.g. ELANE, DEF4) of neutrophil extracellular trap (NET), which have been reported to
46 be associated with higher risk of morbid thrombotic events (66). Approaches to combatting NETs
47 could a potential anticoagulation treatment (67).

48
49 We propose a signaling network which potentially shapes the differentiation of B cells towards
50 the formation of autoantibodies. Proliferation and activation of inflammatory myeloid cells and
51 the formation of exhausted CD4+ T helper around an area of direct or indirect viral tissue injury
52 leads to the production of a set of interleukins and cytokines known to have both direct cell
53 activating and maturing effects on naïve and immature B cells. Previous report had revealed the
54 exaggerated extrafollicular B cell response, which is part of a mechanism that stimulates somatic
55 mutation and maturation of B cells to produce plasma cells with specificity for antigens present in
56 the vicinity of tissue damage sites (68). In the absence of macrophages or dendritic cells to restrict
57 self vs non-self, the presence of IL-10, IL-21, CXCL13 CXC10, IL-6 and others acting on
58 receptors present in naïve and immature B cells leads to the selection and maturation of self-
59 reactive maturation of B cells clones with formation of autoantibodies. Many of these COVID-19-
60 activated genes (e.g. CXCL13, CCL19, CCL20, TNFRSF13) are known to be genetically
61 associated with rheumatoid arthritis, lupus, and risk of developing autoimmune disease in humans
62 and mouse models. The development of different patterns of autoimmunity may be the main
63 hallmark of “Long Haul” Covid disease and could explain why some individuals develop
64 different autoantibodies and suffer different forms of clinical consequences depending on which
65 antigens drive the B-cell maturation. Thus, an additional prediction that could be made based on
66 these findings and our network model is that among individuals treated with corticosteroids at the
67 time these auto-immunogenic processes are activated, there should be a protective effect and
68 lower likelihood of developing post acute sequela of COVID.

69
70 Consistent and varied compositional changes and gene patterns of immune cells were identified in
71 COVID-19, influenza and sepsis. Expansion of plasmablasts, as well as the reduction of non-
72 classical monocytes, are more significant changes in severe COVID-19 patients, while the
73 depletion of T cells is more dramatic in severe influenza patients. The accumulation is a unique
74 immune hallmark of COVID-19 within the selected diseases, which contributes to the coagulation
75 abnormalities and thrombosis, a key cause of fatality in COVID-19 patients. Different signaling
76 gene patterns were identified across immune-mediated diseases, with CCR4 only highly
77 expressed in CD4+ T cells of COVID-19 patients, which might be related with extravasation of

78 these cells (69). Upregulated interferon-stimulated genes of myeloid cells in PBMC revealed the
79 inflammatory environment of COVID-19.

30

31 Collectively, using the COVID-19 single cell atlas data exploration environment, we have
32 illustrated is that researchers are now enabled to systematically explore, learn, and formulate new
33 hypotheses within and between compartments, cell types, and biological processes, and provided
34 access to these reprocessed datasets through a suite of explorative and evaluative tools. Moreover,
35 we have shown different hypotheses can be developed and explored using the approaches that we
36 have outlined and the database that we have provided. Certainly additional critical information
37 will also be obtained using approaches that include in situ spatial, temporal data as well as those
38 of viral products and viral and inflammatory-process affected complexes. Next steps for
39 improving its ability to be mined more deeply will be based on additional statistical methods that
40 extend the current ToppCell / ToppGene Suite based on fuzzy measure similarity, Page-Rank, and
41 cell-cell signaling approaches.

42

43 There are several limitations in our study. Different studies used various standards of COVID-19
44 severity definition. To generalize conclusions, we simplified disease conditions into several
45 universal groups. Prospectively, a standardized definition of disease stages will assist to the
46 accuracy of future studies. Additionally, the timing of sample collection was not considered as a
47 variable in this study, rather disease stages were used to consolidate data across samples. We lack
48 follow-up data of patients with sequela, which will be helpful for understanding the long-haul
49 effects of the disease.

50

51

52 **Materials and Methods**

53

54 **Experimental design and single-cell RNA-seq data source**

55 To have a comprehensive understanding of immune cells in different repertoires, we collected 8
56 public COVID-19 single-cell RNA-seq datasets of multiple compartments, including peripheral
57 blood mononuclear cells, bronchoalveolar lavage and lung biopsy, which in total covered over 43
58 healthy donors, 22 mild/moderate, 42 severe and 2 convalescent COVID-19 patients. More details
59 can be found in Fig. 1A and table S1. Lung biopsy samples were taken from the explanted lung or
60 post-mortem lungs of COVID-19 patients (70). Various criteria were used in these publications to
61 describe COVID-19 severity. For example, we found asymptomatic, mild, moderate and floor

12 COVID-19 patients under the definition of non-severe COVID-19 patients in our data sources. A
13 recent paper used the WHO score of COVID-19 severity to categorize disease conditions of
14 patients (26), which is a more standardized and robust approach for the description of disease
15 stages. However, in order to address the issue of missing information for disease stratification and
16 to simplify the comparison, we grouped disease conditions into three groups, including healthy
17 donors, mild COVID-19 patients and severe COVID-19 patients. Convalescent patients were
18 excluded in some of our analysis for simplification. Sequencing data of healthy donors in Guo et
19 al. was excluded since it was not from the same institute (14).

20 We also collected PBMC single-cell RNA-seq data from 29 sepsis patients (61) and 4 multiple
21 sclerosis (62) patients for comparative analysis of immune-mediated diseases (Fig. 1A and table
22 S1). Data sources can be found in Data Availability.

23 24 **Data preprocessing and normalization**

25 For datasets with raw UMI counts, we first removed cells with less than 300 detected genes or
26 less than 600 UMI counts. Then cells with more than 15% counts of mitochondrial genes were
27 filtered out. Genes expressed in less than 5 cells were removed. After quality control, we finally
28 harvested 483,765 high-quality cells from 8 studies (table S1). We normalized the total UMI
29 counts per gene to 1 million (CPM) and applied $\log_2(\text{CPM}+1)$ transformation for heatmap
30 visualization and downstream differential gene expression analysis. Steps above were done in
31 Scanpy (71).

32 For some datasets that only provide processed and normalized *h5ad* or *rds* files, we checked their
33 preprocessing procedures in the original publications and confirmed that stringent quality control
34 procedures were used. Most of them used the default normalization approach in the Seurat or
35 Scanpy pipeline. We transferred them to $\log_2(\text{CPM}+1)$ to make data consistently normalized. We
36 also prepared corresponding raw count files for data integration.

37 38 **Integration of PBMC datasets and BAL datasets using Reciprocal PCA in Seurat**

39 We input raw count files of 5 preprocessed PBMC datasets into Seurat and created a list of Seurat
40 objects. Reciprocal PCA procedure ([https://satijalab.org/seurat/v3.2/integration.html#reciprocal-
41 pca](https://satijalab.org/seurat/v3.2/integration.html#reciprocal-pca)) was used for data integration. First, normalization and variable feature detection were
42 applied for each dataset in the list. Then we used *SelectIntegrationFeatures* to select features for
43 downstream integration. Next, we scaled data and ran the principal component analysis with
44 selected features using *ScaleData* and *RunPCA*. Then we found integration anchors and integrated

45 data using *FindIntegrationAchnors* and *IntegrateData*. RPCA was used as the reduction method.
46 After integration, we scaled data and ran PCA on integrated expression values. UMAP was
47 generated using the top 30 reduced dimensions with *RunUMAP*. The same approach was also
48 used in BAL data integration and multi-disease integration. We also used it for the integration of
49 specific cell types across multiple datasets, for example, the integration of neutrophils from
50 PBMC and BAL datasets. Compared with standard workflow and SCTransform
51 (<https://satijalab.org/seurat/v3.2/integration.html>) in Seurat, we found Reciprocal PCA is much
52 less computation-intensive and time-consuming, making the integration of multiple large single-
53 cell datasets feasible.

54

55 **Cell Annotations using canonical markers after unsupervised clustering**

56 Cell annotations were assigned in each dataset and then mapped to the integrated data. For some
57 datasets without available cell annotations, we first used unsupervised clustering in Scanpy.
58 Detailed steps include (1) detecting top 3,000 highly variable genes using
59 *pp.highly_variable_genes*; (2) scaling each gene to unit variance on highly variable genes using
60 *pp.scale*; (3) running PCA using *arpack* approach in *tl.pca*; (4) finding neighbors using
61 *pp.neighbors*; (5) running leiden clustering with resolution of 1 using *tl.leiden* (resolutions were
62 determined swiftly based on the size and complexity of data). More details can be found in the
63 code. For datasets with available annotations, we checked their validity and corrected wrong
64 annotations. For example, hematopoietic stem and progenitor cells (HSPC) were mistakenly
65 annotated as “SC&Eosinophil” in the original paper (11) and were corrected in our annotation.

66

67 After unsupervised clustering, well recognized immune cell markers were used to annotate
68 clusters, including CD4⁺ T cell markers such as TRAC, CD3D, CD3E, CD3G, CD4; CD8⁺ T cell
69 markers such as CD8A, CD8B, NKG7; NK cell markers such as NKG7, GNLY, KLRD1; B cell
70 markers such as CD19, MS4A1, CD79A; plasmablast markers such as MZB1, XBP1; monocyte
71 markers such as S100A8, S100A9, CST3, CD14; conventional dendritic cell markers such as
72 XCR1, plasmacytoid dendritic cell markers such as TCF4; megakaryocyte/platelet marker PPBP;
73 red blood cell markers HBA1, HBA2; HSPC marker CD34. Exhaustion-associated markers,
74 including PDCD1, HAVCR2, CTLA4 and LAG3 were used to identify exhausted T cells.

75

76 Additionally, other markers were used for annotations of lung-specific cells, including AGER,
77 MSLN for AT1 cells; SFTPC, SFTPB for AT2 cells; SCGB3A2, SCGB1A1 for Club cells;

78 TPPP3, FOXP3 for Ciliated cells; KRT5 for Basal cells; CFTR for Ionocytes; FABP4, CD68 for
79 tissue-resident macrophages; FCN1 for monocyte-derived macrophages, TPSB2 for Mast cells.
30 More details can be found in Table S2.

31 32 **Cell Annotations using Azimuth**

33 To better annotate T cells in our study, we applied Azimuth (<https://satijalab.org/azimuth/>), a tool
34 for reference-based single-cell analysis developed in Seurat version 4.0 (22). High-quality PBMC
35 single-cell data in Azimuth was used as the reference for label projection. After removing
36 annotations with low prediction scores or low mapping scores, we got a collection of well-
37 annotated T cell subtypes, including CD4+ Cytotoxic T cell, CD4+ Naive T cell, CD4+ Central
38 Memory T cell, CD8+ Naive T cell, CD8+ Effector Memory cell, gamma-delta T cell, double-
39 negative T cell. CD4+ Effector Memory T cell and CD8+ Central Memory T cell were found by
40 Azimuth but removed later because of low scores. Apart from annotations of T cell subtypes, we
41 also found CD56-bright NK cell, intermediate B cell and Memory B cell using Azimuth.

42 43 **Sub-clustering for specific cell types**

44 Sub-clustering was used for the discovery of subtypes or distinct stages of a specific cell type. In
45 our work, we applied sub-cluster for various immune cell types, including classical monocytes,
46 neutrophils, conventional dendritic, B cells and platelets. First, all cells in the specific cell type
47 were integrated using the same procedure as PBMC data integration. Then Louvain clustering
48 (resolution = 0.5, except for sub-clustering of classical monocytes where resolution = 0.3) was
49 applied to detect sub-clusters of those cells. Importantly, neutrophils, cDCs and B cells were
50 retrieved from both PBMC and BAL, whereas classical monocytes and platelets were only
51 retrieved from PBMC.

52 53 **Generation of ToppCell gene modules**

54 ToppCell (<https://toppcell.cchmc.org/>) was designed to parallelly analyze transcriptional profiles
55 of single-cell datasets by organizing differential expressed gene modules in a customized
56 hierarchical order. In our study, we hierarchically annotated cells with multiple layers, including
57 compartments, disease conditions, lineages, cell classes and sub-clusters. All the cells were
58 grouped into specific hierarchical categories. For example, “PBMC_severe COVID-19_myeloid
59 cells_classical-monocytes_cMono1” represents cells belonging to cMono1 (a sub-cluster of
60 classical monocytes) in PBMC of severe COVID-19 patients. With hierarchically ordered cell

11 annotations, we calculated their DEGs in a hierarchical way as well. We defined customized
12 ranges for comparisons and applied t-test based on normalized expression values. More details
13 can be seen on ToppCell website. Usually, the top 200 most differentially genes in each
14 comparison were picked up as the gene modules for the selected cell group, which are the starting
15 point of downstream analysis, including gene enrichment in ToppGene and interaction inference
16 in ToppCluster. All gene modules in our study were curated in COVID-19 Atlas
17 (<https://toppcell.cchmc.org/biosystems/go/index3/COVID-19 Atlas>) and ImmuneMap
18 (<https://toppcell.cchmc.org/biosystems/go/index3/ImmuneMap>) on the ToppCell website.

19

20 **Gene Enrichment Analysis using ToppGene**

21 Abundant gene modules were generated with ToppCell. After that, we used ToppGene
22 (<https://toppgene.cchmc.org/>) for gene enrichment analysis. Genes in each gene module were sent
23 to ToppGene platform as input for enrichment in different domains. GO-Molecular Function, GO-
24 Biological Process and GO-Cellular Component and Mouse Phenotype were usually used for
25 enrichment. P values of enrichment results were adjusted using the Benjamini-Hochberg
26 procedure.

27

28 **Generation of Functional Association Heatmap using ToppCluster**

29 Genes in gene modules of selected cell types or sub-clusters were sent to ToppCluster
30 (<https://toppcluster.cchmc.org/>). Then multi-group functional enrichment was drawn for input
31 gene modules and $-\log_{10}(\text{adjusted p-value})$ was used as the gene enrichment score to represent the
32 strength of association between gene modules and pathways. Scores greater than 10 were trimmed
33 to 10. Pathways from Gene Ontologies, including Molecular Functions, Biological Process and
34 Cellular Component in the option list were used for the enrichment of gene modules in myeloid
35 cells, B cells and platelets. In order to gain a broader knowledge of immunothrombosis-related
36 pathways, “Pathway” and “Mouse Phenotype” in the option list were also selected for enrichment.
37 Morpheus was used for visualization of the heatmap
38 (<https://software.broadinstitute.org/morpheus/>).

39

40 **Cell Interaction Inference in immunothrombosis activities and cytokine signaling pathways**

41 CellChat was used to infer the signaling network in the BAL of severe patients (fig. S8B). All 3
42 categories of interactions were used in the database *CellChatDB.human*. Over-expressed ligands
43 or receptors in each cell type were first identified for further identification of over-expressed

44 interaction pairs. Then cytokine, chemokine and IL signaling probability between multiple cell
45 types was inferred using *computeCommunProb* and *computeCommunProbPathway*.

46

47 ToppCell was used to infer interactions in immunothrombosis. We first selected genes related to
48 coagulation or immunothrombosis pathways from subtypes of endothelial cells, platelets,
49 neutrophils, classical monocytes and monocyte-derived macrophages by filtering the output of
50 ToppCluster (fig. S12A). Then we used CellChatDB as the knowledge base to find the subset of
51 genes participating in cell-cell interaction, including genes involved in signaling via secretion,
52 cell-cell contact and extracellular matrix interaction. These genes in each cluster were sent to
53 ToppCluster to infer the interaction network using protein-protein interactions (PPI) between
54 those genes.

55

56 **Generation of Volcano Plots**

57 We first calculated differential expressed genes using *tl.rank_genes_groups* in Scanpy. Adjusted
58 p values and log fold changes in the output were used as the input of volcano plots. R package
59 *EnhancedVolcano* (72) was used to draw figures.

60

61 **Construction of COVID-19 Functional Enrichment Map**

62 In order to characterize functional properties of cell types and subtypes observed in BAL, PBMC,
63 and lung parenchymal samples from control, mild, and severe COVID-19 patient samples, we
64 used the library of gene expression signatures (“Gene Module Report” from [ToppCell](#)) as an input
65 to the ToppCluster enrichment analyzer web server (Kaimal et al 2010). Using categories of *Gene*
66 *Ontology*, *Human Phenotype*, *Mouse Phenotype*, *Pathway* and *Protein Interaction*, a matrix was
67 constructed using minus log P enrichment values for each celltype gene list and then all cells and
68 enriched features could be clustered and ordered based on their shared or distinct properties that
69 could then be associated with lineage, cell subclass, tissue compartment, and disease state.

70

71 **Statistics Analysis of Cell Proportion Changes in Different Disease Stages**

72 Cell proportion differences between disease groups for specific types and subtypes (Fig. 2 and fig.
73 S2 to S4) shown on box plots were measured by Mann-Whitney test (Wilcoxon, paired=False).
74 Significance between two disease conditions were shown on the top.

75 To investigate the dynamic changes of cell proportions across various immune-mediated diseases,
76 we followed the approach in recent literature (12) (Fig. 7B). For each disease condition, we

77 computed the relative ratio of each cell type in individual disease samples divided by individual
78 healthy samples. Log₂ transformed values were shown in the box plot. Then we calculated
79 relative ratios of each cell type between all sample pairs of healthy donors as a control. To
80 compute the significance, we used a two-sided Kolmogorov-Smirnov (KS) test using relative
81 ratios in diseases and those values in healthy donors.

82

83 **References**

- 84 1. Y. Shi, Y. Wang, C. Shao, J. Huang, J. Gan, X. Huang, E. Bucci, M. Piacentini, G. Ippolito, G.
85 Melino, COVID-19 infection: the perspectives on immune responses. *Cell Death Differ.* **27**, 1451–
86 1454 (2020).
- 87 2. M. Z. Tay, C. M. Poh, L. Rénia, P. A. MacAry, L. F. P. Ng, The trinity of COVID-19: immunity,
88 inflammation and intervention. *Nat. Rev. Immunol.* **20**, 363–374 (2020).
- 89 3. X. Cao, COVID-19: immunopathology and its implications for therapy. *Nat. Rev. Immunol.* **20**,
90 269–270 (2020).
- 91 4. F. Wang, J. Nie, H. Wang, Q. Zhao, Y. Xiong, L. Deng, S. Song, Z. Ma, P. Mo, Y. Zhang,
92 Characteristics of Peripheral Lymphocyte Subset Alteration in COVID-19 Pneumonia. *J. Infect. Dis.*
93 **221**, 1762–1769 (2020).
- 94 5. S. F. Pedersen, Y.-C. Ho, SARS-CoV-2: a storm is raging. *J. Clin. Invest.* **130**, 2202–2205 (2020).
- 95 6. P. Mehta, D. F. McAuley, M. Brown, E. Sanchez, R. S. Tattersall, J. J. Manson, HLH Across
96 Speciality Collaboration, UK, COVID-19: consider cytokine storm syndromes and
97 immunosuppression. *Lancet.* **395**, 1033–1034 (2020).
- 98 7. D. Blanco-Melo, B. E. Nilsson-Payant, W.-C. Liu, S. Uhl, D. Hoagland, R. Møller, T. X. Jordan,
99 K. Oishi, M. Panis, D. Sachs, T. T. Wang, R. E. Schwartz, J. K. Lim, R. A. Albrecht, B. R. tenOever,
100 Imbalanced Host Response to SARS-CoV-2 Drives Development of COVID-19. *Cell.* **181**, 1036–
101 1045.e9 (2020).
- 102 8. J. Hadjadj, N. Yatim, L. Barnabei, A. Corneau, J. Boussier, N. Smith, H. Péré, B. Charbit, V.
103 Bondet, C. Chenevier-Gobeaux, P. Breillat, N. Carlier, R. Gauzit, C. Morbieu, F. Pène, N. Marin, N.
104 Roche, T.-A. Szwebel, S. H. Merklung, J.-M. Treluyer, D. Veyer, L. Mouthon, C. Blanc, P.-L.
105 Tharaux, F. Rozenberg, A. Fischer, D. Duffy, F. Rieux-Laucat, S. Kernéis, B. Terrier, Impaired type I
106 interferon activity and inflammatory responses in severe COVID-19 patients. *Science.* **369**, 718–724
107 (2020).

9. J. Schulte-Schrepping, N. Reusch, D. Paclik, K. Baßler, S. Schlickeiser, B. Zhang, B. Krämer, T. Krammer, S. Brumhard, L. Bonaguro, E. De Domenico, D. Wendisch, M. Grasshoff, T. S. Kapellos, M. Beckstette, T. Pecht, A. Saglam, O. Dietrich, H. E. Mei, A. R. Schulz, C. Conrad, D. Kunkel, E. Vafadarnejad, C.-J. Xu, A. Horne, M. Herbert, A. Drews, C. Thibeault, M. Pfeiffer, S. Hippenstiel, A. Hocke, H. Müller-Redetzky, K.-M. Heim, F. Machleidt, A. Uhrig, L. Bosquillon de Jarcy, L. Jürgens, M. Stegemann, C. R. Glösenkamp, H.-D. Volk, C. Goffinet, M. Landthaler, E. Wyler, P. Georg, M. Schneider, C. Dang-Heine, N. Neuwinger, K. Kappert, R. Tauber, V. Corman, J. Raabe, K. M. Kaiser, M. T. Vinh, G. Rieke, C. Meisel, T. Ulas, M. Becker, R. Geffers, M. Witzernath, C. Drosten, N. Suttorp, C. von Kalle, F. Kurth, K. Händler, J. L. Schultze, A. C. Aschenbrenner, Y. Li, J. Nattermann, B. Sawitzki, A.-E. Saliba, L. E. Sander, Deutsche COVID-19 OMICS Initiative (DeCOI), Severe COVID-19 Is Marked by a Dysregulated Myeloid Cell Compartment. *Cell*. **182**, 1419–1440.e23 (2020).
10. A. Silvin, N. Chapuis, G. Dunsmore, A.-G. Goubet, A. Dubuisson, L. Derosa, C. Almiere, C. Hénon, O. Kosmider, N. Droin, P. Rameau, C. Catelain, A. Alfaro, C. Dussiau, C. Friedrich, E. Sourdeau, N. Marin, T.-A. Szwebel, D. Cantin, L. Mouthon, D. Borderie, M. Deloger, D. Bredel, S. Mouraud, D. Drubay, M. Andrieu, A.-S. Lhonneur, V. Saada, A. Stoclin, C. Willekens, F. Pommeret, F. Griscelli, L. G. Ng, Z. Zhang, P. Bost, I. Amit, F. Barlesi, A. Marabelle, F. Pène, B. Gachot, F. André, L. Zitvogel, F. Ginhoux, M. Fontenay, E. Solary, Elevated Calprotectin and Abnormal Myeloid Cell Subsets Discriminate Severe from Mild COVID-19. *Cell*. **182** (2020), pp. 1401–1418.e18.
11. A. J. Wilk, A. Rustagi, N. Q. Zhao, J. Roque, G. J. Martínez-Colón, J. L. McKechnie, G. T. Ivison, T. Ranganath, R. Vergara, T. Hollis, L. J. Simpson, P. Grant, A. Subramanian, A. J. Rogers, C. A. Blish, A single-cell atlas of the peripheral immune response in patients with severe COVID-19. *Nature Medicine*. **26** (2020), pp. 1070–1076.
12. J. S. Lee, S. Park, H. W. Jeong, J. Y. Ahn, S. J. Choi, H. Lee, B. Choi, S. K. Nam, M. Sa, J.-S. Kwon, S. J. Jeong, H. K. Lee, S. H. Park, S.-H. Park, J. Y. Choi, S.-H. Kim, I. Jung, E.-C. Shin, Immunophenotyping of COVID-19 and influenza highlights the role of type I interferons in development of severe COVID-19. *Sci Immunol*. **5** (2020), doi:10.1126/sciimmunol.abd1554.
13. P. S. Arunachalam, F. Wimmers, C. K. P. Mok, R. A. P. M. Perera, M. Scott, T. Hagan, N. Sigal, Y. Feng, L. Bristow, O. Tak-Yin Tsang, D. Wagh, J. Coller, K. L. Pellegrini, D. Kazmin, G. Alaaeddine, W. S. Leung, J. M. C. Chan, T. S. H. Chik, C. Y. C. Choi, C. Huerta, M. Paine McCullough, H. Lv, E. Anderson, S. Edupuganti, A. A. Upadhyay, S. E. Bosinger, H. T. Maecker, P. Khatri, N. Roupheal, M. Peiris, B. Pulendran, Systems biological assessment of immunity to mild versus severe COVID-19 infection in humans. *Science*. **369**, 1210–1220 (2020).

- 42 14. C. Guo, B. Li, H. Ma, X. Wang, P. Cai, Q. Yu, L. Zhu, L. Jin, C. Jiang, J. Fang, Q. Liu, D. Zong,
43 W. Zhang, Y. Lu, K. Li, X. Gao, B. Fu, L. Liu, X. Ma, J. Weng, H. Wei, T. Jin, J. Lin, K. Qu, Single-
44 cell analysis of two severe COVID-19 patients reveals a monocyte-associated and tocilizumab-
45 responding cytokine storm. *Nat. Commun.* **11**, 3924 (2020).
- 46 15. M. Liao, Y. Liu, J. Yuan, Y. Wen, G. Xu, J. Zhao, L. Cheng, J. Li, X. Wang, F. Wang, L. Liu, I.
47 Amit, S. Zhang, Z. Zhang, Single-cell landscape of bronchoalveolar immune cells in patients with
48 COVID-19. *Nat. Med.* **26**, 842–844 (2020).
- 49 16. R. A. Grant, L. Morales-Nebreda, N. S. Markov, Alveolitis in severe SARS-CoV-2 pneumonia is
50 driven by self-sustaining circuits between infected alveolar macrophages and T cells. *bioRxiv* (2020)
51 (available at <https://www.biorxiv.org/content/10.1101/2020.08.05.238188v1.abstract>).
- 52 17. R. L. Chua, S. Lukassen, S. Trump, B. P. Hennig, D. Wendisch, F. Pott, O. Debnath, L.
53 Thürmann, F. Kurth, M. T. Völker, J. Kazmierski, B. Timmermann, S. Twardziok, S. Schneider, F.
54 Machleidt, H. Müller-Redetzky, M. Maier, A. Krannich, S. Schmidt, F. Balzer, J. Liebig, J. Loske, N.
55 Suttorp, J. Eils, N. Ishaque, U. G. Liebert, C. von Kalle, A. Hocke, M. Witzentrath, C. Goffinet, C.
56 Drosten, S. Laudi, I. Lehmann, C. Conrad, L.-E. Sander, R. Eils, COVID-19 severity correlates with
57 airway epithelium–immune cell interactions identified by single-cell analysis. *Nat. Biotechnol.* **38**,
58 970–979 (2020).
- 59 18. A. C. Yang, F. Kern, P. M. Losada, C. A. Maat, G. Schmartz, Broad transcriptional dysregulation
60 of brain and choroid plexus cell types with COVID-19. *bioRxiv* (2020) (available at
61 <https://www.biorxiv.org/content/10.1101/2020.10.22.349415v1.abstract>).
- 62 19. M. Heming, X. Li, S. Räuber, A. K. Mausberg, A.-L. Börsch, M. Hartlehnert, A. Singhal, I.-N.
63 Lu, M. Fleischer, F. Szepanowski, O. Witzke, T. Brenner, U. Dittmer, N. Yosef, C. Kleinschnitz, H.
64 Wiendl, M. Stettner, G. Meyer Zu Hörste, Neurological Manifestations of COVID-19 Feature T Cell
65 Exhaustion and Dedifferentiated Monocytes in Cerebrospinal Fluid. *Immunity*. **54**, 164–175.e6
66 (2021).
- 67 20. T. M. Delorey, C. G. K. Ziegler, G. Heimberg, R. Normand, Y. Yang, A. Segerstolpe, D.
68 Abbondanza, S. J. Fleming, A. Subramanian, D. T. Montoro, K. A. Jagadeesh, K. K. Dey, P. Sen, M.
69 Slyper, Y. H. Pita-Juárez, D. Phillips, Z. Bloom-Ackerman, N. Barkas, A. Ganna, J. Gomez, E.
70 Normandin, P. Naderi, Y. V. Popov, S. S. Raju, S. Niezen, L. T.-Y. Tsai, K. J. Siddle, M. Sud, V. M.
71 Tran, S. K. Vellarikkal, L. Amir-Zilberstein, D. S. Atri, J. Beechem, O. R. Brook, J. Chen, P.
72 Divakar, P. Dorceus, J. M. Engreitz, A. Essene, D. M. Fitzgerald, R. Fropf, S. Gazal, J. Gould, J.
73 Grzyb, T. Harvey, J. Hecht, T. Hether, J. Jane-Valbuena, M. Leney-Greene, H. Ma, C. McCabe, D. E.
74 McLoughlin, E. M. Miller, C. Muus, M. Niemi, R. Padera, L. Pan, D. Pant, C. Pe’er, J. Pfiffner-

- 75 Borges, C. J. Pinto, J. Plaisted, J. Reeves, M. Ross, M. Rudy, E. H. Rueckert, M. Siciliano, A. Sturm,
76 E. Todres, A. Waghray, S. Warren, S. Zhang, D. R. Zollinger, L. Cosimi, R. M. Gupta, N. Hacohen,
77 W. Hide, A. L. Price, J. Rajagopal, P. R. Tata, S. Riedel, G. Szabo, T. L. Tickle, D. Hung, P. C.
78 Sabeti, R. Novak, R. Rogers, D. E. Ingber, Z. Gordon Jiang, D. Juric, M. Babadi, S. L. Farhi, J. R.
79 Stone, I. S. Vlachos, I. H. Solomon, O. Ashenberg, C. B. M. Porter, B. Li, A. K. Shalek, A.-C.
80 Villani, O. Rozenblatt-Rosen, A. Regev, A single-cell and spatial atlas of autopsy tissues reveals
81 pathology and cellular targets of SARS-CoV-2. *bioRxiv* (2021), doi:10.1101/2021.02.25.430130.
- 82 21. T. Stuart, A. Butler, P. Hoffman, C. Hafemeister, E. Papalexi, W. M. Mauck 3rd, Y. Hao, M.
83 Stoeckius, P. Smibert, R. Satija, Comprehensive Integration of Single-Cell Data. *Cell*. **177**, 1888–
84 1902.e21 (2019).
- 85 22. Y. Hao, S. Hao, E. Andersen-Nissen, W. M. Mauck, S. Zheng, A. Butler, M. J. Lee, A. J. Wilk, C.
86 Darby, M. Zagar, P. Hoffman, M. Stoeckius, E. Papalexi, E. P. Mimitou, J. Jain, A. Srivastava, T.
87 Stuart, L. B. Fleming, B. Yeung, A. J. Rogers, J. M. McElrath, C. A. Blish, R. Gottardo, P. Smibert,
88 R. Satija, Integrated analysis of multimodal single-cell data. *Cold Spring Harbor Laboratory* (2020),
89 p. 2020.10.12.335331.
- 90 23. V. Kaimal, E. E. Bardes, S. C. Tabar, A. G. Jegga, B. J. Aronow, ToppCluster: a multiple gene list
91 feature analyzer for comparative enrichment clustering and network-based dissection of biological
92 systems. *Nucleic Acids Res.* **38**, W96–102 (2010).
- 93 24. A. G. Laing, A. Lorenc, I. Del Molino Del Barrio, A. Das, M. Fish, L. Monin, M. Muñoz-Ruiz, D.
94 R. McKenzie, T. S. Hayday, I. Francos-Quijorna, S. Kamdar, M. Joseph, D. Davies, R. Davis, A.
95 Jennings, I. Zlatareva, P. Vantourout, Y. Wu, V. Sofra, F. Cano, M. Greco, E. Theodoridis, J. D.
96 Freedman, S. Gee, J. N. E. Chan, S. Ryan, E. Bugallo-Blanco, P. Peterson, K. Kisand, L. Haljasmägi,
97 L. Chadli, P. Moingeon, L. Martinez, B. Merrick, K. Bisnauthsing, K. Brooks, M. A. A. Ibrahim, J.
98 Mason, F. Lopez Gomez, K. Babalola, S. Abdul-Jawad, J. Cason, C. Mant, J. Seow, C. Graham, K. J.
99 Doores, F. Di Rosa, J. Edgeworth, M. Shankar-Hari, A. C. Hayday, Author Correction: A dynamic
00 COVID-19 immune signature includes associations with poor prognosis. *Nat. Med.* **26**, 1951 (2020).
- 01 25. R. He, Z. Lu, L. Zhang, T. Fan, R. Xiong, X. Shen, H. Feng, H. Meng, W. Lin, W. Jiang, Q.
02 Geng, The clinical course and its correlated immune status in COVID-19 pneumonia. *J. Clin. Virol.*
03 **127**, 104361 (2020).
- 04 26. A. J. Wilk, M. J. Lee, B. Wei, B. Parks, R. Pi, G. J. Martínez-Colón, T. Ranganath, N. Q. Zhao, S.
05 Taylor, W. Becker, S. C.-19 Biobank, D. Jimenez-Morales, A. L. Blomkalns, R. O’Hara, E. A.
06 Ashley, K. C. Nadeau, S. Yang, S. Holmes, M. Rabinovitch, A. J. Rogers, W. J. Greenleaf, C. A.
07 Blish, Multi-omic profiling reveals widespread dysregulation of innate immunity and hematopoiesis

in COVID-19. *Cold Spring Harbor Laboratory* (2020), p. 2020.12.18.423363.

27. E. Terpos, I. Ntanasis-Stathopoulos, I. Elalamy, E. Kastritis, T. N. Sergentanis, M. Politou, T. Psaltopoulou, G. Gerotziafas, M. A. Dimopoulos, Hematological findings and complications of COVID-19. *Am. J. Hematol.* **95**, 834–847 (2020).

28. S. De Biasi, D. Lo Tartaro, M. Meschiari, L. Gibellini, C. Bellinazzi, R. Borella, L. Fidanza, M. Mattioli, A. Paolini, L. Gozzi, D. Jaacoub, M. Faltoni, S. Volpi, J. Milić, M. Sita, M. Sarti, C. Pucillo, M. Girardis, G. Guaraldi, C. Mussini, A. Cossarizza, Expansion of plasmablasts and loss of memory B cells in peripheral blood from COVID-19 patients with pneumonia. *Eur. J. Immunol.* **50**, 1283–1294 (2020).

29. E. A. Middleton, X.-Y. He, F. Denorme, R. A. Campbell, D. Ng, S. P. Salvatore, M. Mostyka, A. Baxter-Stoltzfus, A. C. Borczuk, M. Loda, M. J. Cody, B. K. Manne, I. Portier, E. S. Harris, A. C. Petrey, E. J. Beswick, A. F. Caulin, A. Iovino, L. M. Abegglen, A. S. Weyrich, M. T. Rondina, M. Egeblad, J. D. Schiffman, C. C. Yost, Neutrophil extracellular traps contribute to immunothrombosis in COVID-19 acute respiratory distress syndrome. *Blood.* **136**, 1169–1179 (2020).

30. L. Nicolai, A. Leunig, S. Brambs, R. Kaiser, T. Weinberger, M. Weigand, M. Muenchhoff, J. C. Hellmuth, S. Ledderose, H. Schulz, C. Scherer, M. Rudelius, M. Zoller, D. Höchter, O. Keppler, D. Teupser, B. Zwißler, M. von Bergwelt-Baildon, S. Kääh, S. Massberg, K. Pekayvaz, K. Stark, Immunothrombotic Dysregulation in COVID-19 Pneumonia Is Associated With Respiratory Failure and Coagulopathy. *Circulation.* **142**, 1176–1189 (2020).

31. M. Merad, J. C. Martin, Author Correction: Pathological inflammation in patients with COVID-19: a key role for monocytes and macrophages. *Nat. Rev. Immunol.* **20**, 448 (2020).

32. D. McGonagle, K. Sharif, A. O'Regan, C. Bridgewood, The Role of Cytokines including Interleukin-6 in COVID-19 induced Pneumonia and Macrophage Activation Syndrome-Like Disease. *Autoimmun. Rev.* **19**, 102537 (2020).

33. B. J. Barnes, J. M. Adrover, A. Baxter-Stoltzfus, A. Borczuk, J. Cools-Lartigue, J. M. Crawford, J. Daßler-Plenker, P. Guerci, C. Huynh, J. S. Knight, M. Loda, M. R. Looney, F. McAllister, R. Rayes, S. Renaud, S. Rousseau, S. Salvatore, R. E. Schwartz, J. D. Spicer, C. C. Yost, A. Weber, Y. Zuo, M. Egeblad, Targeting potential drivers of COVID-19: Neutrophil extracellular traps. *J. Exp. Med.* **217** (2020), doi:10.1084/jem.20200652.

34. T. Iba, J. H. Levy, J. M. Connors, T. E. Warkentin, J. Thachil, M. Levi, The unique characteristics of COVID-19 coagulopathy. *Crit. Care.* **24**, 360 (2020).

- 39 35. M. Levi, J. Thachil, T. Iba, J. H. Levy, Coagulation abnormalities and thrombosis in patients with
40 COVID-19. *The Lancet Haematology*. **7** (2020), pp. e438–e440.
- 41 36. A. V. Rapkiewicz, X. Mai, S. E. Carsons, S. Pittaluga, D. E. Kleiner, J. S. Berger, S. Thomas, N.
42 M. Adler, D. M. Charytan, B. Gasmi, J. S. Hochman, H. R. Reynolds, Megakaryocytes and platelet-
43 fibrin thrombi characterize multi-organ thrombosis at autopsy in COVID-19: A case series.
44 *EClinicalMedicine*. **24**, 100434 (2020).
- 45 37. M. Aid, K. Busman-Sahay, S. J. Vidal, Z. Maliga, S. Bondoc, C. Starke, M. Terry, C. A.
46 Jacobson, L. Wrijil, S. Ducat, O. R. Brook, A. D. Miller, M. Porto, K. L. Pellegrini, M. Pino, T. N.
47 Hoang, A. Chandrashekar, S. Patel, K. Stephenson, S. E. Bosinger, H. Andersen, M. G. Lewis, J. L.
48 Hecht, P. K. Sorger, A. J. Martinot, J. D. Estes, D. H. Barouch, Vascular Disease and Thrombosis in
49 SARS-CoV-2-Infected Rhesus Macaques. *Cell*. **183**, 1354–1366.e13 (2020).
- 50 38. N. H. Schultz, I. H. Sørvoll, A. E. Michelsen, L. A. Munthe, F. Lund-Johansen, M. T. Ahlen, M.
51 Wiedmann, A.-H. Aamodt, T. H. Skattør, G. E. Tjønnfjord, P. A. Holme, Thrombosis and
52 Thrombocytopenia after ChAdOx1 nCoV-19 Vaccination. *N. Engl. J. Med.* (2021),
53 doi:10.1056/NEJMoa2104882.
- 54 39. C. Osterholm, L. Folkersen, M. Lengquist, F. Pontén, T. Renné, J. Li, U. Hedin, Increased
55 expression of heparanase in symptomatic carotid atherosclerosis. *Atherosclerosis*. **226**, 67–73 (2013).
- 56 40. F. Swieringa, H. M. H. Spronk, J. W. M. Heemskerk, P. E. J. van der Meijden, Integrating platelet
57 and coagulation activation in fibrin clot formation. *Res Pract Thromb Haemost*. **2**, 450–460 (2018).
- 58 41. E. Sparkenbaugh, R. Pawlinski, Interplay between coagulation and vascular inflammation in
59 sickle cell disease. *Br. J. Haematol*. **162**, 3–14 (2013).
- 30 42. E. Edovitsky, I. Lerner, E. Zcharia, T. Peretz, I. Vlodaysky, M. Elkin, Role of endothelial
31 heparanase in delayed-type hypersensitivity. *Blood*. **107**, 3609–3616 (2006).
- 32 43. T. Iba, J. M. Connors, J. H. Levy, The coagulopathy, endotheliopathy, and vasculitis of COVID-
33 19. *Inflamm. Res*. **69**, 1181–1189 (2020).
- 34 44. J. W. M. Heemskerk, N. J. A. Mattheij, J M E, Platelet-based coagulation: different populations,
35 different functions. *Journal of Thrombosis and Haemostasis*. **11** (2013), pp. 2–16.
- 36 45. M. Ehrenfeld, A. Tincani, L. Andreoli, M. Cattalini, A. Greenbaum, D. Kanduc, J. Alijotas-Reig,
37 V. Zinserling, N. Semenova, H. Amital, Y. Shoenfeld, Covid-19 and autoimmunity. *Autoimmun. Rev*.
38 **19**, 102597 (2020).

- 39 46. Y. Rodríguez, L. Novelli, M. Rojas, M. De Santis, Y. Acosta-Ampudia, D. M. Monsalve, C.
70 Ramírez-Santana, A. Costanzo, W. M. Ridgway, A. A. Ansari, M. E. Gershwin, C. Selmi, J.-M.
71 Anaya, Autoinflammatory and autoimmune conditions at the crossroad of COVID-19. *J. Autoimmun.*
72 **114**, 102506 (2020).
- 73 47. C. N. Gruber, R. S. Patel, R. Trachtman, L. Lepow, F. Amanat, F. Krammer, K. M. Wilson, K.
74 Onel, D. Geanon, K. Tuballes, M. Patel, K. Mouskas, T. O'Donnell, E. Merritt, N. W. Simons, V.
75 Barcessat, D. M. Del Valle, S. Udondem, G. Kang, S. Gangadharan, G. Ofori-Amanfo, U. Laserson,
76 A. Rahman, S. Kim-Schulze, A. W. Charney, S. Gnjatich, B. D. Gelb, M. Merad, D. Bogunovic,
77 Mapping Systemic Inflammation and Antibody Responses in Multisystem Inflammatory Syndrome in
78 Children (MIS-C). *Cell*. **183**, 982–995.e14 (2020).
- 79 48. H. Fujii, T. Tsuji, T. Yuba, S. Tanaka, Y. Suga, A. Matsuyama, A. Omura, S. Shiotsu, C. Takumi,
30 S. Ono, M. Horiguchi, N. Hiraoka, High levels of anti-SSA/Ro antibodies in COVID-19 patients with
31 severe respiratory failure: a case-based review. *Clin. Rheumatol.* **39**, 3171–3175 (2020).
- 32 49. Y. Zhou, T. Han, J. Chen, C. Hou, L. Hua, S. He, Y. Guo, S. Zhang, Y. Wang, J. Yuan, C. Zhao,
33 J. Zhang, Q. Jia, X. Zuo, J. Li, L. Wang, Q. Cao, E. Jia, Clinical and autoimmune characteristics of
34 severe and critical cases of COVID-19. *Clin. Transl. Sci.* **13**, 1077–1086 (2020).
- 35 50. D. Y. Mason, J. L. Cordell, M. H. Brown, J. Borst, M. Jones, K. Pulford, E. Jaffe, E. Ralfkiaer, F.
36 Dallenbach, H. Stein, CD79a: a novel marker for B-cell neoplasms in routinely processed tissue
37 samples. *Blood*. **86**, 1453–1459 (1995).
- 38 51. S. Jin, C. F. Guerrero-Juarez, L. Zhang, I. Chang, P. Myung, M. V. Plikus, Q. Nie, Inference and
39 analysis of cell-cell communication using CellChat. *Cold Spring Harbor Laboratory* (2020), p.
40 2020.07.21.214387.
- 41 52. G. Aust, D. Sittig, L. Becherer, U. Anderegg, A. Schütz, P. Lamesch, E. Schmücking, The role of
42 CXCR5 and its ligand CXCL13 in the compartmentalization of lymphocytes in thyroids affected by
43 autoimmune thyroid diseases. *Eur. J. Endocrinol.* **150**, 225–234 (2004).
- 44 53. H.-T. Lee, Y.-M. Shiao, T.-H. Wu, W.-S. Chen, Y.-H. Hsu, S.-F. Tsai, C.-Y. Tsai, Serum
45 BLC/CXCL13 concentrations and renal expression of CXCL13/CXCR5 in patients with systemic
46 lupus erythematosus and lupus nephritis. *J. Rheumatol.* **37**, 45–52 (2010).
- 47 54. O. M. Steinmetz, J. Velden, U. Kneissler, M. Marx, A. Klein, U. Helmchen, R. A. K. Stahl, U.
48 Panzer, Analysis and classification of B-cell infiltrates in lupus and ANCA-associated nephritis.
49 *Kidney Int.* **74**, 448–457 (2008).

- 00 55. T. Kuwabara, F. Ishikawa, T. Yasuda, K. Aritomi, H. Nakano, Y. Tanaka, Y. Okada, M. Lipp, T.
01 Kakiuchi, CCR 7 Ligands Are Required for Development of Experimental Autoimmune
02 Encephalomyelitis through Generating IL-23-Dependent Th17 Cells. *The Journal of Immunology*.
03 **183**, 2513–2521 (2009).
- 04 56. K. Hirota, H. Yoshitomi, M. Hashimoto, S. Maeda, S. Teradaira, N. Sugimoto, T. Yamaguchi, T.
05 Nomura, H. Ito, T. Nakamura, N. Sakaguchi, S. Sakaguchi, Preferential recruitment of CCR6-
06 expressing Th17 cells to inflamed joints via CCL20 in rheumatoid arthritis and its animal model. *J.*
07 *Exp. Med.* **204**, 2803–2812 (2007).
- 08 57. E. Klimatcheva, T. Pandina, C. Reilly, S. Torno, H. Bussler, M. Scrivens, A. Jonason, C. Mallow,
09 M. Doherty, M. Paris, E. S. Smith, M. Zauderer, CXCL13 antibody for the treatment of autoimmune
10 disorders. *BMC Immunol.* **16**, 6 (2015).
- 11 58. C. K. Wong, P. T. Y. Wong, L. S. Tam, E. K. Li, D. P. Chen, C. W. K. Lam, Elevated production
12 of B cell chemokine CXCL13 is correlated with systemic lupus erythematosus disease activity. *J.*
13 *Clin. Immunol.* **30**, 45–52 (2010).
- 14 59. F. Zhang, K. Wei, K. Slowikowski, C. Y. Fonseka, D. A. Rao, S. Kelly, S. M. Goodman, D.
15 Tabechian, L. B. Hughes, K. Salomon-Escoto, G. F. M. Watts, A. H. Jonsson, J. Rangel-Moreno, N.
16 Meednu, C. Rozo, W. Apruzzese, T. M. Eisenhaure, D. J. Lieb, D. L. Boyle, A. M. Mandelin 2nd,
17 Accelerating Medicines Partnership Rheumatoid Arthritis and Systemic Lupus Erythematosus (AMP
18 RA/SLE) Consortium, B. F. Boyce, E. DiCarlo, E. M. Gravallesse, P. K. Gregersen, L. Moreland, G.
19 S. Firestein, N. Hacohen, C. Nusbaum, J. A. Lederer, H. Perlman, C. Pitzalis, A. Filer, V. M. Holers,
20 V. P. Bykerk, L. T. Donlin, J. H. Anolik, M. B. Brenner, S. Raychaudhuri, Defining inflammatory
21 cell states in rheumatoid arthritis joint synovial tissues by integrating single-cell transcriptomics and
22 mass cytometry. *Nat. Immunol.* **20**, 928–942 (2019).
- 23 60. A. Arazi, D. A. Rao, C. C. Berthier, A. Davidson, Y. Liu, P. J. Hoover, A. Chicoine, T. M.
24 Eisenhaure, A. H. Jonsson, S. Li, D. J. Lieb, F. Zhang, K. Slowikowski, E. P. Browne, A. Noma, D.
25 Sutherby, S. Steelman, D. E. Smilek, P. Tosta, W. Apruzzese, E. Massarotti, M. Dall’Era, M. Park, D.
26 L. Kamen, R. A. Furie, F. Payan-Schober, W. F. Pendergraft 3rd, E. A. McInnis, J. P. Buyon, M. A.
27 Petri, C. Putterman, K. C. Kalunian, E. S. Woodle, J. A. Lederer, D. A. Hildeman, C. Nusbaum, S.
28 Raychaudhuri, M. Kretzler, J. H. Anolik, M. B. Brenner, D. Wofsy, N. Hacohen, B. Diamond,
29 Accelerating Medicines Partnership in SLE network, The immune cell landscape in kidneys of
30 patients with lupus nephritis. *Nat. Immunol.* **20**, 902–914 (2019).
- 31 61. M. Reyes, M. R. Filbin, R. P. Bhattacharyya, K. Billman, T. Eisenhaure, D. T. Hung, B. D. Levy,
32 R. M. Baron, P. C. Blainey, M. B. Goldberg, N. Hacohen, An immune-cell signature of bacterial

- 33 sepsis. *Nat. Med.* **26**, 333–340 (2020).
- 34 62. D. Schafflick, C. A. Xu, M. Hartlehnert, M. Cole, A. Schulte-Mecklenbeck, T. Lautwein, J.
35 Wolbert, M. Heming, S. G. Meuth, T. Kuhlmann, C. C. Gross, H. Wiendl, N. Yosef, G. M. zu Horste,
36 Integrated single cell analysis of blood and cerebrospinal fluid leukocytes in multiple sclerosis.
37 *Nature Communications*. **11** (2020), , doi:10.1038/s41467-019-14118-w.
- 38 63. M. Zhao, Cytokine storm and immunomodulatory therapy in COVID-19: Role of chloroquine and
39 anti-IL-6 monoclonal antibodies. *Int. J. Antimicrob. Agents*. **55**, 105982 (2020).
- 40 64. K. J. Goodall, I. K. H. Poon, S. Phipps, M. D. Hulett, Soluble heparan sulfate fragments generated
41 by heparanase trigger the release of pro-inflammatory cytokines through TLR-4. *PLoS One*. **9**,
42 e109596 (2014).
- 43 65. K. M. Jayatilleke, M. D. Hulett, Heparanase and the hallmarks of cancer. *J. Transl. Med.* **18**, 453
44 (2020).
- 45 66. Y. Zuo, M. Zuo, S. Yalavarthi, K. Gockman, J. A. Madison, H. Shi, W. Woodard, S. P. Lezak, N.
46 L. Lugogo, J. S. Knight, Y. Kanthi, Neutrophil extracellular traps and thrombosis in COVID-19. *J.*
47 *Thromb. Thrombolysis*. **51**, 446–453 (2021).
- 48 67. C. Thålin, Y. Hisada, S. Lundström, N. Mackman, H. Wallén, Neutrophil Extracellular Traps:
49 Villains and Targets in Arterial, Venous, and Cancer-Associated Thrombosis. *Arterioscler. Thromb.*
50 *Vasc. Biol.* **39**, 1724–1738 (2019).
- 51 68. A. D. Farris, J. M. Guthridge, Overlapping B cell pathways in severe COVID-19 and lupus. *Nat.*
52 *Immunol.* **21**, 1478–1480 (2020).
- 53 69. S. Spoerl, A. N. Kremer, M. Aigner, N. Eisenhauer, P. Koch, L. Meretuk, P. Löffler, M.
54 Tenbusch, C. Maier, K. Überla, L. Heinzlerling, B. Frey, G. Lutzny-Geier, T. H. Winkler, G. Krönke,
55 M. Vetter, H. Bruns, M. F. Neurath, A. Mackensen, A. E. Kremer, S. Völkl, Upregulation of CCR4 in
56 activated CD8+ T cells indicates enhanced lung homing in patients with severe acute SARS-CoV-2
57 infection. *Eur. J. Immunol.* (2021), doi:10.1002/eji.202049135.
- 58 70. A. Bharat, M. Querrey, N. S. Markov, S. Kim, C. Kurihara, R. Garza-Castillon, A. Manerikar, A.
59 Shilatifard, R. Tomic, Y. Politanska, H. Abdala-Valencia, A. V. Yeldandi, J. W. Lomasney, A. V.
60 Misharin, G. R. S. Budinger, Lung transplantation for patients with severe COVID-19. *Sci. Transl.*
61 *Med.* **12** (2020), doi:10.1126/scitranslmed.abe4282.
- 62 71. F. A. Wolf, P. Angerer, F. J. Theis, SCANPY: large-scale single-cell gene expression data
63 analysis. *Genome Biol.* **19**, 15 (2018).

72. K. Blighe, S. Rana, M. Lewis, EnhancedVolcano: Publication-Ready Volcano Plots With
Enhanced Colouring and Labeling.(2019). *R Package Version. 1* (2018).

Acknowledgments

We thank Pablo Garcia-Nieto, Ambrose Carr and Jonah Cool and the Chan Zuckerberg Initiative for hosting the data on cellxgene. We acknowledge suggestions and help from Greta Beekhuis. We thank the support from Pediatric Cell Atlas and high performance computational cluster of CCHMC. Some figures were created using <https://biorender.com>. **Funding:** Funding for this study was provided by LungMap (U24 and HL148865), Digestive Health Center (P30, DK078392) and Harold C. Schott Foundation funding of the Harold C. Schott Endowed Chair, UC College of Medicine. **Author contributions:** Conceptualization, K.J. and B.A.; Methodology, K.J., B.A. and E.B.; Investigation, K.J. and B.A.; Writing – Original Draft, K.J.; Writing – Review & Editing, K.J., B.A., M.E.R., A.M., D.A.P.K, S.S.G. and S.B.; Funding Acquisition, B.A.; Resources, K.J.; Data Curation, K.J. and E.B.; Visualization, E.B.; Supervision, B.A.. **Competing interests:** Authors declare that they have no competing interests. **Data and materials availability:** Public single-cell RNA-seq datasets of PBMC in COVID-19 patients are available on NCBI Gene Expression Omnibus and European Genome-phenome Archive, including [GSE150728](#), [GSE155673](#), [GSE150861](#), [GSE149689](#) and EGAS00001004571 (or [FastGenomics](#)). BAL single-cell RNA-seq datasets of COVID-19 patients are available on [GSE145926](#) and [GSE155249](#). Lung Parenchyma single-cell RNA-seq data are available on [GSE158127](#). Single-cell RNA-seq data of sepsis patients are available on the Single Cell Portal [SCP548](#) and [SCP550](#). Data of multiple sclerosis patients are available on [GSE128266](#). Data of severe influenza patients are available on [GSE149689](#). Gene modules of all datasets analyzed using ToppCell web portal are available on COVID-19 Atlas in [ToppCell](#), including gene modules from either a single dataset or an integrated dataset. Gene modules from the integration of specific cell types, such as B cells and neutrophils are also listed in ToppCell. More details are listed in Fig. 1A and table S1. An interactive interface of integrated PBMC data and subclusters of immune cells will be public on [cellxgene](#) upon publication. Codes of preprocessing, normalization, clustering and plotting of single-cell datasets will be available on [github](#) upon publication.

98 **Figures and Tables**

99

100 **Fig. 1. Creating a COVID-19 Signature Atlas.** (A) Representative aggregation of multiple
101 single-cell RNA-sequencing datasets from COVID-19 and related studies. The present study is
102 derived from a total of 231,800 peripheral blood mononuclear cells (PBMCs), 101,800
103 bronchoalveolar lavage (BAL) cells and 146,361 lung parenchyma cells from 43 healthy; 22 mild,
104 42 severe, and 2 convalescent patients. Data was collated from eight public datasets (right). (B)
105 Data analysis pipeline of the study using Topp-toolkit. It includes three phases: (1) clustering and
106 annotation; (2) downstream analysis using Topp-toolkit; (3) biological exploration. Output
107 includes the evaluation of abundance of cell populations, cell type (cluster) specific gene
108 modules, functional associations of disease-associated cell classes and clusters, inference of cell-
109 cell interactions, as well as comparative analysis across diseases, including influenza, sepsis and
110 multiple sclerosis. Additional newer datasets not included in this manuscript are present and will
111 continue to be added to ToppCell (<http://toppcell.cchmc.org>).

112

113 **Fig. 2. Modularized representation of cell type specific gene signatures and dynamic**
114 **changes of cell abundance.** (A) Uniform Manifold Approximation and Projection (UMAP) of 28
115 distinct cell types identified in the integrated peripheral blood mononuclear cell (PBMC) data. (B)
116 Comparative analysis of cell abundance effects of COVID-19. Reproducible multi-study data
117 present high impact effects on 5 cell types in PBMC. Percentages of selected cell types in each
118 sample are shown (where Vent: Ventilated patients; Non Vent: Non-ventilated patients).
119 Significance between two conditions was measured by the Mann-Whitney rank sum test
120 (Wilcoxon, paired=False), which was also used in following significance tests of cell abundance
121 changes in this study. *: $p \leq 0.05$; **: $p \leq 0.01$; ***: $p \leq 0.001$; ****: $p \leq 0.0001$. (C)
122 UMAP of 24 distinct cell types identified in the integrated BAL data. (D) Dynamic changes of
123 cell abundances for cell types in two bronchoalveolar lavage (BAL) single-cell datasets. (E)
124 ToppCell allows for gene signatures to be hierarchically organized by lineage, cell type, subtype,
125 and disease condition. The global heatmap shows gene modules with top 50 upregulated genes
126 (student t test) for each cell type in a specific disease condition and compartment. Gene modules
127 from control donors and severe COVID-19 patients were included in the figure.

128

129 **Fig. 3. Functional analysis of compartment-specific immature and subtype-differentiated**
130 **neutrophils and monocytic macrophages in COVID-19 patients.** (A) Five sub-clusters and
131 three cell groups were identified after the integration of neutrophils in peripheral blood

32 mononuclear cells (PBMC) and bronchoalveolar lavage (BAL) (Left). The distribution of
33 compartments is shown on the right. **(B)** Sub-clusters (Left) and COVID-19 conditions (Right) of
34 monocyte-derived macrophages and tissue-resident macrophages were identified after integration
35 of BAL datasets. **(C)** Heatmap of gene modules from ToppCell with top 200 upregulated genes
36 for each neutrophil sub-cluster. Important neutrophil-associated genes and inferred roles of sub-
37 clusters were shown on two sides. **(D)** Heatmap of associations between subclusters of
38 neutrophils and macrophages and myeloid-cell-associated pathways (Gene Ontology). Gene
39 modules with 200 upregulated genes for sub-clusters; these were used for enrichment in ToppCluster.
40 Additionally, enrichment of top 200 differentially expressed genes (DEGs) for comparisons in fig.
41 S5D and fig. S6B were appended on the right. Gene enrichment scores, defined as $-\log_{10}(\text{adjusted}$
42 $p\text{-value})$, were calculated as the strength of associations. Pie charts showed the proportions of
43 COVID-19 conditions in each cluster. **(E)** Gene interaction network in the BAL of severe
44 patients. Highly expressed ligands and receptors of each cell type were drawn based on fig. S8.
45 Interaction was inferred using both CellChat database and embedded cell interaction database in
46 ToppCell.

47

48 **Fig. 4. COVID-19 driven reprogramming of platelets leads to drastically altered expression**
49 **of genes associated with platelet adhesion, activation, coagulation and thrombosis. (A-B)**

50 Uniform Manifold Approximation and Projections (UMAPs) show distributions of sub-clusters
51 (A) and COVID-19 conditions (B) of platelets after the integration of PBMC datasets. **(C)**
52 Severity-associated coagulation genes were selected and shown on the heatmap, with disease and
53 sub-cluster specific gene patterns identified and labeled. Their functional associations with
54 coagulation pathways were retrieved from ToppGene and shown on the right. **(D)** Functional and
55 phenotypical associations of coagulation-association genes in each gene pattern from (B).
56 Associations were retrieved from ToppGene enrichment. Fibrinolysis is highlighted.

57

58 **Fig. 5. Implicating a multi-lineage cell network capable of driving extrafollicular B cell**
59 **maturation and the emergence of humoral autoimmunity in COVID-19 patients. (A)**

60 Uniform Manifold Approximation and Projections (UMAPs) of sub-clusters (Left) and COVID-
61 19 conditions (Right) of B cells after integration of peripheral blood mononuclear cells (PBMC)
62 and bronchoalveolar lavage (BAL) datasets. **(B)** UMAPs of subtypes (Left) and COVID-19
63 conditions (Right) of plasmablasts after integration of PBMC and BAL datasets. **(C)** Volcano plot
64 depicts differentially expressed genes between plasmablasts and developing plasmablasts. Student

35 t-tests were applied and p values were adjusted by the Benjamini-Hochberg procedure. **(D)**
36 Workflow of discovering and prioritizing candidate genes related to a disease-specific phenotype
37 with limited understanding. **(E)** The heatmap shows the normalized expression levels of candidate
38 ligands and receptors for COVID-19 autoimmunity in multiple compartments in healthy donors
39 and COVID-19 patients. Binding ligands of receptor genes were shown in parentheses on the
40 right. Hot spots of expression are highlighted. **(F)** Network analysis of autoimmunity-associated
41 gene expression by COVID-19 cell types. Prior knowledge associated gene associations include
42 GWAS, OMIM, mouse knockout phenotype, and additional recent manuscripts were selected
43 from ToppGene enrichment results of differentially expressed ligands and receptors and shown on
44 the network. Orange arrows present the interaction directions from ligands (green) to receptors
45 (pink) on B cells. Annotations for these genes, including single-cell co-expression (blue), mouse
46 phenotype (light blue), transcription factor binding site (purple) and signaling pathways (green)
47 are shown.

48

49 **Fig. 6. Comparative analysis of cell type specific gene signatures associated with lineage,**
50 **class, subclass, compartment, and disease state in the COVID-19 atlas.** **(A)** Enrichment scores
51 of gene modules for all cell types across different compartments and COVID-19 conditions were
52 generated by ToppCluster and shown on the heatmap. ToppCluster enriched functions from Gene
53 Ontology, Human Phenotype, Mouse Phenotype, Pathway and Interaction databases were used to
54 generate a feature matrix (cell types by features) and hierarchically clustered. Hot spots of the
55 disease-specific enrichments were highlighted and details were shown on the left. More details
56 can be found in Methods. **(B)** Summarizing predicted functions and interplay of immune cells in
57 COVID-19 blood and lung. Aforementioned key observations in this study were shown in
58 peripheral blood mononuclear cells (PBMC) and bronchoalveolar lavage (BAL) in healthy
59 donors, mild and severe COVID-19 patients, including changes of cell abundance, specific
60 marker genes, upregulated secretion, cell development and cell-cell interactions.

61

62 **Fig. 7. Comparative analysis of differentially-expressed immunoregulatory genes between**
63 **COVID-19 and other immune-mediated diseases.** **(A)** Uniform Manifold Approximation and
64 Projection (UMAP) shows the distributions of cell types (Left) and diseases (Top right) after the
65 integration of datasets in multiple studies. MS: multiple sclerosis; IIH: idiopathic intracranial
66 hypertension. IIH patients were recruited as controls in the multiple sclerosis study. **(B)** Dynamic
67 changes of immune cell types in different immune-mediated diseases compared to healthy

98 controls. Log₂(ratio) was calculated to show the levels of changes. *, p<0.05, **, p<0.01, ***,
99 p<0.001. Statistical models can be found in the Methods. Leuk-UTI: sepsis patients that enrolled
100 into UTI with leukocytosis (blood WBC ≥ 12,000 per mm³) but no organ dysfunction. (C)
101 Normalized expression values of key genes involved in immune signaling and responses are
102 shown for cell types across multiple diseases. Lowly expressed genes (maximal average
103 expression level across all cell types in the heatmap is less than 0.5 after Log₂CPM normalization)
104 were removed.

105

106 **Figure S1. Cell distribution and abundance in the integrated COVID-19 PBMC data. (A)**

107 Distributions of COVID-19 conditions (Left) and data sources (Right) for the integrated PBMC
108 data are shown on the same UMAP of Figure 2A. (B) Bar plot depicts distributions of disease
109 conditions in 5 individual PBMC single-cell datasets. Percentages of 3 disease conditions in each
110 dataset is shown on y axis. (C) The integrated bar plot shows percentages of 3 disease conditions
111 in each cell type per dataset. Dataset abbreviations and cell types were concatenated to show
112 disease distributions of specific cell types in the selected datasets. These labels are colored by
113 their cell type designations and ordered by the ascending percentages of COVID-19 conditions.

114

115 **Figure S2. Dynamic changes of cell type abundances in five COVID-19 PBMC datasets.**

116 Relative abundances and differences of major cell types in each single cell dataset are shown and
117 compared to controls per each disease condition, per each single-cell dataset. Box plots of all cell
118 types in PBMC are shown except for the 5 highlighted cell types shown in Figure 2B. Statistical
119 methods are the same with Figure 2B.

120

121 **Figure S3. Cell distributions and dynamic changes in the integrated COVID-19 BAL data.**

122 (A-C) Distributions of disease conditions (A), data sources (B) and samples (C) are shown on the
123 same UMAP of Figure 2C. (D) Box plots depict dynamic changes of cell types across COVID-19
124 conditions in BAL that are not covered in Figure 2D. Statistical methods are the same with Figure
125 2B.

126

127 **Figure S4. Cell type abundance changes in COVID-19 lung parenchyma dataset. Box plots**

128 depict percentages of cell types in control samples and severe COVID-19 samples. We used cell
129 type clusters identified in the original publication but modified cell naming of macrophage

30 subtypes to distinguish monocyte derived macrophage subtypes present in BAL fluid samples.
31 Statistical methods are the same with Figure 2B.

32

33 **Figure S5. Sub-cluster-specific genes of neutrophils of COVID-19 patients.** (A) Distribution
34 of disease conditions (Left) and data sources (Right) for the integrated neutrophil data on the
35 same UMAP of Figure 3A. (B) UMAPs of neutrophil sub-cluster-associated genes from Figure
36 3C. Normalized expression values for each gene were used. (C) Normalized expression values of
37 neutrophil-associated genes and other important immune signatures are shown for 5 neutrophil
38 sub-clusters. Lowly expressed genes (genes with maximal average expression level across all
39 neutrophil sub-clusters less than 0.5 after Log₂CPM normalization) were removed from the gene
40 pool of cytokines, chemokines, ISGs, interleukins, interferons, corresponding receptors and
41 MHC-II. (D) The volcano plot depicts differentially expressed genes between circulating mature
42 neutrophils (Neu0,1) and extravasated neutrophils (Neu3) (Left); as well as DEGs between pro-
43 neutrophils (Neu4) and pre-neutrophils (Neu2) (Right). Statistical methods are the same with
44 Figure 5C. Representative enriched biological processes (Gene Ontology) are shown in the
45 bottom.

46

47 **Figure S6. Macrophage-related signatures in the integrated BAL data.** (A) Normalized
48 expression values of myeloid-cell-associated genes and other important immune signatures are
49 shown for 9 macrophage sub-clusters. Lowly expressed genes (genes with maximal average
50 expression level across all macrophage sub-clusters less than 0.5 after Log₂CPM normalization)
51 were removed from the gene pool of MHC-II, cytokines, chemokines, ISGs, interleukins,
52 interferons and their receptors. (B) Volcano plots were drawn for DEGs of MoAM3,4 versus
53 MoAM1,2,5 (Left) and TRAM 1,2 versus TRAM3 (Middle) and TRAM3 versus MoAM1,2,5
54 (Right). Statistical methods are the same with Figure 5C. (C) Normalized expression values were
55 shown on the same UMAP of Figure 3B for important genes including macrophage signatures,
56 ISGs, interferons, receptors and MHC-II.

57

58 **Figure S7. A uniquely-activated monocyte-derived cell type (MoAM5) exhibits a broad**
59 **signature of cytokines, chemokines, and interleukins including IL6.** (A) Normalized
30 expression values of IL6 on the same reference UMAP of integrated BAL data as Figure 3B. (B)
31 Scale expression levels of IL6 for each macrophage sub-cluster on the violin plot. (C) Heatmap of
32 expression levels of pan-MoAM signatures and MoAM5-specific signatures in all myeloid cells in

53 both PBMC and BAL. **(D)** Network of functional and phenotypic associated pan-MoAM
54 signatures and MoAM5-specific signatures from (C). Associations were retrieved from ToppGene
55 enrichment results. IL6 is highlighted in the network. As a caveat, the MoAM5 subtype
56 represented a small fraction among the BAL MoAM subtypes and the majority of these cells were
57 observed in a single severely-affected individual.

58

59 **Figure S8. Cell type and cell subtype-specific divisions of cytokine, chemokine, and**
60 **interleukin signaling pathways in BAL of severe COVID-19 patients.** **(A)** Heatmap of
61 expression patterns of ligands and receptors in cytokine, chemokine, interleukin, CSF and TNFSF
62 signaling pathways across cell types of BAL in severe patients. Average normalized expression
63 values were shown and lowly expressed ligands or receptors (maximal normalized expression
64 value for a row in the heatmap < 0.5) were removed. To reduce bias, MoAM5 was removed
65 because cells in the cluster were mainly from one patient. Cell types that have less than 5% cells
66 from severe patients were removed, including TRAM1 and TRAM2. Neutrophils are highlighted
67 in the heatmap. **(B)** Interaction network of BAL cells in severe patients using CellChat. CCL,
68 CXCL and IL1 signaling pathways were shown. The width of edges represents the strength of
69 interactions and the size of nodes represents the abundance of cell types.

30

31 **Figure S9. Characteristics of sub-clusters of classical monocytes in the integrated COVID-**
32 **19 PBMC data.** **(A)** UMAPs of 4 sub-clusters (Left) and COVID-19 conditions (Right) of
33 classical monocytes are shown. Grey dots are other myeloid cells in the UMAP of integrated
34 PBMC myeloid data. **(B)** UMAPs of normalized expression values of specific signatures for
35 classical monocyte sub-clusters. **(C)** Normalized expression values of monocyte-associated genes
36 and other important immune signatures are shown for 4 classical monocyte sub-clusters. **(D)** Gene
37 modules of classical monocyte sub-clusters, as well as other myeloid cell types in the integrated
38 PBMC myeloid data. Representative genes in each module are shown on the left. ToppGene
39 enrichment results for classical monocyte sub-clusters are shown on the right. Columns are
40 clustered using hierarchical clustering. **(E)** Similarity matrix of myeloid cell types using genes in
41 (D). Pearson correlation was used to evaluate similarity. **(F)** Dot plot of MHC-II, ISGs,
42 interleukin genes and cell cycle genes for each myeloid cell type. Scale values were used.

33

34 **Figure S10. Features of conventional dendritic cell sub-clusters and polarized signaling**
35 **genes.** **(A)** UMAPs of 13 sub-clusters (Left) and sources (Right) of conventional dendritic cells

96 after data integration. **(B)** Normalized expression values of sub-cluster-specific genes on the
97 UMAP. **(C)** Normalized expression values of cDC-associated genes and other important immune
98 signatures are shown for 13 cDC sub-clusters. **(D)** Gene modules of cDC sub-clusters with 200
99 most significantly upregulated genes in each module. Representative genes are shown on the left.
10 Gene enrichment results of some modules from ToppGene are shown on the right. **(E)** Similarity
11 matrix of sub-clusters using genes in (D). Pearson correlation was used for similarity scores and
12 hierarchical clustering was applied for rows and columns. **(F)** The heatmap shows the clustering
13 of signaling genes, including cytokines, chemokines, interleukins and their receptors. Red boxes
14 highlight severe patients associated sub-clusters and their upregulated genes. Green boxes
15 highlight mild patients-associated sub-clusters and their upregulated genes.

16

17 **Figure S11. Landscape of myeloid cells in the integrated PBMC and BAL data. (A-B)**
18 UMAPs of myeloid cells in integrated PBMC (A) and BAL (B) data. Cell types which were
19 further clustered are highlighted in different colors. **(C)** The heatmap shows associations between
20 subclusters of myeloid cells and myeloid-cell-associated pathways, such as antigen presenting, T
21 cell activation, phagocytosis etc. Gene enrichment scores, defined as $-\log_{10}(\text{adjusted p value})$,
22 were calculated as the strength of associations. Pie charts showed the proportions of COVID-19
23 conditions in each sub-cluster.

24

25 **Figure S12. Gene expression signatures of cell types and subtypes activated by COVID-19**
26 **are extensively associated with coagulation, hemostasis, and thrombosis-associated**
27 **pathways, functions, and knockout phenotypes. (A)** Functional association heatmap of gene
28 signatures from COVID-19 cell types demonstrates differential enrichment for pathways
29 associated with coagulation, vascular permeability, complement, extravasation, platelet activation
30 and aggregation, response to wounding, as shown. Gene modules of cell types and sub-clusters
31 that participate in these pathways were used to calculate enrichment scores. **(B)** Network of
32 upregulated genes in coagulation/thrombosis-associated pathways (A) shows the potential gene-
33 gene interactions in immunothrombosis of COVID-19 patients. CellChat and ToppCell/ToppGene
34 protein-protein ligand receptor and cell adhesion interaction databases were used to find
35 interaction pairs among upregulated genes. **(C)** A new network derived from (B) shows integrin-
36 associated interactions between platelets and other cells.

37

28 **Figure S13. Emergence of platelet subtypes suggestive of functionally significant alternative**
29 **roles in in hemostasis, coagulation, wound response, and neutrophil recruitment and**
30 **activation. (A)** The heatmap shows ToppCell gene modules of 6 platelet sub-clusters in COVID-
31 19 PBMC. Each gene module contains 200 most significant genes for each sub-cluster and
32 important genes are shown on the left. Gene enrichment analysis was conducted using ToppGene
33 and top enrichment results from biological processes (Gene Ontology) are shown on the right. **(B)**
34 Dot plot of integrin and other platelet-associated genes. Scale values are shown on the figure. **(C)**
35 Heatmap of associations between subclusters of platelets and platelet-associated pathways (Gene
36 Ontology). Gene enrichment scores, defined as $-\log_{10}(\text{adjusted p value})$, were calculated and
37 shown.

38
39 **Figure S14. Consistent emergence of a series of early and maturing B cells and**
40 **plasmablasts in BAL fluid and PBMC across multiple datasets. (A-B)** UMAPs of B cells (A)
41 and plasmablasts (B) from multiple datasets. **(C-D)** UMAP of normalized expression values of
42 immunoglobulin genes (C) and ISGs (D) for B cells. **(E-F)** UMAP of normalized expression
43 values of immunoglobulin genes (E) and sub-cluster associated genes, such as cell cycle genes
44 and B cell markers (F) for plasmablasts. **(G)** Gene modules of B cell sub-clusters and plasmablast
45 subtypes with 200 most significant genes in each module. Hierarchical clustering was applied for
46 columns. **(H)** Three representative enriched biological processes (Gene Ontology) are shown for
47 these two subtypes using DEGs of plasmablasts in Figure 5C.

48
49 **Figure S15. Gene Enrichment analysis of B cell subtypes and autoimmune-associated**
50 **signatures. (A)** Heatmap shows gene enrichment scores of B-cell-associated pathways for each B
51 cell sub-cluster and plasmablast subtype. **(B)** Pathway and function association network of
52 upregulated genes in B cells of BAL in mild COVID-19 patients. **(C-D)** Heatmaps show
53 normalized expression levels of autoimmune-associated ligands and receptors (Figure 5E) in
54 lupus nephritis (C) and rheumatoid arthritis (D).

55
56 **Figure S16. Distinct subtypes of T cells and NK cells in COVID-19 BAL data. (A-C)** UMAPs
57 of subtypes (A), COVID-19 conditions (B) and data sources (C) of T cells and NK cells in the
58 integrated BAL data. **(D-E)** UMAPs of normalized expression values of exhausted T cell markers
59 **(D)** and ISGs **(E)**.

30

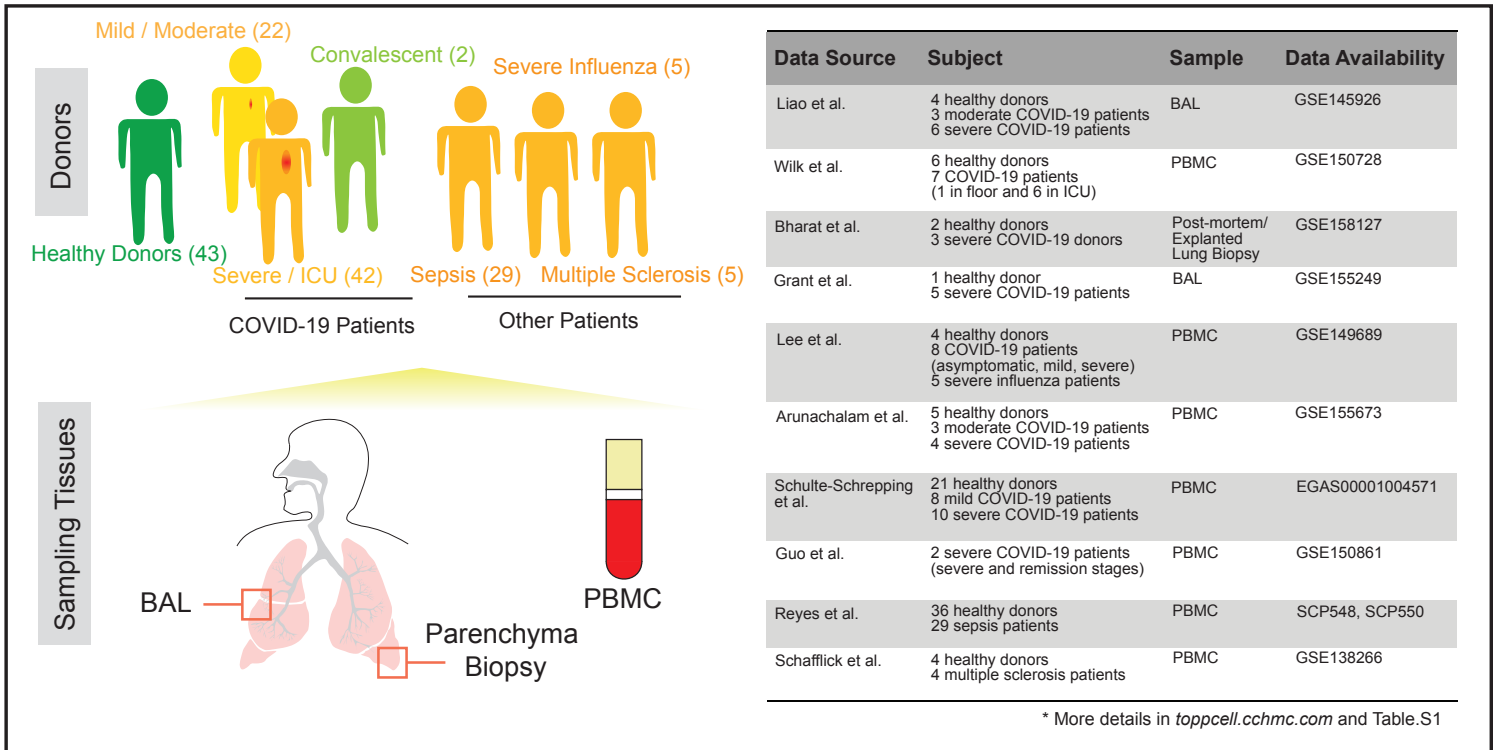
51 **Figure S17. Various T cell and NK cell subtypes in the integrated PBMC data. (A-B)**
52 UMAPs of T cell and NK cell subtypes (A) and COVID-19 conditions (B) after integration of T
53 cells in 5 PBMC single-cell datasets. (C) Dot plot shows T cell and NK cell subtype associated
54 genes for each subtype per disease condition. Labels of cell types of healthy donors, mild patients
55 and severe patients are colored by blue, yellow and red. Scaled expression values are shown using
56 a color scheme.

57
58 **Figure S18. Various cell types in immune-mediated diseases. (A, C, E)** Distributions of cell
59 types identified in influenza (A), sepsis (C) and multiple sclerosis (E) patients were shown on
60 UMAPs. **(B, D, F)** Distributions of disease conditions in influenza (B), sepsis (D) and multiple
61 sclerosis (F) patients were shown on UMAPs.

62

A

Data Collection



B

Quality Control & Integration

Computational Analysis

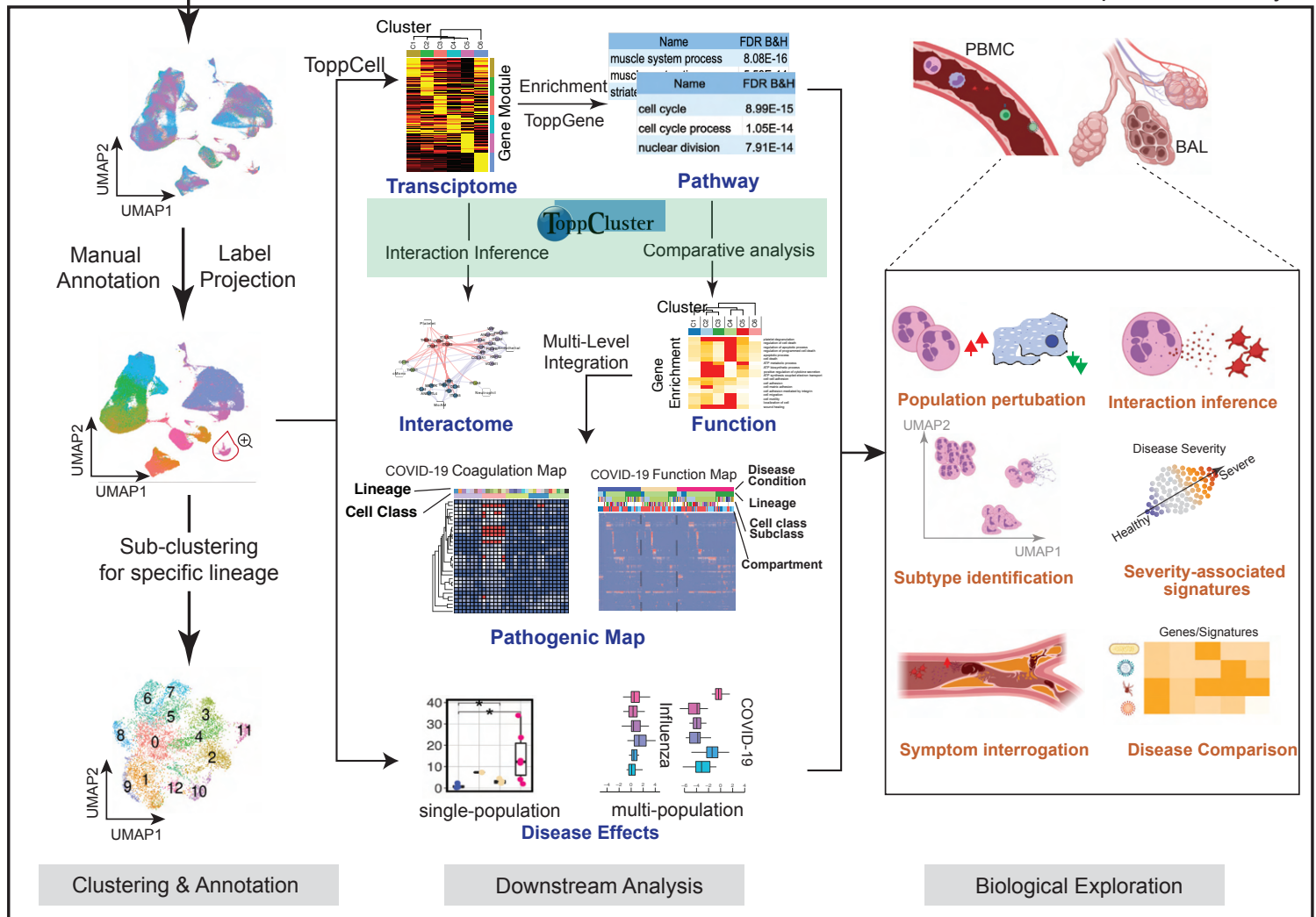


Fig. 1. Creating a COVID-19 Signature Atlas

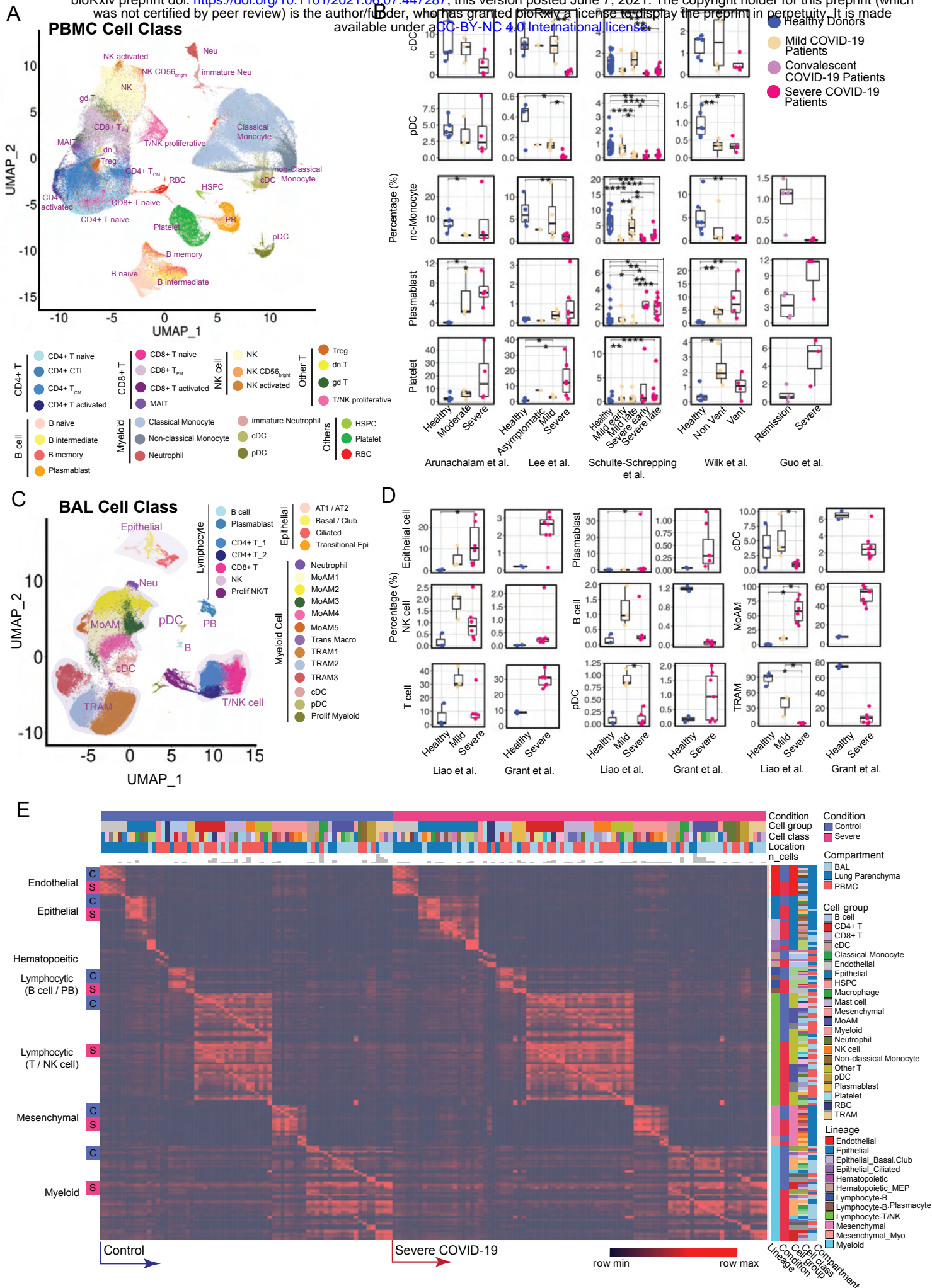


Fig. 2. Modularized representation of cell type specific gene signatures and dynamic changes of cell

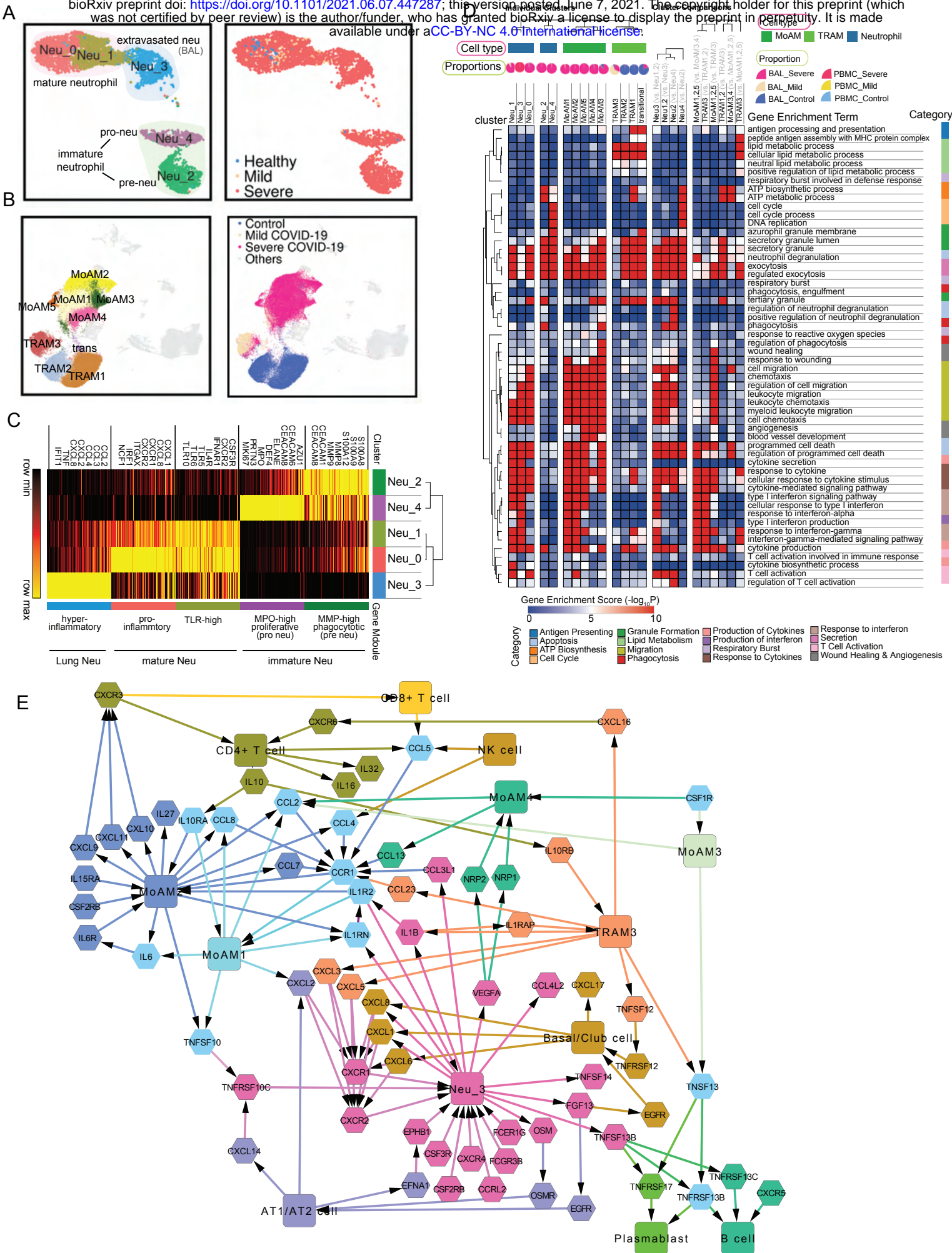


Fig. 3. Functional analysis of compartment-specific immature and subtype-differentiated neutrophils and monocytic macrophages in COVID-19 patients

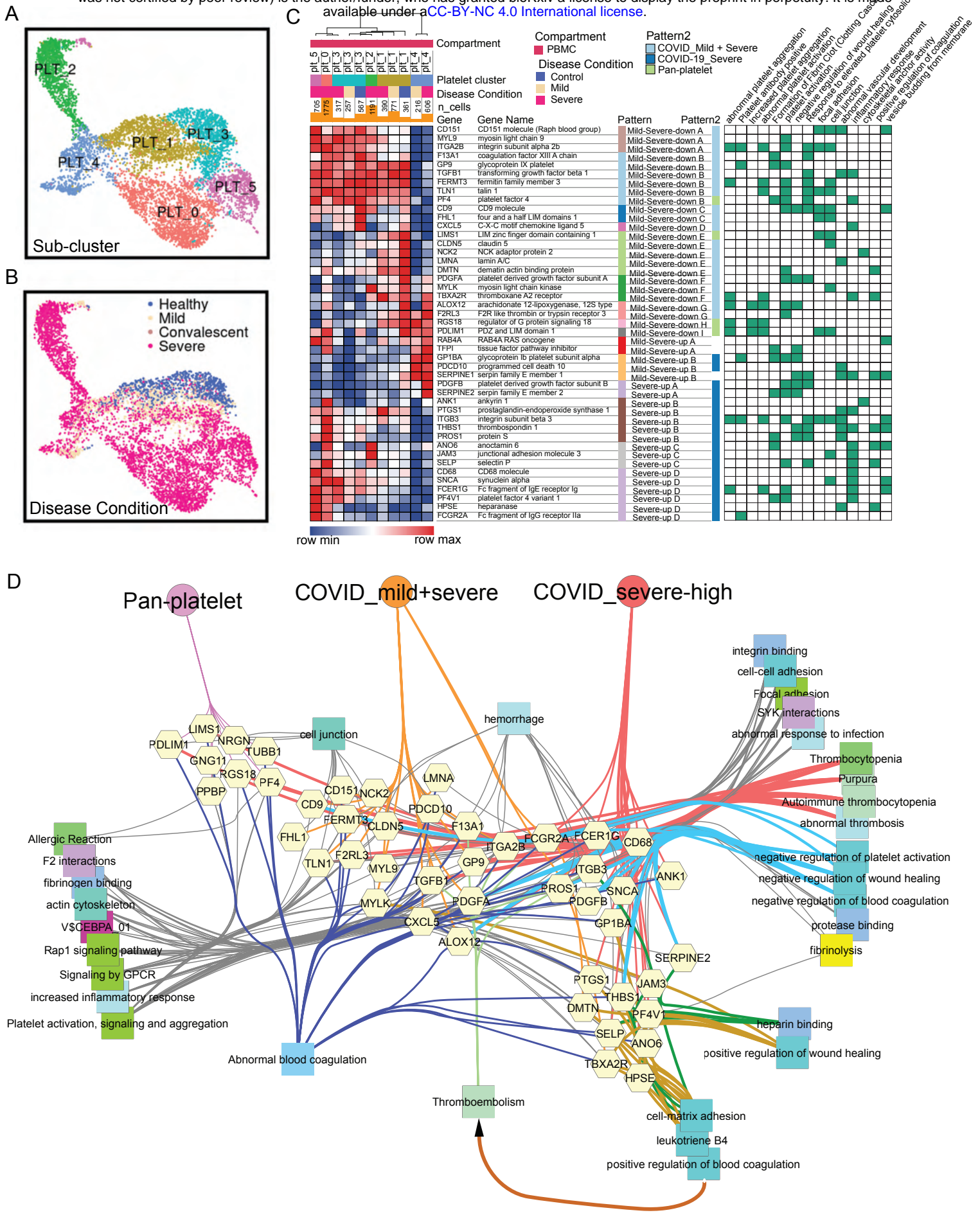
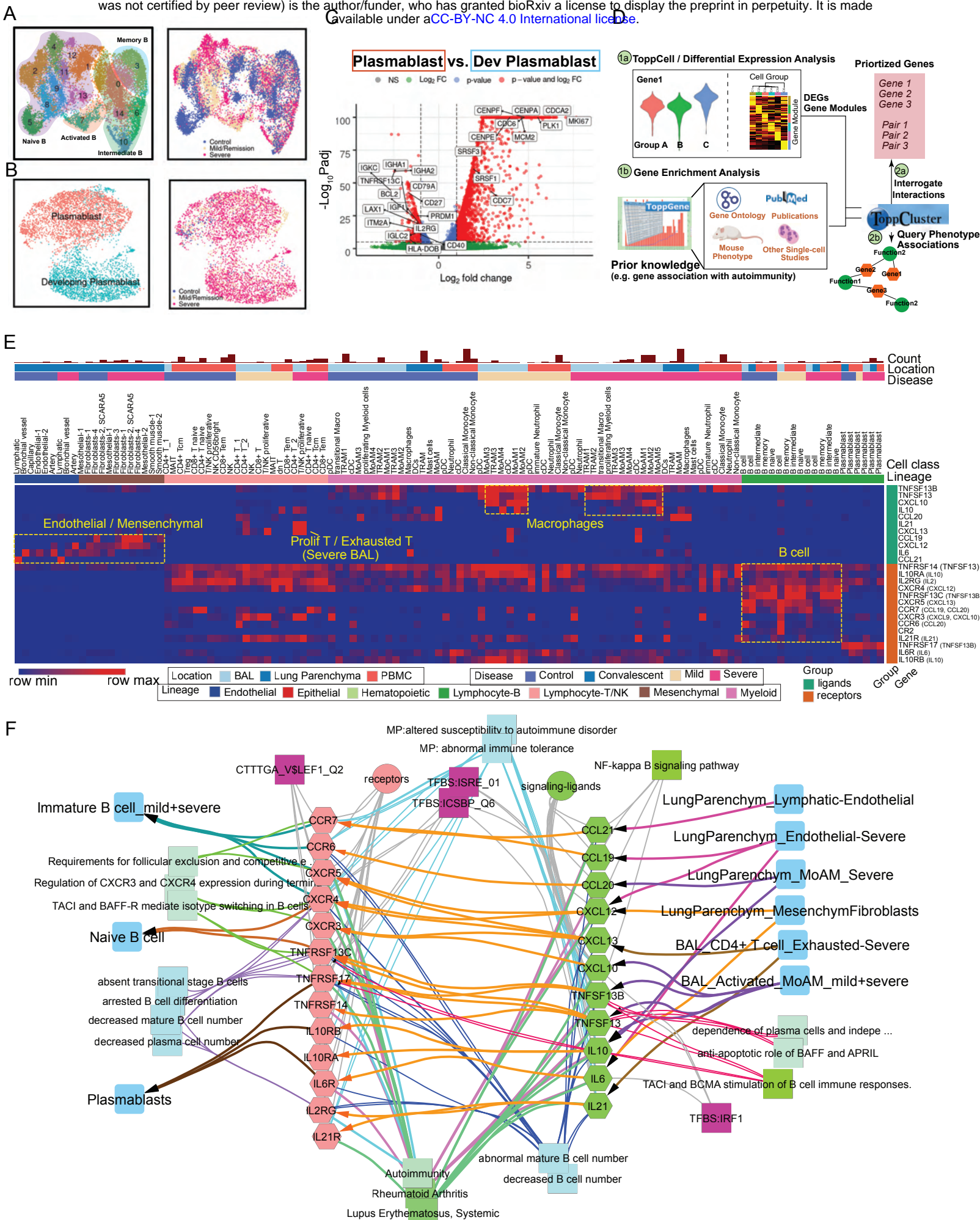


Fig. 4. COVID-19 driven reprogramming of platelets leads to drastically altered expression of genes associated with platelet adhesion, activation, coagulation and thrombosis



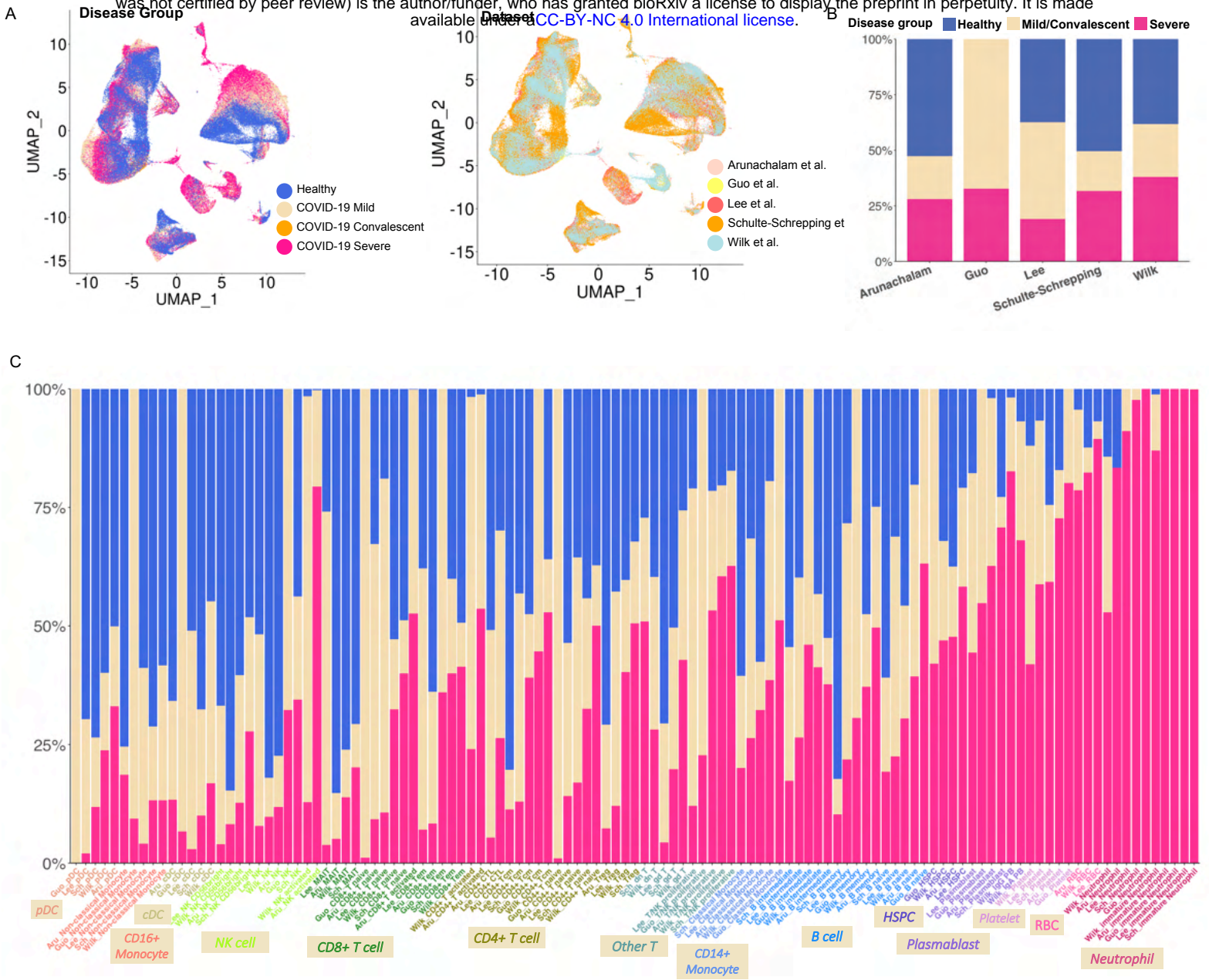


Figure S1. Cell distribution and abundance in the integrated COVID-19 PBMC data, relative to Figure 2.

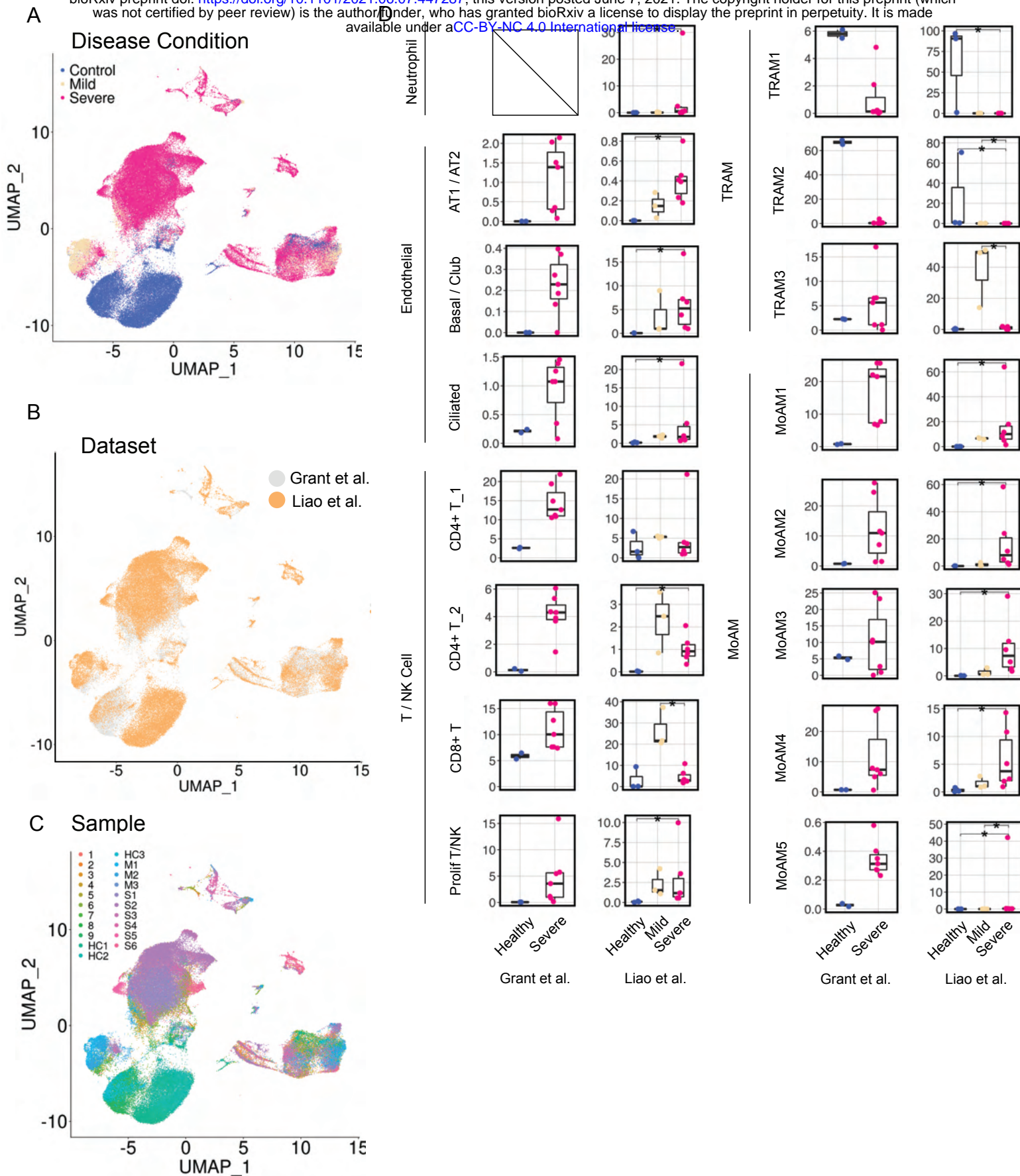


Figure S3. Cell distributions and dynamic changes in the integrated COVID-19 BAL data, relative to Figure 2.

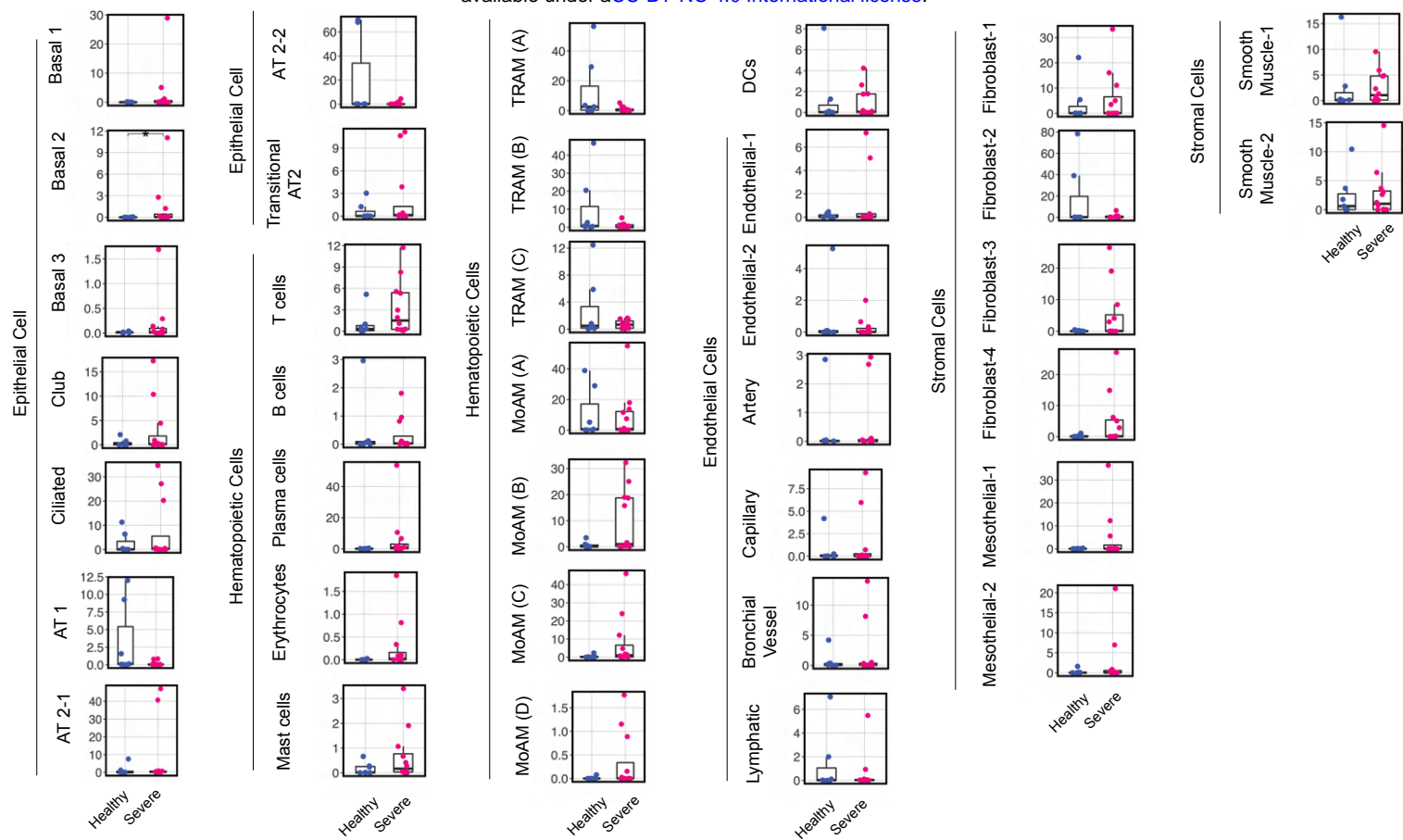
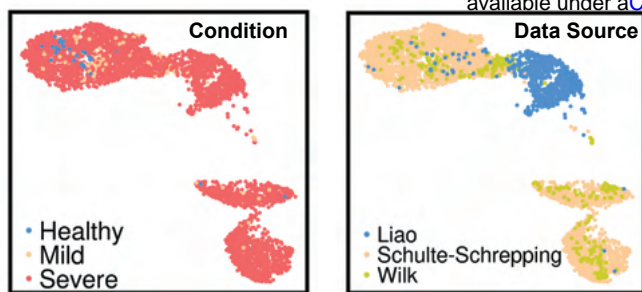
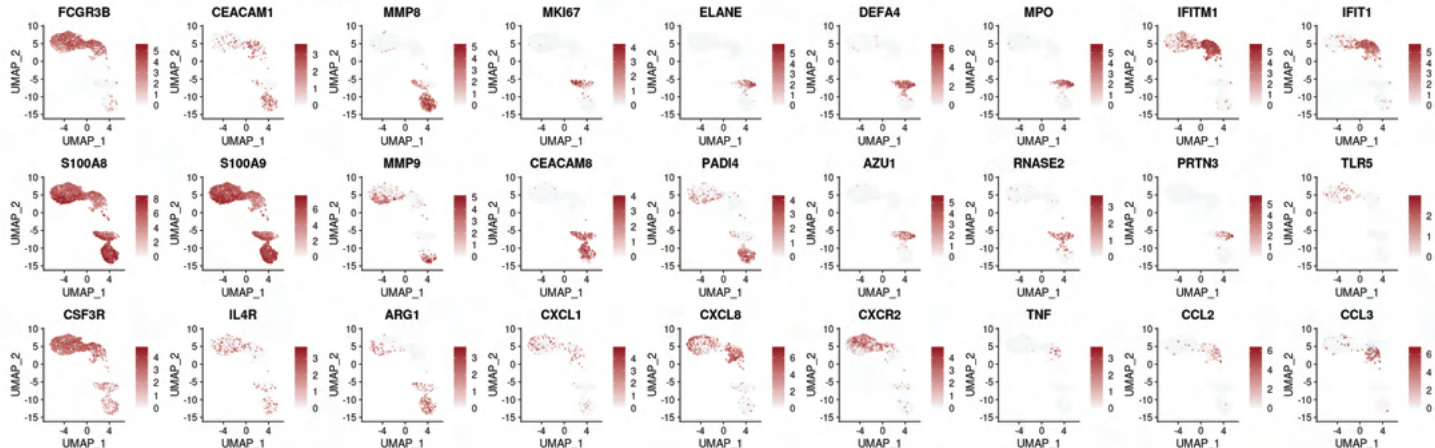


Figure S4. Dynamic changes of cell types in the COVID-19 lung parenchyma dataset, relative to Figure 2.

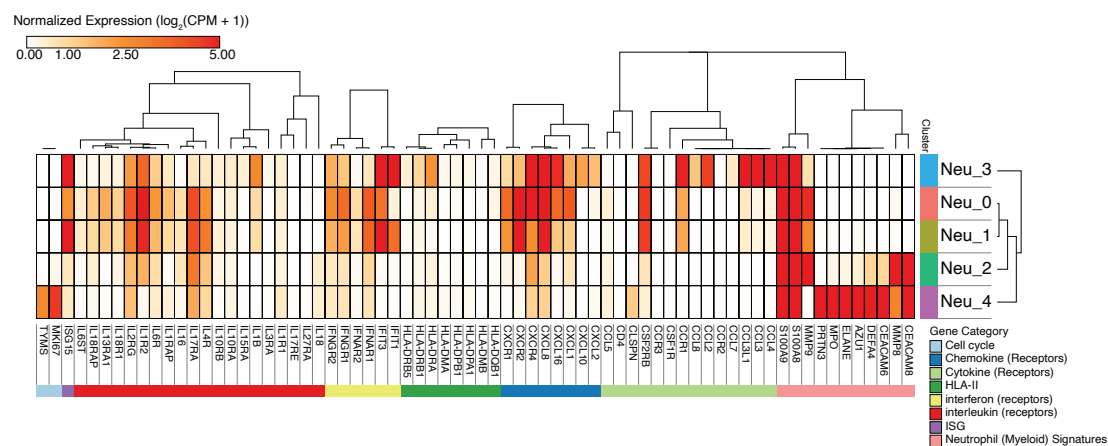
A



B



C



D

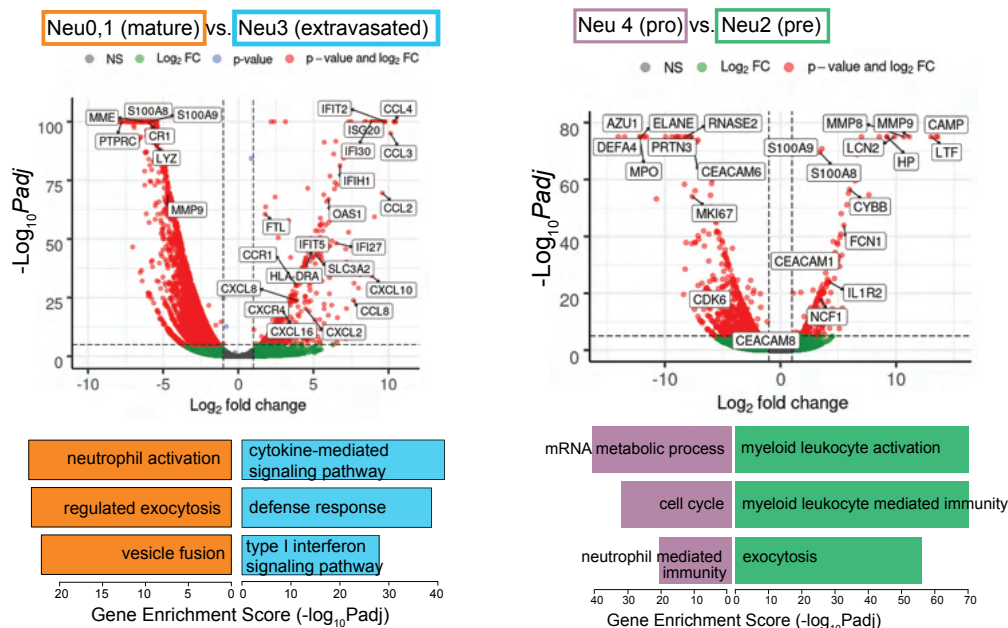
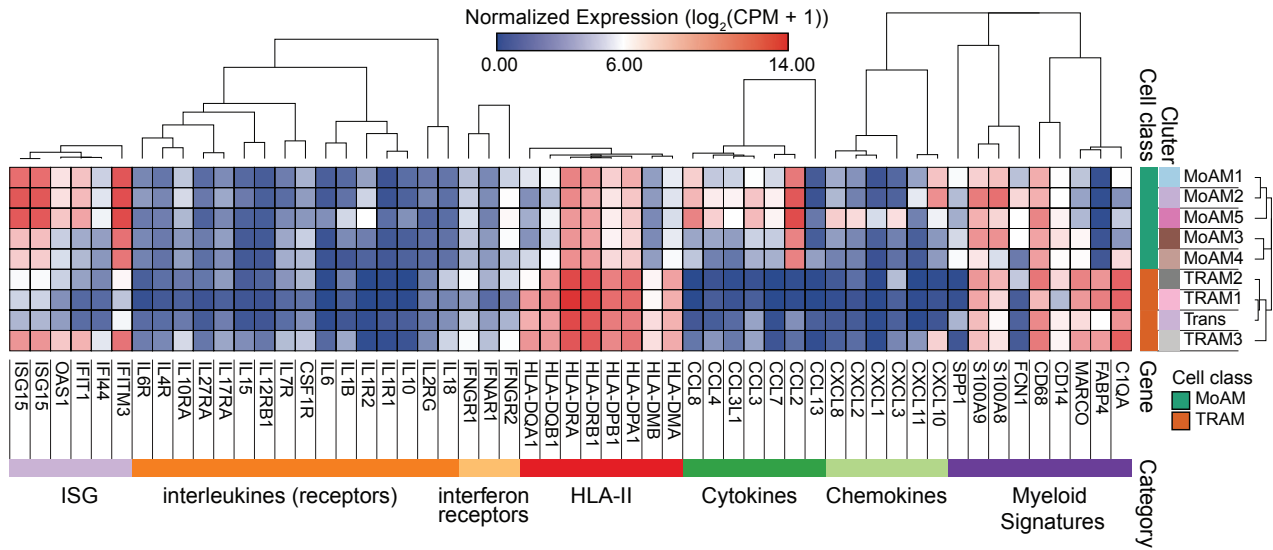
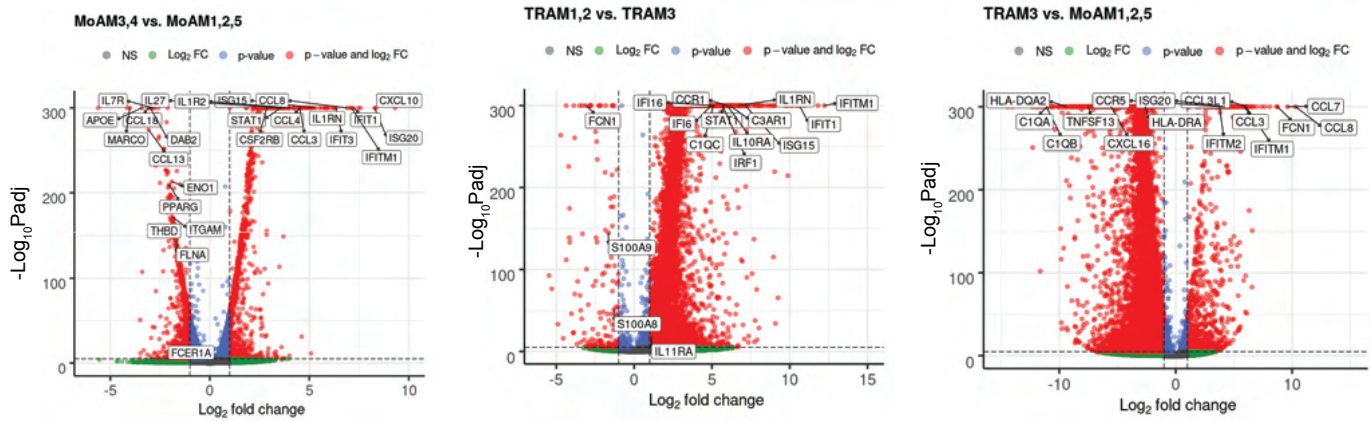


Figure S5. Sub-cluster-specific genes of neutrophils of COVID-19 patients, relative to Figure 3.

A



B



C

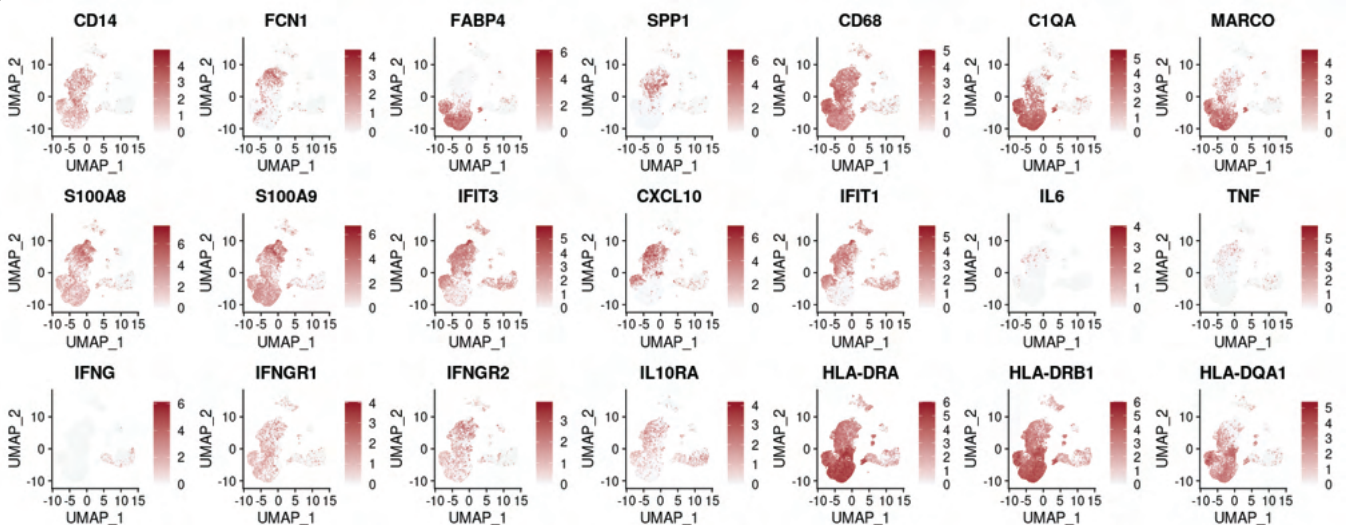


Figure S6. Macrophage-related signatures in the integrated BAL data, relative to Figure 3.

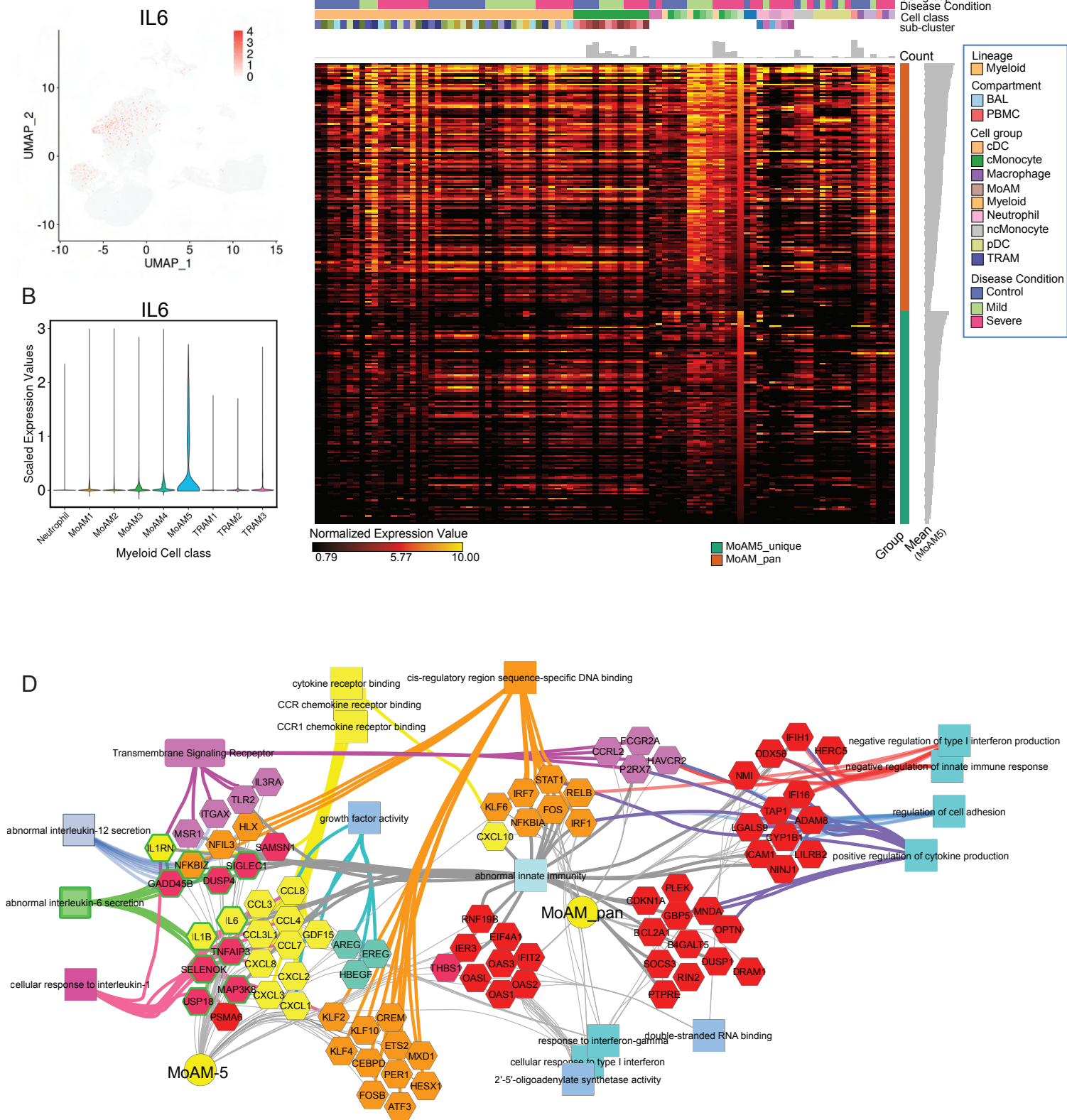


Figure S7. A uniquely-activated monocyte-derived cell type (MoAM5) exhibits a broad signature of cytokines, chemokines, and interleukins including IL6, relative to Figure 3.

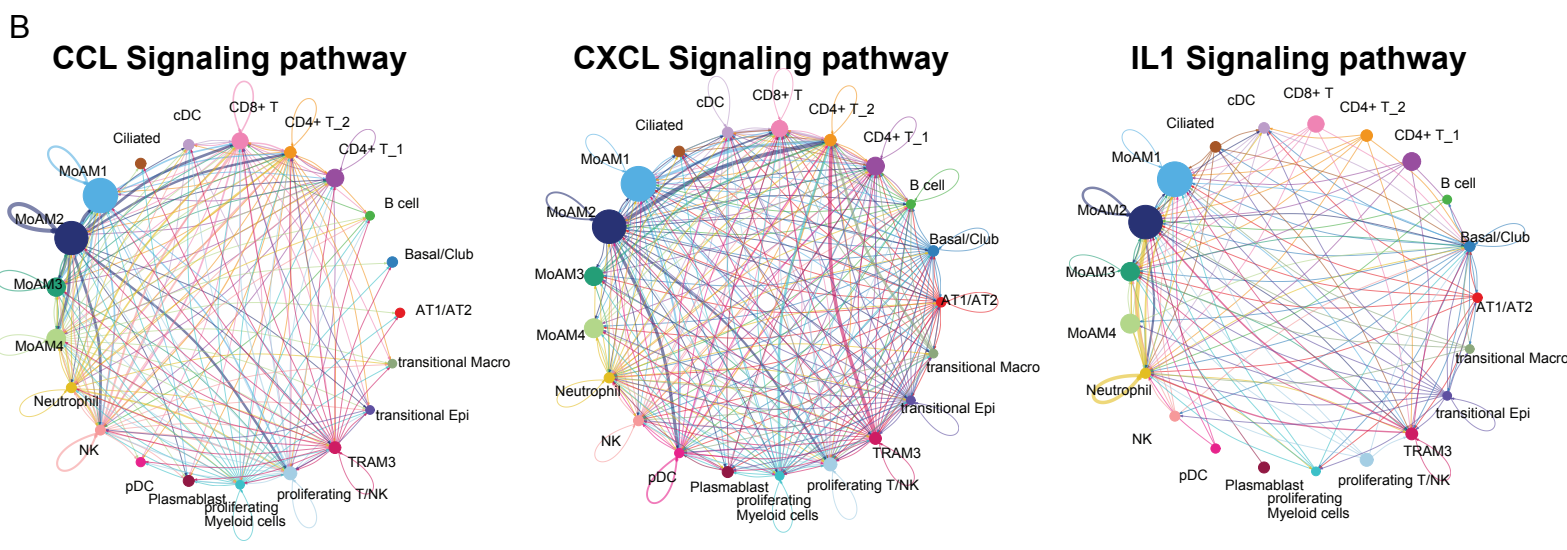
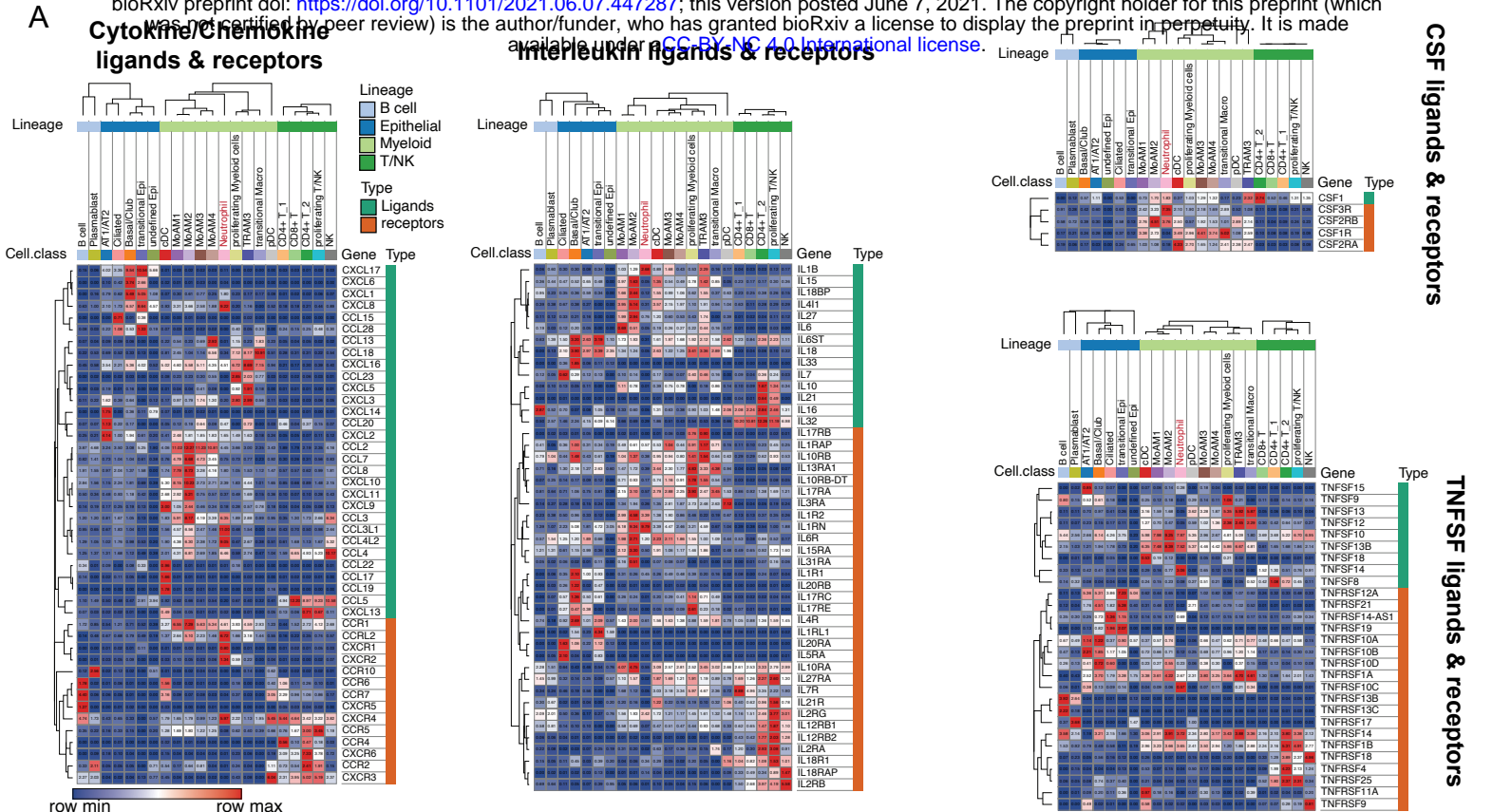
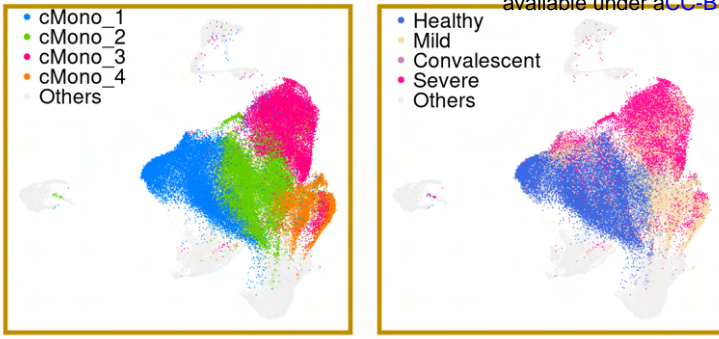
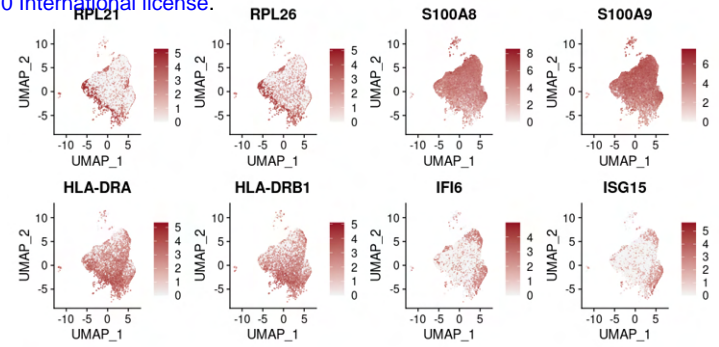


Figure S8. Cell type and cell subtype-specific divisions of cytokine, chemokine, and interleukin signaling pathways in BAL of severe COVID-19 patients, relative to Figure 3.

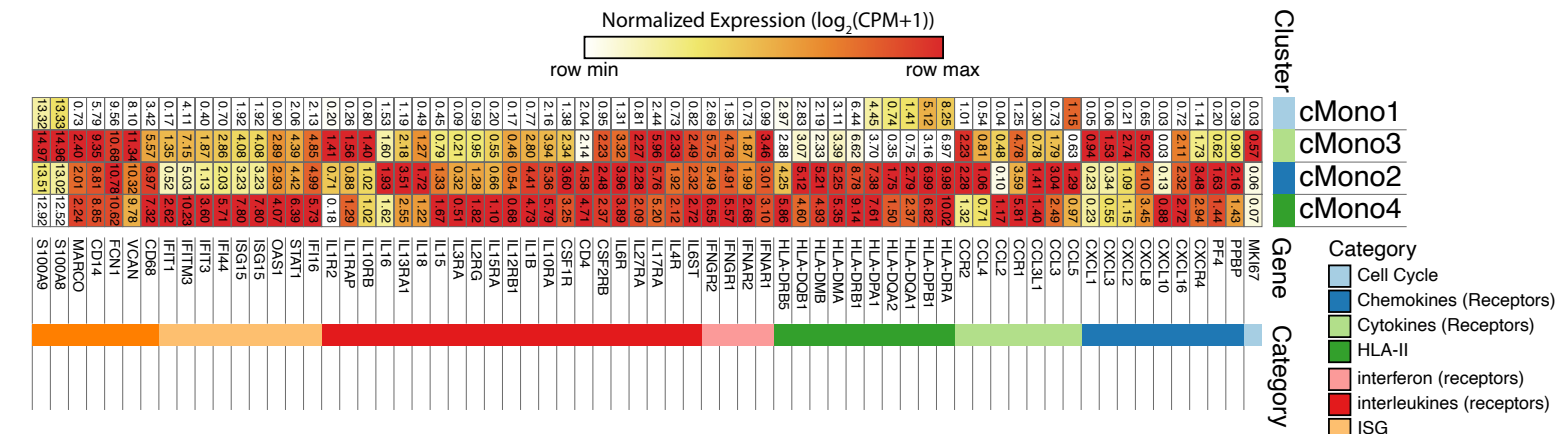
A



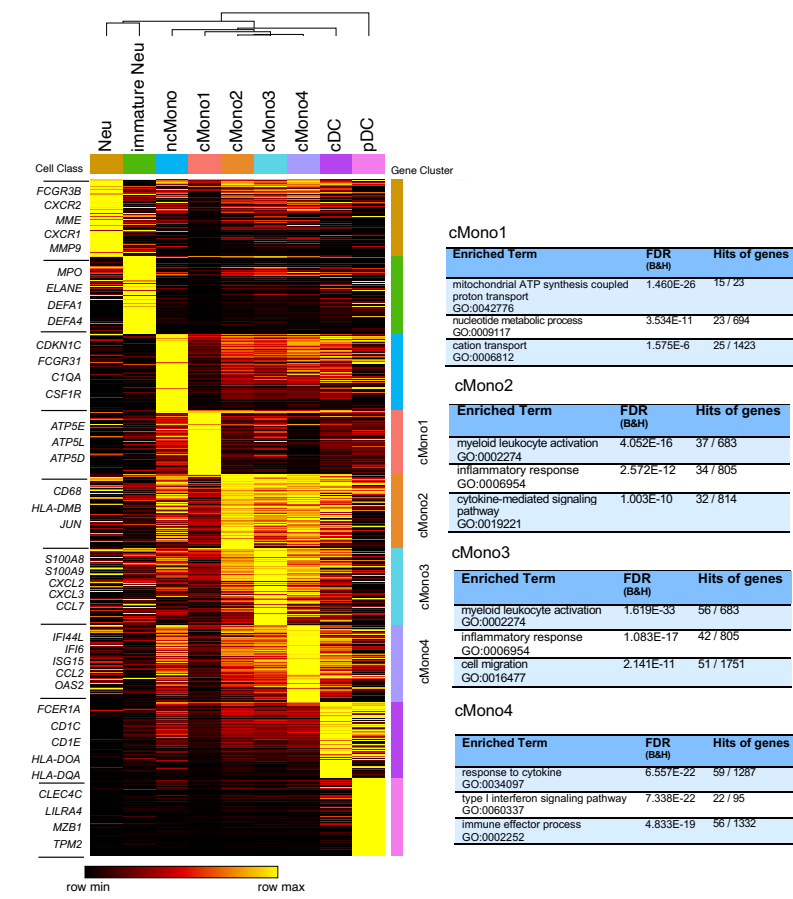
B



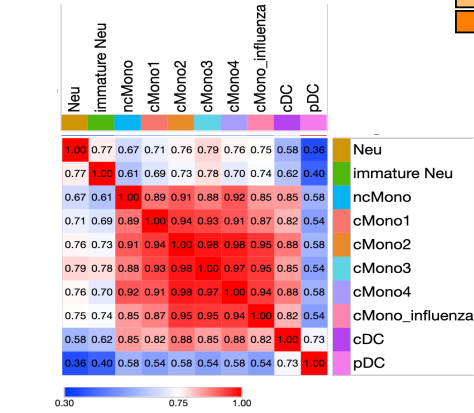
C



D



E



F

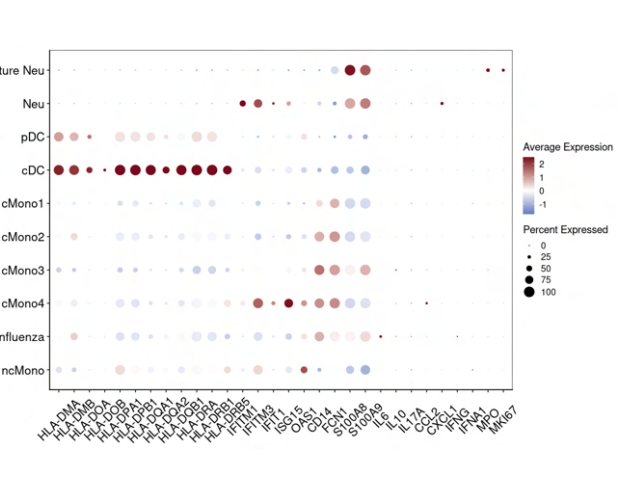


Figure S9. Characteristics of sub-clusters of classical monocytes in the integrated COVID-19 PBMC data, relative to Figure 3.

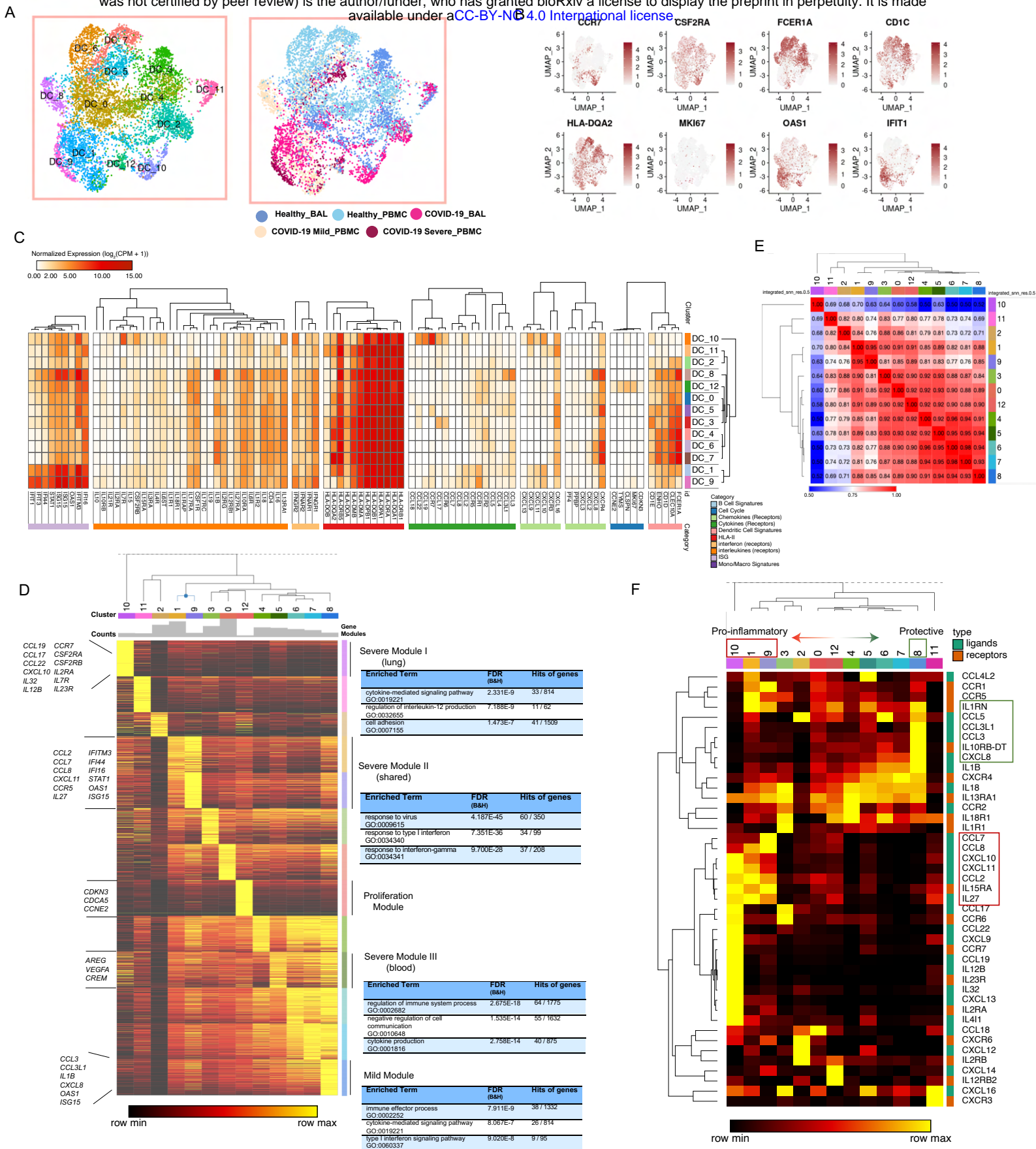
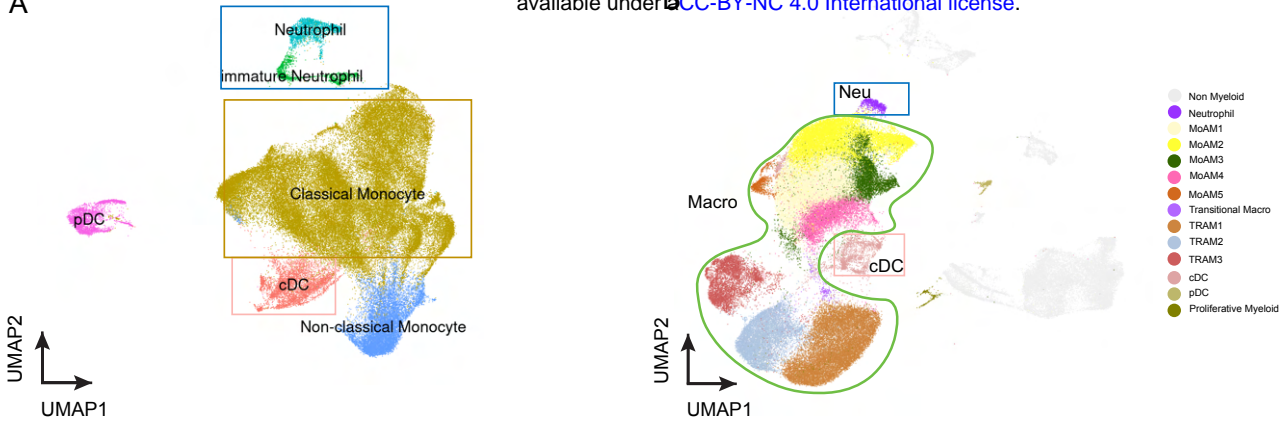


Figure S10. Features of conventional dendritic cell sub-clusters and polarized signaling genes, relative to Figure 3.

A



C

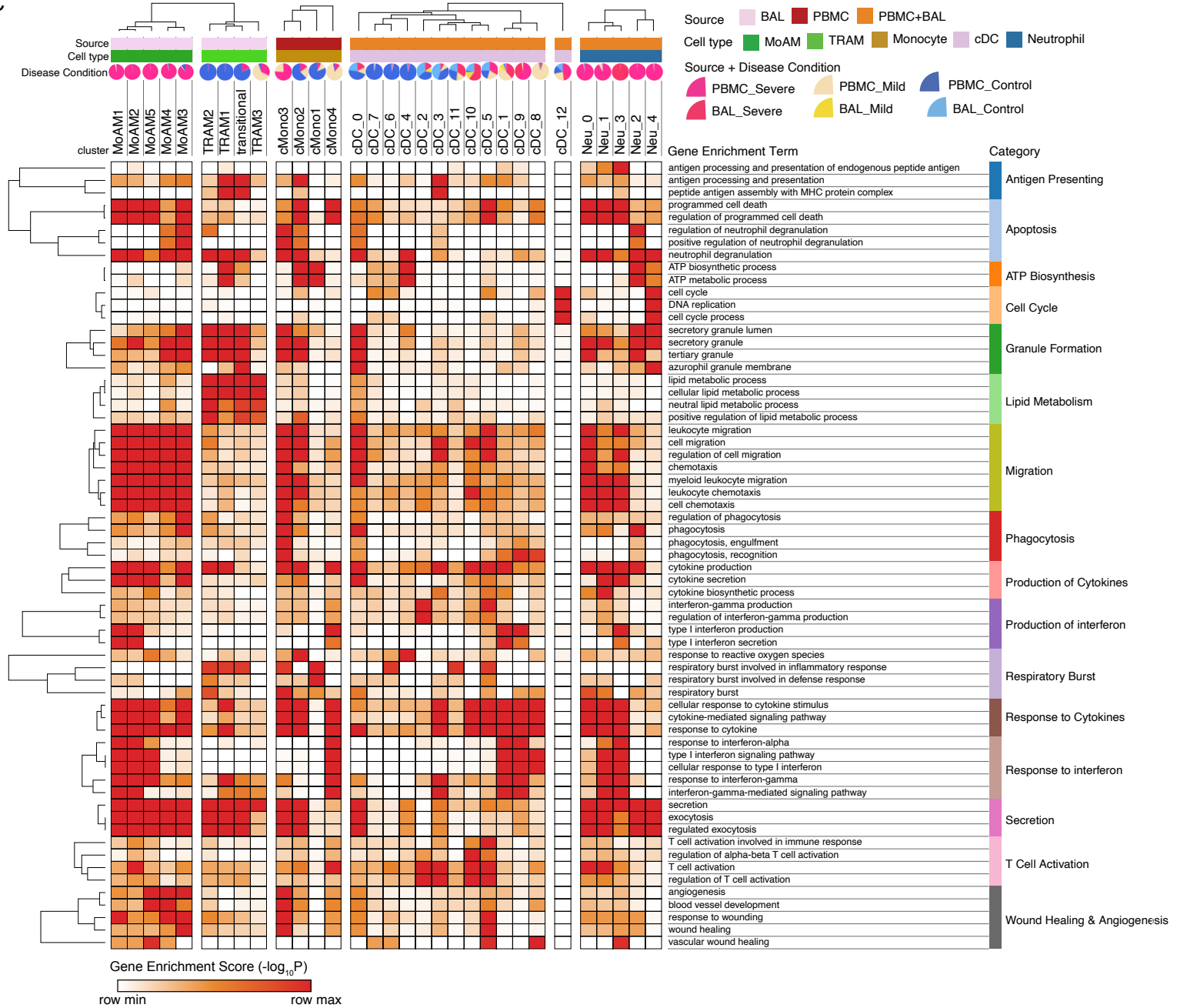


Figure S11. Landscape of myeloid cells in the integrated PBMC and BAL data, relative to Figure 3.

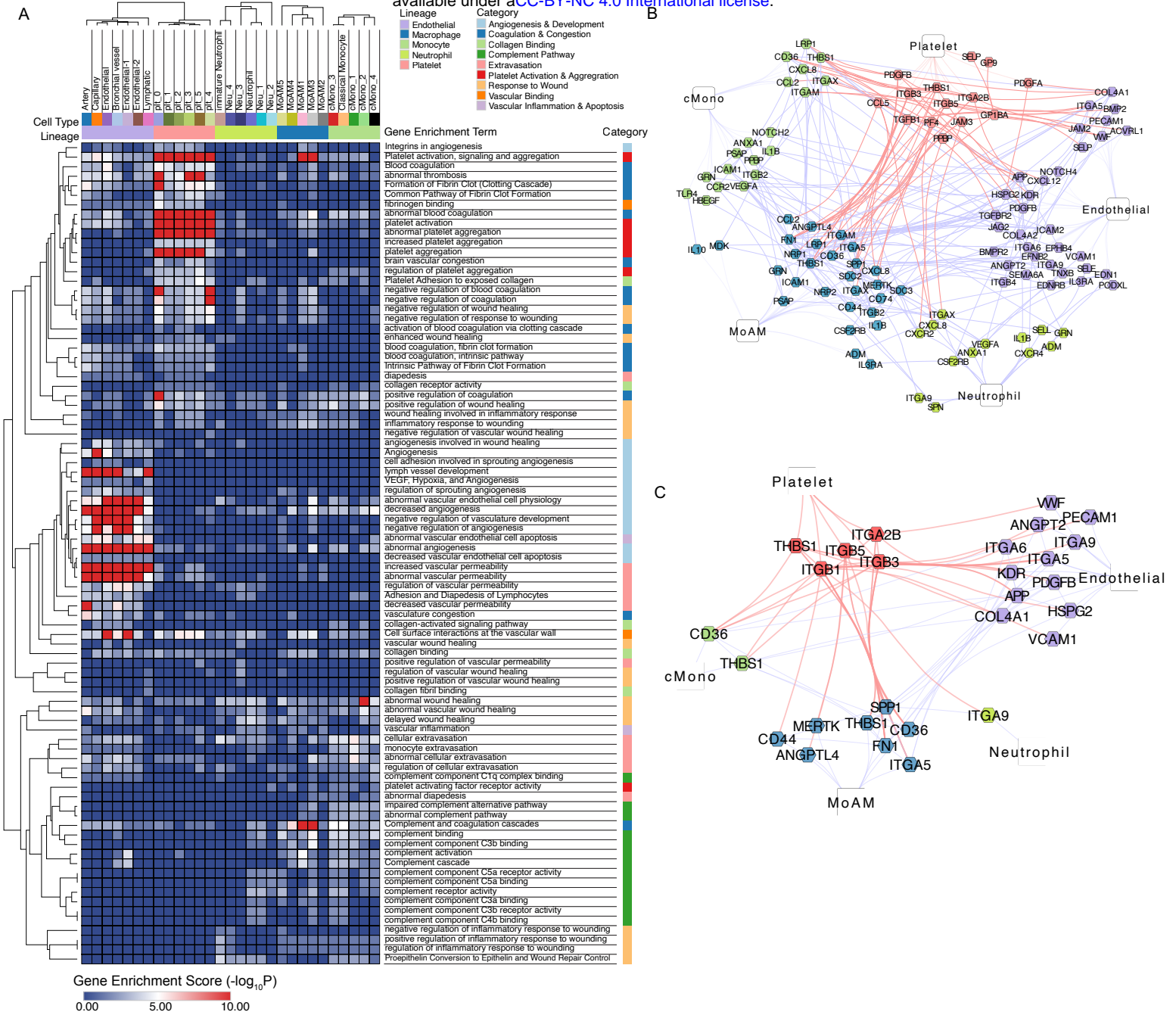
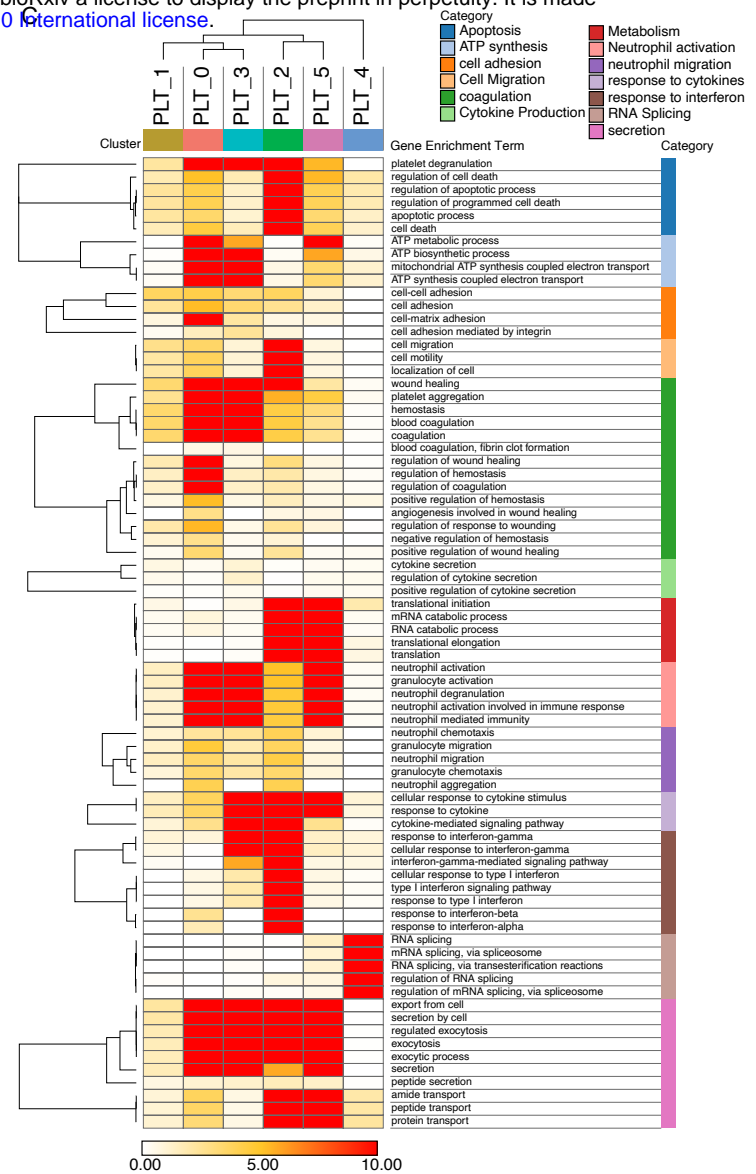
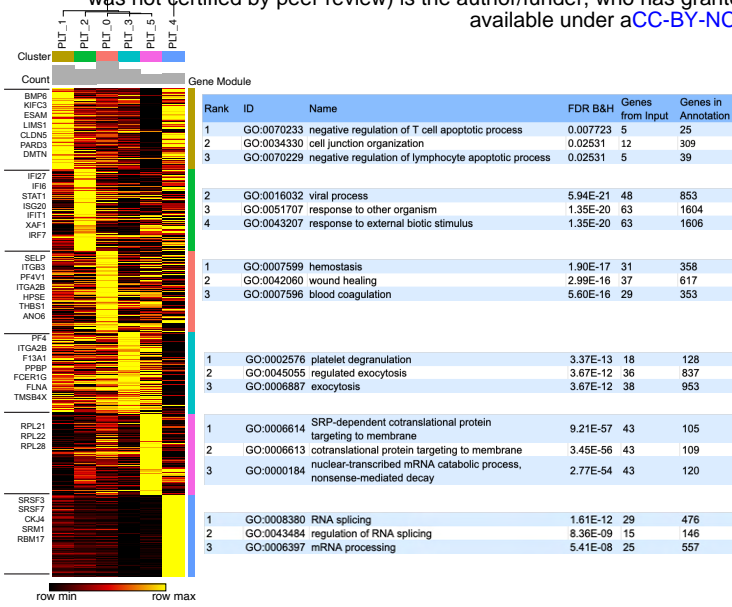


Figure S12. Gene expression signatures of cell types and subtypes activated by COVID-19 are extensively associated with coagulation, hemostasis, and thrombosis-associated pathways, functions, and knockout phenotypes, relative to Figure 4.

A



B

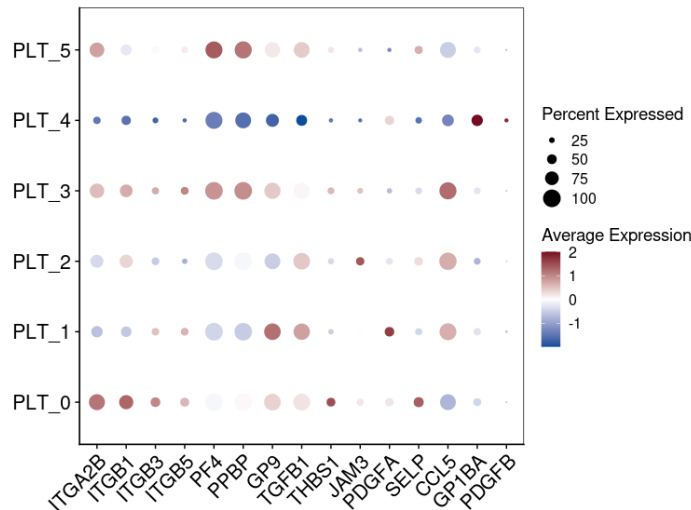


Figure S13. Emergence of platelet subtypes suggestive of functionally significant alternative roles in in hemostasis, coagulation, wound response, and neutrophil recruitment and activation, relative to Figure 4.

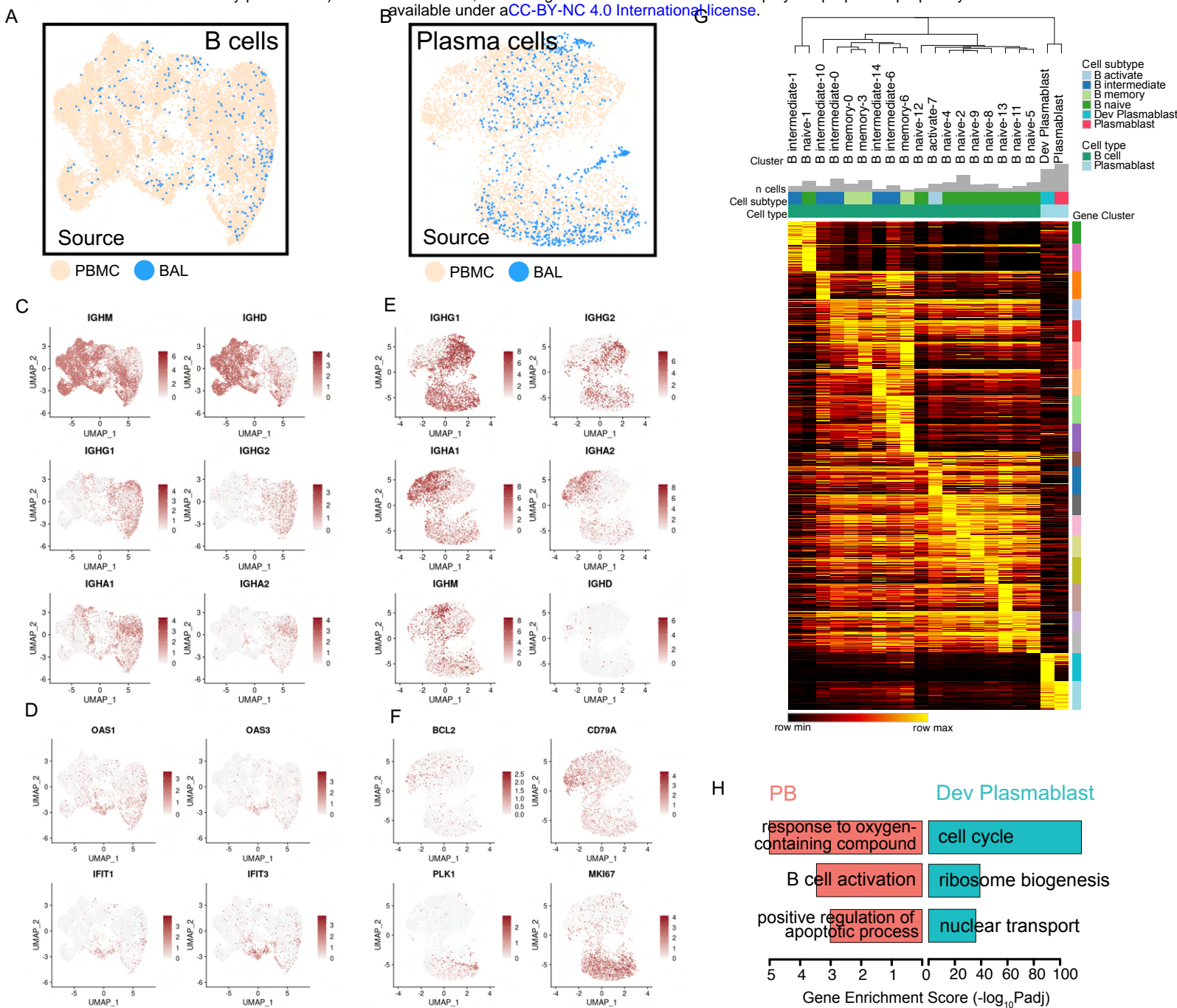


Figure S14. Consistent emergence of a series of early and maturing B cells and plasmablasts in BAL fluid and PBMC across multiple datasets, relative to Figure 5.

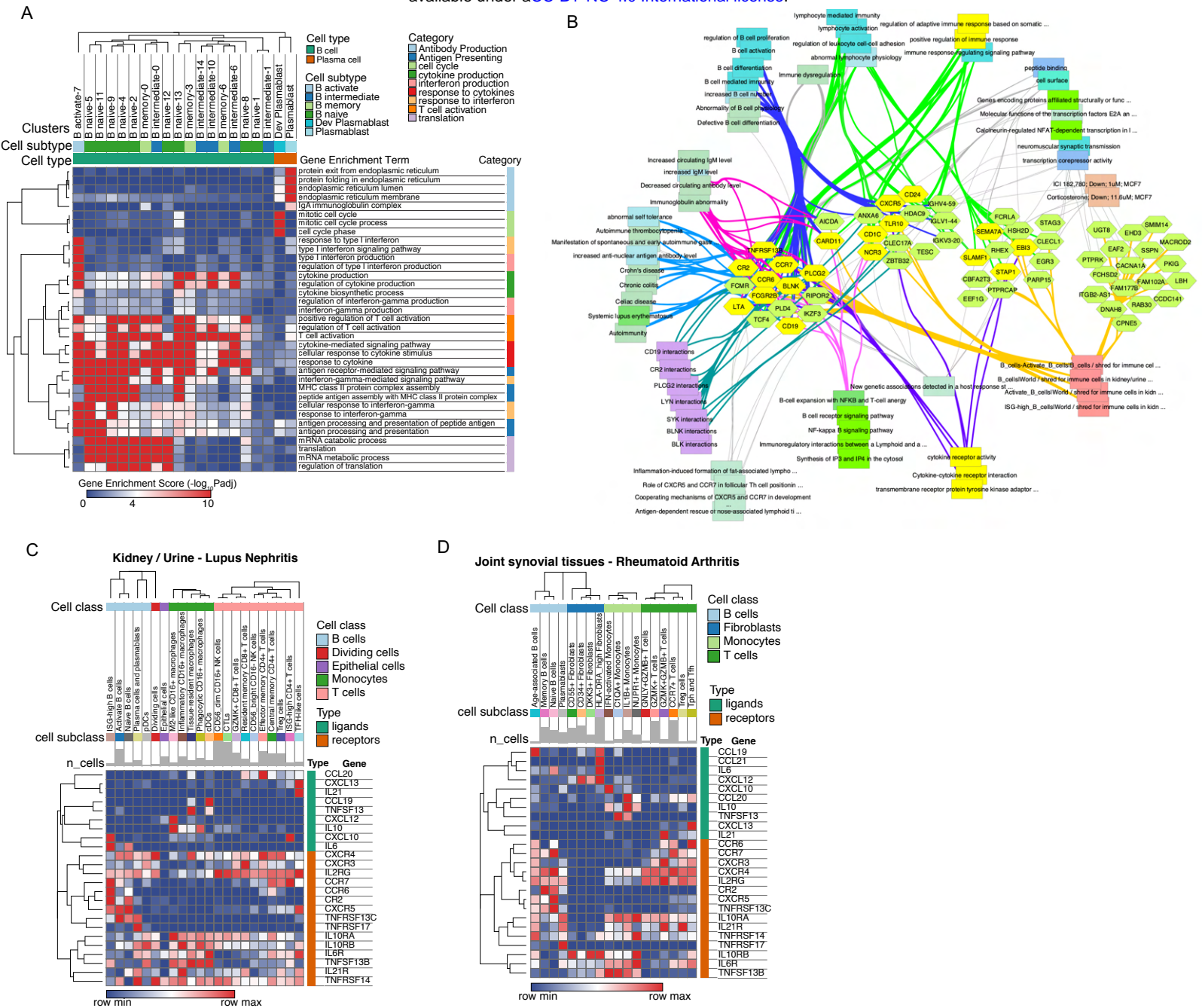


Figure S15. Gene Enrichment analysis of B cell subtypes and autoimmune-associated signatures, relative to Figure 5.

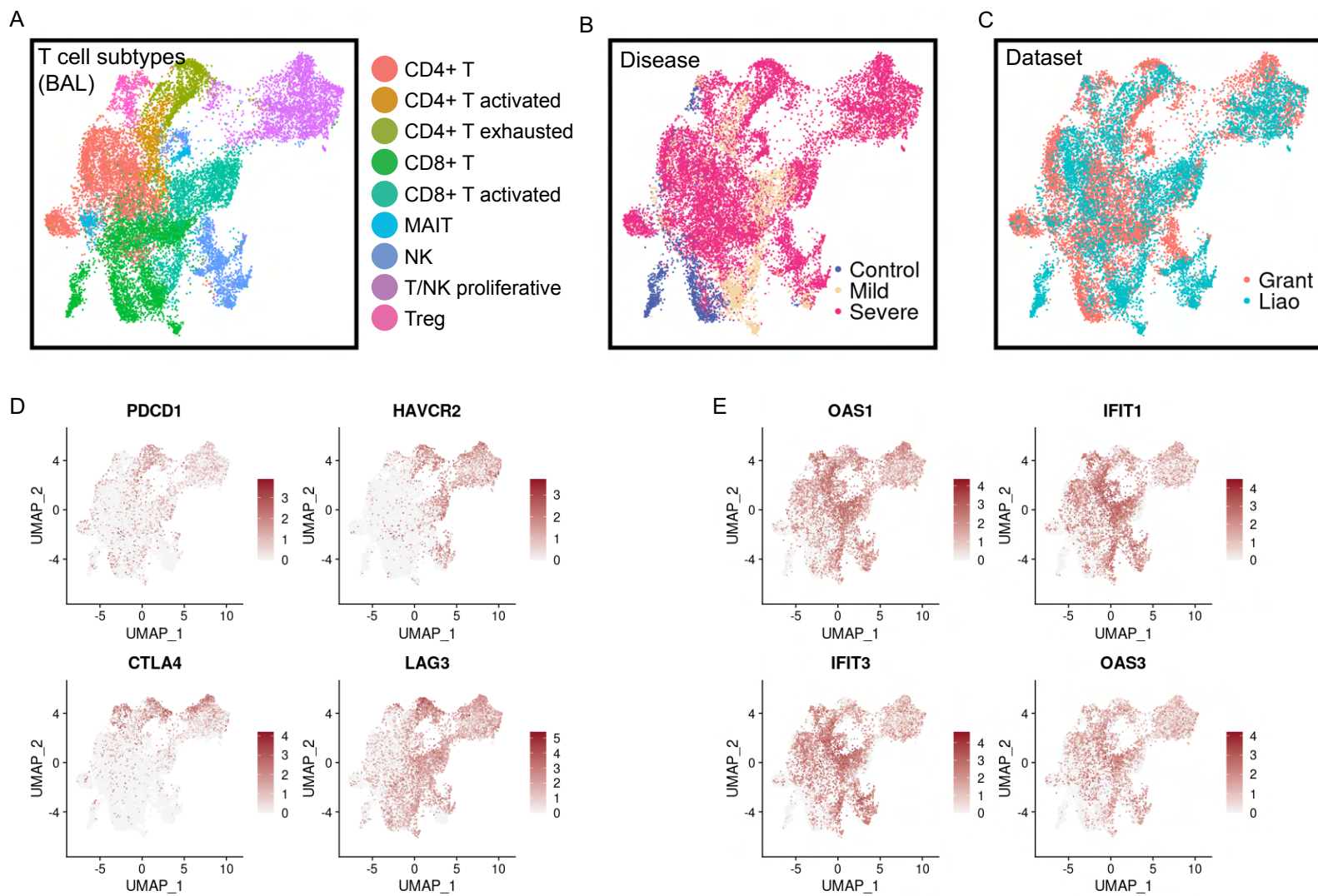
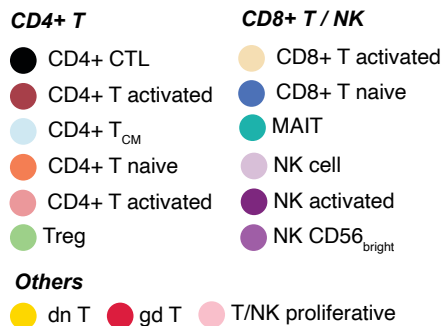
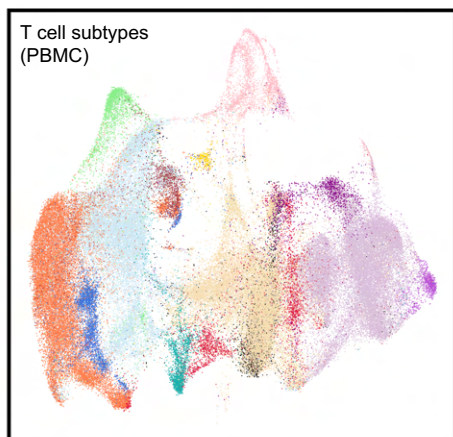
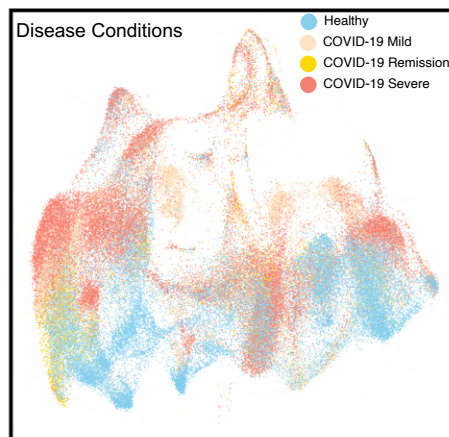


Figure S16. Distinct subtypes of T cells and NK cells in COVID-19 BAL data.

A



B



C

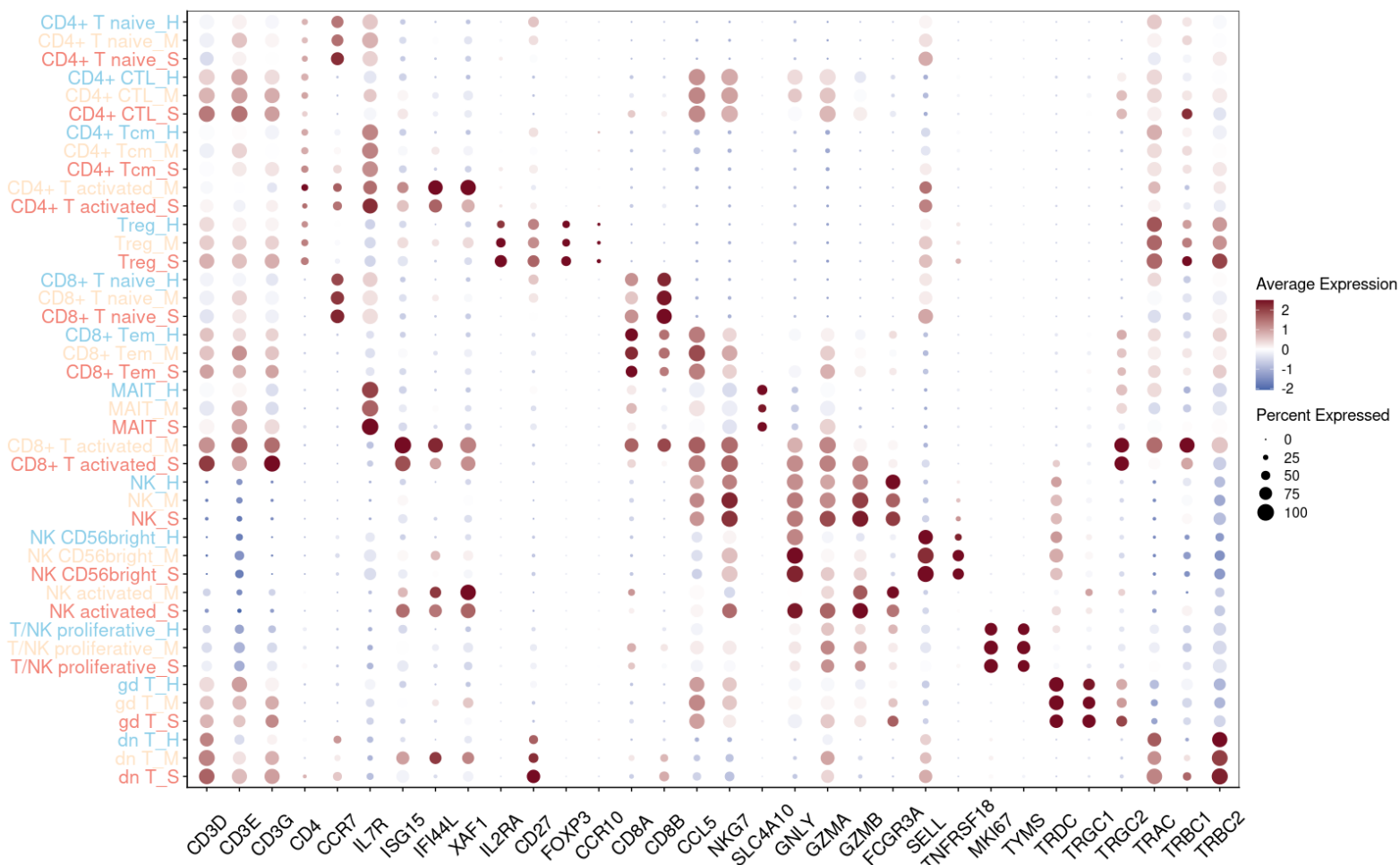
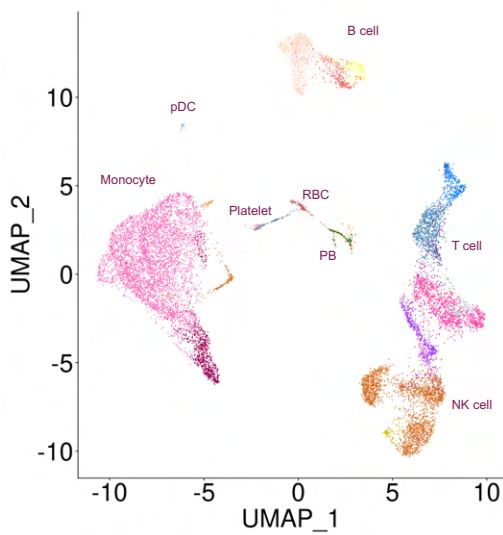


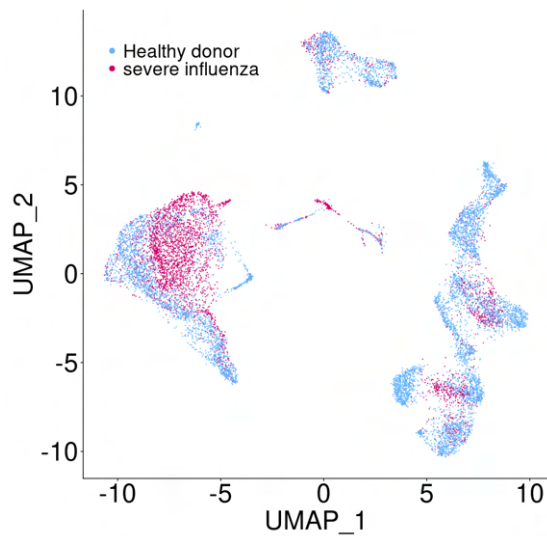
Figure S17. Various T cell and NK cell subtypes in the integrated PBMC data.

A

Influenza

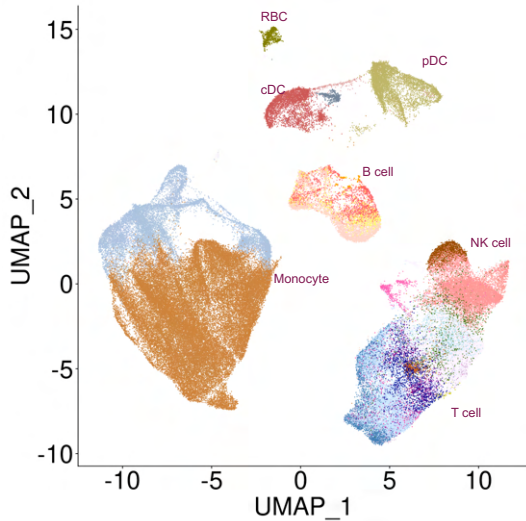


B

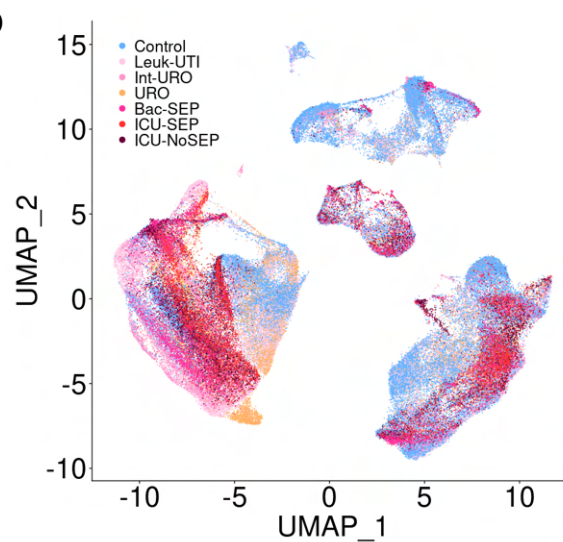


C

Sepsis

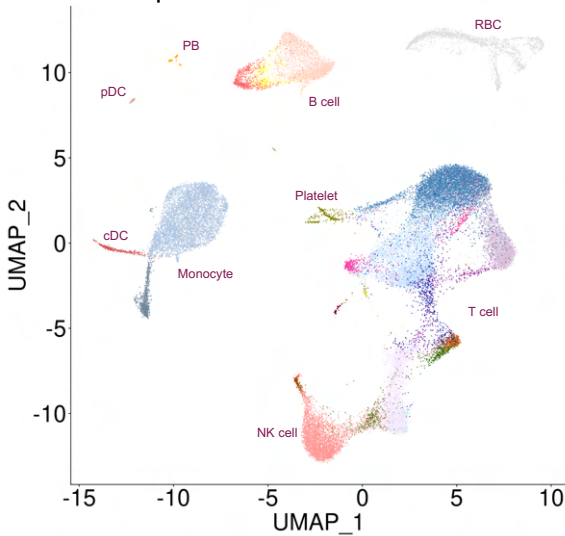


D



E

Multiple Sclerosis



F

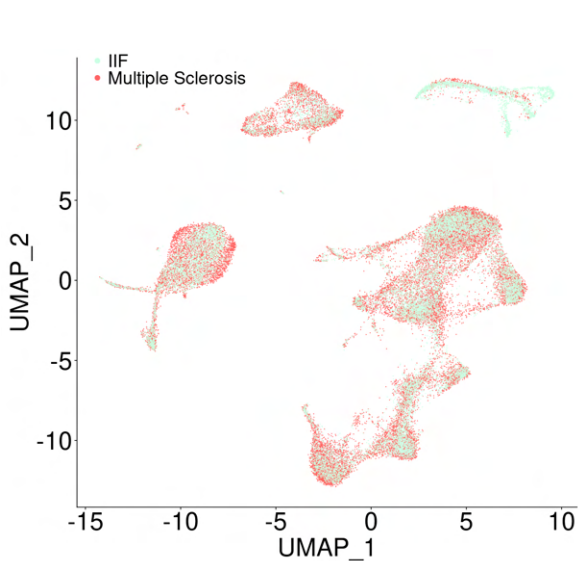


Figure S18. Various cell types in immune-mediated diseases, relative to Figure 7.